YAP engages RIF1 to dampen replication stress in squamous cell carcinoma.

Jodie Bojko[1], Benjamin Flynn[1,2], Bertram Aschenbrenner[3], Alexander Howard[1], Emily Lay[1], Emma Bailey[4], Natalia Krajic[3], Sandra Catalan[1], Kelli Gallacher[1], Elodie Sins[2], Jun Wang[4], Ute Jungwirth[1,5], Beate M. Lichtenberger[3], Gernot Walko[1,2,*]

[1]Department of Life Sciences, University of Bath, Bath, UK.

[2]Centre for Oral Immunobiology and Regenerative Medicine, Institute of Dentistry, Queen Mary University of London, London, UK.

[3]Department of Dermatology, Medical University of Vienna, Vienna, Austria.

[4]Barts Cancer Institute, Queen Mary University of London, London, UK.

[5]Cancer Research Horizons Therapeutic Innovation, Newcastle Drug Discovery Group, Translational and Clinical Research Institute, Newcastle University, Newcastle, UK.

[*]Correspondence: g.walko@qmul.ac.uk

Word count: Abstract, 175; remaining manuscript text (excluding references and figure legends, 13,461 words)

Abstract

Squamous cancers are the most frequently diagnosed solid tumours world-wide. The closely related transcriptional co-regulators YAP and TAZ(WWTR1) have emerged as important drivers of tumour initiation and progression in various types of squamous cell carcinoma. How YAP and TAZ execute their oncogenic functions in squamous cancers is still not fully understood. Here, we report that in addition to controlling transcriptional programmes that determine the balance between proliferation and terminal differentiation, YAP also engages with RIF1, a key regulator of DNA replication timing and protector of stalled replication forks under replication stress. YAP modulates gene expression of RIF1 via TEAD transcription factors and also stabilizes RIF1 protein on the chromatin. YAP-RIF1 complex formation increases in response to exogenous replication stress, and treatment with hydroxyurea to induce replication fork stalling acts synergistically with YAP depletion to impair cell proliferation. Our results thus demonstrate that YAP's oncogenic functions in squamous cell carcinoma involve both transcriptional and non-transcriptional mechanisms, and that RIF1 is key for squamous cell carcinoma cells to survive with their high levels of endogenous replication stress.

Introduction

Squamous cancers develop in squamous (also called 'stratified') epithelia and are by far the most frequently diagnosed solid tumours globally, with incidences continuing to rise (Dotto & Rustgi, 2016). Common risk factors for developing squamous cell carcinoma (SCC) are smoking, alcohol, and viral infections (human papilloma virus and Epstein-Barr virus)(Dotto & Rustgi, 2016). SCC of the skin epidermis (cutaneous SCC; cSCC) is the most common type of squamous cancer, and a significant burden to health care systems world-wide due to its very high incidence (Winge *et al*, 2023). The major risk factor for cSCC development is life-long

chronic exposure to UV radiation in sunlight (Dotto & Rustgi, 2016; Winge *et al.*, 2023). In contrast, SCCs originating in the head and neck region (HNSCC), which include squamous cancers of the oral cavity, oropharynx, nasopharynx, hypopharynx, and larynx, are less common, but are associated with a far higher mortality rate (Johnson *et al*, 2020). This is due to their aggressiveness and high risk of progression to metastatic disease (Johnson *et al.*, 2020). There is ample evidence that the cells of origin of SCCs are the stem and progenitor cells which are located in the deepest tissue layers and maintain and repair squamous epithelia during the life course (Sanchez-Danes & Blanpain, 2018). Tissue homeostasis of the highly proliferative squamous epithelial tissues is maintained by a tightly controlled balance of cell proliferation and terminal differentiation (Flora & Ezhkova, 2020). Proliferating cells that have committed to undergoing terminal differentiation withdraw from the cell cycle and undergo a programmed series of biochemical and morphological changes whilst moving towards the epithelial surface (Blanpain & Fuchs, 2009). In well differentiated SCCs the terminal differentiation programme continues to be executed to some extent, often giving rise to regions with concentric layers of differentiated cancer cells called 'keratin pearls' (Dotto & Rustgi, 2016; Yanofsky *et al*, 2011). It is widely understood that the ability of SCC cells to undergo terminal differentiation acts as a 'brake' to tumour progression (Dotto & Rustgi, 2016; Johnson *et al.*, 2020; Winge *et al.*, 2023). Accordingly, in poorly differentiated SCCs the cancer cells have lost the ability to undergo terminal differentiation, which contributes to the rapid growth and increased aggressiveness of such tumours (Johnson *et al.*, 2020; Winge *et al.*, 2023). Lung squamous cell carcinoma (LUSC) is a form of non-small cell lung cancer, and contrary to other types of SCC, develops through acquisition of a squamous differentiation programme of the basal stem/progenitor cells in the otherwise pseudo-stratified epithelium

69 covering the trachea and the airways, or by trans-differentiation of a lung adenocarcinoma
70 into a LUSC (Hou *et al*, 2017; Lau *et al*, 2022).

71 Like other cancers, SCC arises from genetic alterations that invariably lead to dysregulated
72 transcriptional programmes (Dotto & Rustgi, 2016; Johnson *et al.*, 2020; Ratushny *et al*, 2012;
73 Winge *et al.*, 2023). These dysregulated programmes can cause cancer cells to become highly
74 dependent on certain regulators of gene expression (Bradner *et al*, 2017). Such transcriptional
75 dependencies are not typically identified by cancer genome sequencing but arise through
76 focused mechanistic studies of gene control programmes operating in both normal and
77 neoplastic cells (Bradner *et al.*, 2017). The closely related transcriptional co-regulators Yes-
78 associated protein (YAP; gene symbol: *YAP1*) and transcriptional co-activator with PDZ-
79 binding motif (TAZ, also called WW Domain Containing Transcription Regulator 1 (*WWTR1*))
80 have surfaced as essential drivers of cancer initiation, progression and metastasis in many
81 tumour types, including SCC (Franklin *et al*, 2023; Howard *et al*, 2022; Maehama *et al*, 2021;
82 Piccolo *et al*, 2023). YAP/TAZ do not bind DNA directly, but rely on the interaction with
83 different transcription factors (TFs; predominantly those of the TEAD family (Battilana *et al*,
84 2021; Franklin *et al.*, 2023; Piccolo *et al.*, 2023)) and associated cofactors (e.g. bromodomain-
85 containing protein 4 (BRD4) (Zanconato *et al*, 2018) and the BRG1- or BRM-associated factors
86 (BAF)-type SWItch/Sucrose Non-Fermentable (SWI/SNF) chromatin regulation complex
87 (Chang *et al*, 2021)) to bind to enhancer and super-enhancer elements (large chromatin
88 domains bountiful in cell-type specific TF binding motifs that enable cooperative binding of
89 TFs) to drive the execution of transcriptional programmes that promote proliferation,
90 chemoresistance, epithelial-to-mesenchymal transition (EMT), and metastasis (Dey *et al*,
91 2020; Franklin *et al.*, 2023; Piccolo *et al.*, 2023). YAP/TAZ can operate as both transcriptional
92 co-activators and co-repressors (Hillmer & Link, 2019). Although YAP/TAZ are classified as

93 oncoproteins (http://ongene.bioinfo-minzhao.org/browse_gene.html), activating mutations
94 of YAP/TAZ are rarely identified (Zhang *et al*, 2019). Instead, activation of YAP/TAZ occurs
95 through de-regulation of upstream inhibitory signalling pathways, leading to increased
96 nuclear YAP/TAZ accumulation and consequently, chromatin binding and downstream
97 signalling (Battilana *et al.*, 2021; Dey *et al.*, 2020; Franklin *et al.*, 2023; Piccolo *et al.*, 2023). In
98 addition to the well documented transcriptional functions of YAP/TAZ, evidence for non-
99 transcriptional roles has also begun to emerge (Bui *et al*, 2016; Chow *et al*, 2023). Intriguingly,
100 a recent study demonstrated that YAP regulates DNA replication during early stages of
101 *Xenopus* development, when transcription is still largely absent (Melendez Garcia *et al*, 2022).
102 Studies in mice have demonstrated an absolute requirement of YAP/TAZ for initiation and
103 progression of both cSCC and HNSCC (Debaugnies *et al*, 2018; Omori *et al*, 2020; Vincent-
104 Mistiaen *et al*, 2018; Zanconato *et al*, 2015), while YAP/TAZ appear to be largely dispensable
105 for normal squamous epithelial tissue homeostasis (Elbediwy *et al*, 2016; Omori *et al.*, 2020;
106 Zanconato *et al.*, 2015). This highlights the possibility that targeting YAP/TAZ in SCC may
107 display a large therapeutic window (Howard *et al.*, 2022; Maehama *et al.*, 2021).

108 One of the hallmarks of cancer cells is their ability to sustain chronic proliferation (Hanahan &
109 Weinberg, 2011). Since oncogene expression drives cancer cell proliferation by interfering
110 with the regulatory pathways of cell cycle progression control, cancer cells usually experience
111 replication stress, which occurs when DNA replication fork progression in S phase slows or
112 stalls (da Costa *et al*, 2023; Gaillard *et al*, 2015). This leads to the collapse of forks into DNA
113 double-strand breaks (DSBs), as well as incomplete sister chromatid separation in the
114 following mitosis, and ultimately genomic instability (da Costa *et al.*, 2023; Gaillard *et al.*,
115 2015). In addition to de-regulated cell cycle control, another source of replication stress is the

upregulation of transcription, which can cause direct collisions or torsional stress between the transcriptional and replication machineries as well as collisions with RNA-DNA hybrids (R loops) (Bowry *et al*, 2021; Gaillard *et al.*, 2015). As endogenous replication stress is higher in cancer cells, they depend on replication stress response and DNA damage response (DDR) pathways for survival (Ashley *et al*, 2014; da Costa *et al.*, 2023; Liu *et al*, 2012). Markers of endogenous replication stress have been found in tumour samples and cells expressing active oncogenes (Bartkova *et al*, 2006; Burrell *et al*, 2013; Takahashi *et al*, 2022). Of note, the stem and progenitor cells in healthy human epidermis already have high levels of endogenous replication stress due to their high proliferation rates, and the resulting activation of DDR pathways directly couples replication stress to polyploidisation and terminal differentiation as a homeostatic mechanism (Contreras *et al*, 2024; Molinuevo *et al*, 2020). This mechanism is mediated by G2 and mitotic checkpoints that determine the fate of epidermal stem/progenitor cells towards differentiation or apoptosis (de Pedro *et al*, 2021; Freije *et al*, 2012; Freije *et al*, 2014). Importantly, the same mechanism operates to eliminate pre-cancerous cells in the epidermis in response to activation of oncogenic signalling ('oncogene-induced differentiation' (Gandarillas, 2012)), such as overexpression of MYC or Cyclin E (*CCNE1*) (Freije *et al.*, 2012; Gandarillas *et al*, 2000), or inactivation of TP53 (Freije *et al.*, 2014). The key cell cycle regulator p21 (*CDKN1A*) is a transcriptional target of TP53, but squamous epithelial cells (keratinocytes) also express a pool of p21 that is regulated in a TP53-independent fashion (de Pedro *et al.*, 2021; Freije *et al.*, 2014). Interestingly, depletion of this TP53-independent pool of p21 was shown to alleviate the differentiation response caused by knockdown of TP53, allowing DNA-damaged keratinocytes to escape differentiation and continue to proliferate (de Pedro *et al.*, 2021). Intriguingly, several studies have reported that reduced p21 expression inversely correlates with cell proliferation and invasion in HNSCC

140 patient samples (Li *et al*, 2015a; Xie *et al*, 2002), suggesting that suppression of p21 may be
141 an important step in human SCC progression similar to what was reported in mice (Topley *et*
142 *al*, 1999). While YAP plays an essential role in stimulating proliferation of human epidermal
143 stem cells in response to tissue injury (De Rosa *et al*, 2019; Walko *et al*, 2017), overexpression
144 of an oncogenic, hyperactive YAP variant in these cells was found to induce rapid senescence
145 (De Rosa *et al.*, 2019). It is likely that this oncogene-induced senescence mechanism is linked
146 to YAP-driven transcription and the resulting replication stress, similar to what was reported
147 in neuronal progenitors upon YAP/TAZ activation (Lavado *et al*, 2018).

148 How YAP/TAZ control oncogenic signalling in SCC at the molecular level, and how SCC cells
149 deal with YAP/TAZ hyperactivation-induced replication stress remains poorly understood.
150 Here, by characterising the YAP-controlled transcriptome and the protein interactome of
151 chromatin-associated YAP, we have identified transcriptional and non-transcriptional
152 mechanisms that underly YAP's oncogenic functions in SCC, including engagement of the DNA
153 replication and damage repair factor RIF1 to dampen replication stress.

154

155 **Results**

156 ***The protein interactome of chromatin-associated YAP in squamous cell carcinoma cells.***

157 To characterise the protein interactome of transcriptionally engaged, chromatin-associated
158 YAP in SCC cells, we chose SCC13 as a relevant cell model. SCC13 cells are a widely used human
159 cSCC cell line and are derived from the rapid recurrence of a cSCC (T2N0) in a patient's facial
160 epidermis following radiotherapy (Rheinwald & Beckett, 1981; Weichselbaum *et al*, 1984). As
161 is typical for cSCC, SCC13 cells carry an inactivating mutation in *TP53* (p.Glu258Lys (c.772G>A)
162 (Burns *et al*, 1993; Nappi *et al*, 2023). SCC13 are representative of a subclass of cSCC with

163 reduced expression of αE-catenin (Schlegelmilch *et al*, 2011; Walko *et al.*, 2017), which likely
164 explains the constitutive nuclear localisation of YAP/TAZ in these cells and their strong YAP-
165 dependency (Walko *et al.*, 2017). Like most cSCC cell lines, SCC13 require feeder layer support
166 for optimal growth in culture (Hassan *et al*, 2019; Rheinwald & Beckett, 1981).

167 Rapid immunoprecipitation mass spectrometry of endogenous protein (RIME) analysis
168 (Mohammed *et al*, 2016) was performed on two independent cultures of SCC13 cells and
169 normal human epidermal keratinocytes (NHK, strain Km), using a knockdown-validated YAP-
170 specific antibody that does not recognise TAZ (Supplementary Figs. 1A and 2D) and isotype-
171 matched IgG as control. Low passage cells were cultured on a mitotically inactivated fibroblast
172 feeder layer to maintain the stem cell state of NHKs characterised by predominantly nuclear
173 localisation of YAP (Supplementary Fig. 1B) (De Rosa *et al.*, 2019; Walko *et al.*, 2017). YAP
174 immunoprecipitation (IP) was performed on formaldehyde-fixed chromatin fractions of SCC13
175 and NHK cells. IP efficiency was consistently high across all YAP-RIME replicates, with high YAP
176 peptide coverage (63-65%) detected by mass spectrometry analysis (Supplementary Fig. 1C),
177 and with zero spectral counts (MS/MS events, total number of spectra associated to a single
178 protein or protein group) for YAP in the IgG-control IPs (Supplementary Dataset 1). Proteins
179 detected by mass spectrometry in the YAP IPs (Supplementary Dataset 1 – Table 1) were
180 stringently filtered (see Materials and Methods, and Supplementary Dataset 1 – Tables 2–7)
181 to remove potential false positive hits and to compile a list of high confidence interactors of
182 chromatin-associated YAP in SCC13 and NHK cells (Supplementary Dataset 1 – Tables 6, 7).
183 YAP-RIME enabled identification of 48 high confidence YAP-interacting proteins in SCC13 cells
184 (Fig. 1A, Supplementary Dataset 1 – Table 6) and 15 high confidence YAP-interacting proteins
185 in NHK cells (including the bait protein YAP in both cases) (Supplementary Fig. 2A,
186 Supplementary Dataset 1 – Table 7). Using the 'Compartments' database

187 (https://compartments.jensenlab.org/Search), most identified proteins had a high confidence
188 score (≥4) for nuclear localization (Supplementary Dataset 1 – Tables 6, 7). Moreover,
189 significantly enriched gene ontology terms for molecular functions (GO MF) and biological
190 processes (GO BP) in both protein interactomes were all related to processes occurring in the
191 nucleus (Fig. 1B, Supplementary Fig. 2B). This confirms that, as expected, the YAP-RIME
192 predominantly identified protein interactions of YAP on the chromatin.

193 STRING analysis was used to identify known interactions occurring between the YAP-
194 interacting proteins in SCC13 (Fig. 1A) and NHK (Supplementary Fig. 2A) cells, and proteins
195 were manually grouped by cellular function (Szklarczyk *et al*, 2019). Because our aim was to
196 identify proteins that facilitate YAP's functions in squamous cancers, we focused on the
197 protein interactome of chromatin-associated YAP in SCC13 cells. Among these YAP-interacting
198 proteins were several known regulators of YAP, including Neurofibromatosis type (NF2, also
199 called Merlin) (Zhang *et al*, 2010), Angiomiotin-like 1 (AMOTL1), PPP1CB, one the catalytic
200 subunits of protein phosphatase 1 (PP1) (Wang *et al*, 2011), and Prolyl 4-Hydroxylase subunit
201 alpha 2 (P4HA2). The identification of NF2 in the interactome of chromatin-bound YAP was, at
202 first look, at odds with the established dogma that the canonical Hippo signalling pathway
203 operates in the cytoplasm. However, nuclear localization of NF2 has been widely documented
204 (Beltrami *et al*, 2013), and nucleocytoplasmic shuttling of NF2 has been implicated in YAP
205 regulation (Furukawa *et al*, 2017; Li *et al*, 2014; Moleirinho *et al*, 2017). AMOTL1, a member
206 of the Motin protein family (Amirifar & Kissil, 2023), was previously shown to enhance YAP
207 stability and to help translocate YAP into the nucleus (Ragni *et al*, 2017; Zhou *et al*, 2020).
208 P4HA2 was shown to hydroxylate YAP at multiple proline residues, with implications in cell
209 migration and invasion (Zhu *et al*, 2021). Consistent with the results from a previous study
210 which used a similar YAP chromatin-IP/mass spectrometry approach (Chang *et al*, 2018), our

211 YAP-RIME also identified five subunits of the BAF-type SWI/SNF chromatin remodelling
212 complex (Mittal & Roberts, 2020) in the interactome of chromatin-associated YAP in SCC13
213 cells. These included the YAP binding partner AT-rich interactive domain-containing protein
214 1A (ARID1A), and SWI/SNF-related matrix-associated actin-dependent regulator of chromatin
215 (SMARC) subfamily A member 4 (SMARCA4, also called BRG1), subfamily E member 1
216 (SMARCE1), subfamily D member 2 (SMARCD2), and subfamily C member 1 (SMARCC1) (Fig.
217 1A). Two key components of the NuRD chromatin remodelling complex, Chromodomain-
218 helicase-DNA-binding protein 4 (CHD4) and Metastasis Associated 1 Family Member 2
219 (MTA2), were also identified as interactors of chromatin-bound YAP in SCC13 cells. Of note,
220 the NuRD complex was previously implicated in mediating co-repressor functions of YAP (Kim
221 *et al*, 2015). While key components of the general transcriptional machinery (POLR2A,
222 POLR2B, GTF21, TOP1) were present in the SCC13 YAP interactome, TEAD TFs were notably
223 absent (Fig. 1A). A closer inspection of our mass spectrometry data revealed that TEADs, as
224 well as other known YAP-interacting transcription factors, such as JunB and TP63 (He *et al*,
225 2021; Ning *et al*, 2023), had been identified but did not pass our stringent bioinformatics
226 filtering criteria (Supplementary Dataset 1 – Table 4). The overall poor identification of TFs by
227 our YAP-RIME was likely due to their insufficient crosslinking to the DNA by formaldehyde
228 alone, as previously observed for the highly dynamic transcription factor NFκB (Nowak *et al*,
229 2005).

230 To identify physiologically relevant interactions, the YAP-interacting proteins identified by
231 RIME in SCC13 were also compared to candidate positive and negative regulators of cell
232 proliferation and survival identified in a genome-wide RNA interference screen that had
233 previously been performed in the same cell lines (Walko *et al.*, 2017). This revealed that 22

234 out of the 47 high confidence YAP-interacting proteins in SCC13 cells were likely relevant for
235 cell proliferation and/or survival (Fig. 1A, Supplementary Dataset 1 – Table 8).
236
237 ***A fraction of chromatin-associated YAP interacts with RIF1.***

238 Our attention was drawn to RIF1, a key regulator of DNA replication timing and DDR (Alver *et*
239 *al*, 2017; Buonomo *et al*, 2009; Cornacchia *et al*, 2012; Foti *et al*, 2016; Gnan *et al*, 2021; Hiraga
240 *et al*, 2017; Moiseeva *et al*, 2019; Mukherjee *et al*, 2019; Yamazaki *et al*, 2012). An involvement
241 of RIF1 in transcription regulation has been reported previously (Liu *et al*, 2023; Yoshizawa-
242 Sugata *et al*, 2021). RIF1 was detected as a YAP-interacting protein in both the SCC13 and NHK
243 YAP-RIME experiments (Fig. 1A; Supplementary Fig. 2A) with a much stronger enrichment in
244 the SCC13 cells (Supplementary Fig. 2C, Supplementary Dataset 1 – Tables 6, 7). Of note,
245 PPP1CB, one of the three catalytic subunits of PP1—a key effector of RIF1 (Alver *et al.*, 2017;
246 Gnan *et al.*, 2021; Hiraga *et al.*, 2017; Moiseeva *et al.*, 2019), was also present in the SCC13
247 YAP-RIME (Fig. 1A; Supplementary Dataset 1 – Table 6). Like YAP, RIF1 featured among the
248 positive regulators of cell proliferation and survival of SCC13 cells identified in a genome-wide
249 RNA interference screen (Walko *et al.*, 2017)(Fig. 1A; Supplementary Dataset 1 – Table 8). As
250 expected, YAP and RIF1 were both localised in the nucleus of SCC13 cells (Fig. 1C) and were
251 present in chromatin fractions (Supplementary Fig. 2D), confirming their chromatin-
252 association. To biochemically validate the YAP-RIF1 interaction identified by RIME, co-IP
253 experiments were performed under native non-cross-linking conditions using a different YAP-
254 specific antibody that also does not detect TAZ (Supplementary Fig. 3A). Indeed, RIF1 could be
255 immunoprecipitated together with YAP from both, whole-cell detergent extracts and nuclei-
256 enriched fractions (Fig. 1D, E). Further validating our RIME results, CHD4 and ARID1A also co-
257 immunoprecipitated with YAP under native conditions. We also found that under these

258 conditions, TEAD transcription factors could be immunoprecipitated together with YAP (Fig.
259 1E). Of note, compared to the TEADs, smaller amounts of RIF1, ARID1A, and CHD4 co-
260 immunoprecipitated with YAP from nuclei-enriched fractions, possibly indicating weaker
261 interactions of these proteins with YAP. Indeed, significantly more RIF1 co-
262 immunoprecipitated with YAP under milder lysis conditions (Fig. 1D). In-situ proximity ligation
263 assays (PLA) confirmed YAP-RIF1 interactions in the nucleus of SCC13 cells (Fig. 1F). The YAP-
264 RIF1 PLA signal was significantly decreased upon YAP/TAZ knockdown. To achieve a sufficient
265 knockdown of both YAP and TAZ we combined our doxycycline-inducible YAP-targeting shRNAs
266 with an siRNA pool targeting YAP and TAZ (Fig. 1F, Supplementary Fig. 3B). Consistent with our
267 co-IP results, YAP was also found in very close proximity to TEAD1 in the nucleus of SCC13 cells
268 by PLA (Fig. 1G). The YAP-RIF1 PLA signal was completely absent when either both or one of
269 the two primary antibodies were omitted during the experiments (Supplementary Fig. 3C, D),
270 and was also largely absent from mitotic chromosomes (Supplementary Fig. 3E). To test if the
271 YAP-RIF1 interaction also occurred in other types of SCC, we used the lung SCC cell line HARA
272 (Liu *et al*, 2020). YAP and RIF1 co-expression in HARA cell nuclei was confirmed by
273 immunofluorescence microscopy (Supplementary Fig. 3F). Co-IP was performed with nuclei-
274 enriched HARA cell fractions treated with Benzonase nuclease to enzymatically digest DNA
275 and RNA (Supplementary Fig. 3G, H), demonstrating that YAP and RIF1 interact on the
276 chromatin and are not co-immunoprecipitated because of a DNA bridge between the two
277 proteins. In summary, our results show that RIF1 is a binding partner of chromatin-associated
278 YAP in NHKs and cutaneous and lung SCC cells.
279
280 ***YAP/TAZ-mediated oncogenic signalling controls the balance between proliferation and***
281 ***differentiation and contributes to replication stress in squamous cell carcinoma cells.***

282 In normal epidermal keratinocytes, but also in basal cell carcinoma (BCC) cells, YAP/TAZ control
283 the transcription of genes driving cell proliferation and survival through TEAD transcription
284 factors and suppress the expression of genes promoting terminal differentiation through
285 TEAD-independent mechanisms (Yuan *et al*, 2020; Yuan *et al*, 2021). To test if YAP/TAZ execute
286 similar transcriptional programmes in cSCC, and to investigate a potential involvement of RIF1
287 in YAP/TAZ-mediated transcriptional regulation, we performed bulk RNAseq analysis on
288 samples of SCC13 cells with acute (48 hours) siRNA-mediated knockdown of either YAP/TAZ
289 or RIF1 (siY/T, siRIF1; Fig. 2A, Fig. 3A). We were unable to robustly deplete TAZ(WWTR1) (Fig.
290 2A), but the TAZ-targeting siRNA pool was able to block compensatory upregulation of TAZ in
291 response to YAP knockdown (Supplementary Fig. 3B) (Walko *et al.*, 2017). DESeq2 analysis
292 revealed a large number of differentially expressed genes (DEGs) upon siY/T treatment (977
293 DEGs downregulated, 2,209 DEGs upregulated; $p<0.05$, FC>1.5; Supplementary Dataset 2 -
294 Tables 1–3). Gene set enrichment analysis (GSEA) revealed significant enrichment of pathways
295 associated with cell cycle regulation, DNA replication, and mitosis among the downregulated
296 DEGs, and of pathways associated with keratinization, cornification, extracellular matrix (ECM)
297 remodelling, and immunoregulation among the upregulated DEGs upon siY/T treatment (Fig.
298 2C; Supplementary Fig. 4A, B; Supplementary Dataset 2 - Tables 4–6). DEGs downregulated
299 upon siY/T comprised both, genes known to be positively regulated by YAP/TAZ in cooperation
300 with TEADs (Zanconato *et al.*, 2015), as well as genes known to be regulated by YAP/TAZ in
301 cooperation with the Myb-MuB (MMB) complex (Jessen *et al*, 2024; Pattschull *et al*, 2019)
302 (Supplementary Fig. 4C; Supplementary Dataset 2 – Tables 10, 11). YAP/TAZ knockdown in
303 SCC13 also led to increased terminal differentiation which was evident from (i) enrichment of
304 an epidermal terminal differentiation gene signature (Lopez-Pajares *et al*, 2015) in the
305 upregulated DEGs and of an epidermal progenitor cell signature (Lopez-Pajares *et al.*, 2015)

306 in the downregulated DEGs (Supplementary Fig. 4D), and (ii), upregulation of genes belonging
307 to the epidermal differentiation complex (EDC) (Kypriotou *et al*, 2012), as well as
308 transcriptional regulators of terminal differentiation (Fig. 2C; Supplementary Dataset 2 –
309 Tables 13, 14). These data suggest that YAP/TAZ regulate terminal differentiation indirectly by
310 supressing the transcription of key regulators of the terminal differentiation programme, and
311 that this function is conserved between normal keratinocytes and neoplastic keratinocytes of
312 both BCC (Yuan *et al.*, 2021) and cSCC. In accordance with the detected transcriptomic
313 changes, we observed that cell proliferation was impacted in SCC13 cells upon expression of
314 doxycycline-inducible YAP-targeting shRNAs (shYAP) (Fig. 2C). This was evident from reduced
315 levels of Ser10-phosphorylated histone H3, a marker of mitotic cells, and strong upregulation
316 of p21 (Fig. 2D). Consistent with the reduced expression of several key regulators of DNA
317 replication (Supplementary Fig. 4C; Supplementary Dataset 2 – Table 15), shYAP SCC13 cells
318 arrested in G1 and progressed much slower through S phase (Fig. 2E). Compromised cell cycle
319 progression and increased terminal differentiation led to reduced clonal growth of shYAP
320 SCC13 cells (Fig. 2F).

321 Reduced activation of the replication stress checkpoint (phosphorylation of CHK1 on Ser317;
322 (Ashley *et al.*, 2014; Liu *et al.*, 2012)) was evident in SCC13 cells upon induction of shYAP (Fig.
323 2G), while depletion of either YAP or TAZ in SCC13 cells reduced accumulation of replication
324 stress-induced DNA DSBs, marked by decreased γH2Ax expression (de Pedro *et al.*, 2021;
325 Freije *et al.*, 2014; Liu *et al.*, 2012; Molinuevo *et al.*, 2020) (Fig. 2G). Furthermore, using mRNA
326 expression data from the DepMap project (https://depmap.org/portal/), we discovered a
327 strong correlation between the expression of a replication stress signature (Takahashi *et al.*,
328 2022) and an in-house generated SCC-specific YAP/TAZ activity signature comprising 10
329 YAP/TAZ target genes (Supplementary Dataset 2 – Table 16) from our SCC13 RNAseq dataset

330 in a panel of 64 HNSCC cell lines (Supplementary Fig. 5A–D). Together, these findings
331 indicated that YAP/TAZ-driven oncogenic signalling contributed to the endogenous
332 replication stress of SCC cells.
333 Of note, reduced cell proliferation was reversible upon doxycycline withdrawal
334 (Supplementary Fig. 6), demonstrating that YAP knockdown slows down cell cycle progression,
335 but does not cause permanent growth arrest. The effects of shTAZ on SCC13 proliferation were
336 less dramatic (Fig. 2D, F). We conclude that, like in NHKs, YAP/TAZ regulate the balance
337 between proliferation and terminal differentiation also in cSCC cells, thereby promoting a
338 highly proliferative and undifferentiated cell state.

339 We next used the YAP/TAZ target gene expression signature derived from our RNA-seq data to
340 perform gene set variation analysis (GSVA; see materials and methods) on one of the largest
341 bulk RNA-seq datasets from patients with cSCC (237 patients) (Wang *et al*, 2023). This revealed
342 that genes that are positively regulated by YAP/TAZ in SCC13 cells are expressed significantly
343 higher in cSCC tumours (as well as their perilesional skin tissue) that have progressed to
344 metastatic disease, compared to those cSCC tumours that have not (Supplementary Fig. 7A).
345 Genes that were positively regulated by YAP/TAZ in SCC13 cells were also highly expressed in
346 cSCC metastases (Supplementary Fig. 7A). Conversely, genes that were negatively regulated
347 by YAP/TAZ in SCC13 cells displayed significantly reduced expression in cSCC metastases
348 (Supplementary Fig. 7B). This finding provides intriguing evidence for the involvement of
349 YAP/TAZ in the metastatic progression of human cSCC.
350

351 ***RIF1 is not directly involved in YAP/TAZ-controlled transcription.***

352 Compared to siY/T treatment, knockdown of RIF1 affected the expression of a smaller number
353 of genes (Fig. 3A). 165 DEGs (of which 33 are protein-coding) were downregulated, and 942

354 DEGs (of which 749 are protein-coding) were upregulated ($p<0.05$, FC>1.5; Fig. 3A,
355 Supplementary Dataset 2 - Tables 1–3). GSEA revealed that theses DEGs were predominantly
356 involved in cell cycle regulation, although the statistical significance of pathway enrichment
357 was generally quite low (Supplementary Fig. 8A–C; Supplementary Dataset 2 - Tables 7–9).
358 Interestingly, 710 out the 782 differentially expressed protein-encoding genes upon siRIF1
359 knockdown appeared to be co-regulated by YAP/TAZ, since the observed expression changes
360 were going into the same direction in both siRIF1 and siY/T experiments (Fig. 3B). However,
361 GSEA did not reveal any significantly enriched pathways (data not shown) among these
362 putative RIF1 and YAP/TAZ co-regulated genes. This is reminiscent of findings in mouse
363 embryonic stem cells, where limited gene expression changes in response to *Rif1* knockout
364 could neither be linked to any specific functions/pathways nor to the genome-wide
365 distribution of Rif1 on the chromatin (Foti *et al.*, 2016). Instead, the gene expression changes
366 in response to *Rif1* knockout were suggested to be effects that are secondary to changes in
367 DNA replication timing (Cornacchia *et al.*, 2012; Foti *et al.*, 2016). Accordingly, an intriguing
368 possibility is that the observed expression changes of those genes that appear to be co-
369 regulated by YAP/TAZ and RIF1 in SCC13 cells are the consequence of altered replication timing
370 (Fig. 6 and text below) and changes to YAP/TAZ chromatin accessibility, and not of a direct
371 involvement of RIF1 in YAP/TAZ-regulated transcription.
372
373 ***YAP modulates RIF1 transcription and promotes RIF1 protein stability.***
374 Our RNAseq analysis revealed that *RIF1* mRNA expression was moderately downregulated in
375 response to siY/T knockdown (Fig. 2A), and a similar trend could be confirmed in independent
376 siY/T samples by RT-qPCR analysis (Fig. 3C). Accordingly, RIF1 protein expression was slightly
377 lower in siY/T compared to siNTC SCC13 cells (Fig. 3D) and was more strongly reduced in

378 shYAP and shTAZ cells with a more prominent depletion of YAP or TAZ protein (Fig. 3E). Lowest
379 RIF1 protein levels were observed in shYAP and shTAZ cells where compensatory upregulation
380 of the other paralogue was only moderate (shYAP-2, shTAZ-1; Fig. 3E). Analysis of published
381 RNAseq data of siY/T in N/TERT-2G immortalized human keratinocytes (Yuan *et al.*, 2020)
382 revealed that this relationship was conserved also in NHKs (Fig. 3F). Moreover, we observed
383 a significant correlation between *RIF1* mRNA expression and single-sample enrichment scores
384 of a generic Hippo/YAP/TAZ pathway gene signature in a panel of 64 HNSCC cell lines using
385 the DepMap portal (https://depmap.org/portal/) (Dempster *et al*, 2019) (Fig. 3G). An even
386 stronger correlation was observed when we used our in-house generated SCC-specific YAP
387 activity signature (Supplementary Dataset 2 – Table 16, Supplementary Fig. 5C, F).
388 Summarized, RIF1 expression closely correlates with YAP/TAZ transcriptional activity in both
389 normal and neoplastic human keratinocytes.

390 Combined siRNA-mediated knockdown of TEAD1, 3, and 4 (siTEAD1/3/4) in SCC13 cells
391 reduced RIF1 protein to levels similar to those observed in siY/T cells (Fig. 3H), indicating that
392 YAP modulates *RIF1* transcription through TEADs. Since our biochemical experiments had
393 revealed direct binding of YAP and RIF1 proteins, we also tested if this interaction additionally
394 stabilizes RIF1 protein. Indeed, by combining shYAP with cycloheximide treatment to stop
395 protein translation, we could reduce RIF1 protein expression in SCC13 cells to levels below
396 the detection limit of our chemiluminescence imaging system (Fig. 3I). Interestingly, YAP
397 protein levels remained stable during the treatment time course and were even upregulated
398 during the first 4 hours of cycloheximide treatment. This suggests that YAP protein
399 homeostasis is precisely fine-tuned in SCC cells. We conclude that YAP modulates *RIF1*
400 transcription trough TEADs, but additionally stabilizes RIF1 protein on the chromatin through
401 a direct interaction.

402

403 ***Increased association of YAP with RIF1 in response to replication stress.***

404 Our discovery of RIF1 as a YAP interaction partner in NHK and SCC cell lines raised the exciting
405 possibility that in normal and cancerous squamous epithelial tissues YAP could have dual,
406 transcriptional and non-transcriptional roles. In *Xenopus laevis* embryos, the YAP-RIF1
407 complex was previously shown to control the dynamics of DNA replication by limiting
408 replication origin firing (Melendez Garcia *et al.*, 2022). Using *Xenopus* egg extracts, a classical
409 model for studying DNA replication, Melendez Garcia et al. (Melendez Garcia *et al.*, 2022)
410 showed that *Xenopus* YAP became recruited onto the chromatin upon S phase induction,
411 following the formation of the pre-replication complex and in parallel with PCNA (proliferating
412 cell nuclear antigen) loading (Melendez Garcia *et al.*, 2022). Here, we used a double thymidine
413 block to arrest human SCC13 cells at the G1/S phase boundary (Yamazaki *et al.*, 2012) and
414 assessed the levels of YAP on the chromatin upon S phase entry following thymidine washout.
415 We noticed an increase in the amount of chromatin-bound YAP as SCC13 cells where entering
416 S phase that correlated with the increased loading of PCNA (Fig. 4A). Consistent with the
417 reduced expression of key DNA replication regulators in siY/T cells (Supplementary Fig. 4C;
418 Supplementary Dataset 2 – Table 15) and the slowed S phase progression of shYAP cells (Fig.
419 2E), PCNA loading onto the chromatin was reduced in shYAP cells (Fig. 4A). Only a very limited
420 number of YAP-RIF1 PLA speckles overlapped with replication foci, marked by DNA
421 incorporation of EdU during a 1-hour pulse (Fig. 4B), suggesting that YAP is not associated
422 with nascent chromatin behind the replication fork. Moreover, only very few YAP-RIF1 PLA
423 speckles were present on the DNA of mitotic cells (Fig. 4C), consistent with the absence of
424 RIF1 from mitotic chromosomes (Atemin *et al*, 2024; Yamazaki *et al.*, 2012).

425 In addition to controlling origin firing and DNA replication timing, another key function of RIF1
426 is the protection of stalled replication forks from resection by nucleases in response to
427 replication stress and the promotion of replication restart (Alver *et al.*, 2017; Buonomo *et al.*,
428 2009; Garzon *et al*, 2019; Lebdy *et al*, 2023; Mukherjee *et al.*, 2019). To test if YAP might be
429 recruited to either stalled or collapsed replication forks, we treated SCC13 cells with 4 mM
430 hydroxyurea (HU) (Dungrawala *et al*, 2015; Petermann *et al*, 2010) for periods of up to 24
431 hours. As shown in Fig. 4D, this triggered strong activation of the replication stress checkpoint
432 (phosphorylation of CHK1 on Ser317; (Ashley *et al.*, 2014; Liu *et al.*, 2012)) and accumulation
433 of DNA DSBs, marked by γH2Ax expression (de Pedro *et al.*, 2021; Freije *et al.*, 2014;
434 Molinuevo *et al.*, 2020). Persisting γH2Ax expression following washout of HU indicated
435 accumulation of DNA damage at stalled and subsequently inactivated replication forks upon
436 24 hours of HU treatment (Petermann *et al.*, 2010) (Fig. 4D). While the YAP-RIF1 PLA signal
437 remained unchanged upon short-term HU treatment, it increased significantly after long-term
438 (24 hours) HU treatment (Fig. 4E). Moreover, upon long-term HU treatment, more YAP
439 molecules were found in close vicinity of γH2Ax by in-situ PLA (Fig. 4F), indicating that YAP
440 associates with RIF1 preferentially near DNA DSBs at insctivated replication forks.
441 Summarized, these data provided evidence that in SCC cells, a fraction of YAP is involved in
442 RIF1-mediated DDR at replication forks.
443
444 ***RIF1 is highly expressed in several types of squamous cell carcinoma and upregulated during***
445 ***tumour progression.***
446 The strong effect of YAP depletion on the cell cycle-regulatory transcriptome (Fig. 2,
447 Supplementary Fig. 4) and the resulting cell cycle exit and commitment to terminal
448 differentiation (Fig. 2B–F) precluded a further in-depth analysis of non-transcriptional YAP

449 functions specific to DNA replication. Consequently, we focused on RIF1 itself, given its
450 regulation by YAP (Fig. 3) and the previously unknown function(s) of RIF1 in SCC.

451 We first assessed RIF1 protein expression levels in a panel of human cSCC cell lines, which
452 also included an isogenic cSCC progression series (Proby *et al*, 2000). Increased expression of
453 RIF1 protein was notable in all cSCC cell lines when compared to NHKs, including a cell line
454 derived from a pre-malignant cSCC precursor lesion (PM1) (Proby *et al.*, 2000) (Fig. 5A).
455 Consistent with our findings that YAP controls RIF1 expression (Fig. 3), the protein levels of
456 RIF1 were highest in SCC13 cells featuring constitutively nuclear YAP (Supplementary Fig. 1B)
457 (Walko *et al.*, 2017) (as also indicated by a low ratio of S127-YAP to total YAP, Fig. 5A). All cSCC
458 lines in our panel, as well as the PM1 cells, displayed higher levels of γH2Ax compared to
459 NHKs, indicating elevated endogenous replication stress (Fig. 5A).

460 To investigate if increased RIF1 expression was a general hallmark of cancers originating from
461 epidermal keratinocytes, we next quantified the nuclear abundance of RIF1 protein in a tissue
462 array comprising cSCCs of different differentiation grades, as well as different types of BCCs
463 (Fig. 5B, C). There were increased number of RIF1-expressing cells within the keratin-positive
464 tumour cell masses of both BCC and cSCC compared to normal skin epidermis, in particular
465 within the more aggressive tumour types of infiltrative BCC and poorly differentiated cSCC
466 (Fig. 5B, C). The pattern of RIF1 expression in cSCC correlated well with the known localisation
467 of cycling cells, which are located at the periphery in well-differentiated tumours, but diffusely
468 distributed throughout the tumour mass in moderately/poorly-differentiated tumours (Al-
469 Hazmi *et al*, 2018; Stojkovic-Filipovic *et al*, 2018). By examining publicly available
470 immunohistochemistry data from the Human Protein Atlas (https://www.proteinatlas.org/),
471 we also observed increased numbers of RIF1-expressing tumour cells in HNSCC and cervical

472 SCC (CeSCC) (Supplementary Fig. 9A–C). To obtain a pan-cancer overview of RIF1 protein
473 expression levels, we used the UALCAN portal (https://ualcan.path.uab.edu/) (Chandrashekar
474 *et al*, 2022) to access protein expression data from the Clinical Proteomic Tumour Analysis
475 Consortium (CPTAC) (Zhang *et al*, 2022). This revealed increased RIF1 protein expression in
476 several cancer types (Supplementary Fig. 9D). Importantly, in HNSCC, RIF1 protein expression
477 increased with tumour grade (Fig. 5D). The UALCAN portal also allows assessment of the
478 impact of somatic alterations (small mutations or copy number alterations) in several
479 signalling pathways on the cancer proteome (Chandrashekar *et al.*, 2022; Zhang *et al.*, 2022).
480 The CPTAC data include somatic alterations in *NF2*/Merlin, *WWC1*, and *SAV1* as a proxy for
481 Hippo pathway alterations (Zhang *et al.*, 2022). WWC1 expression was previously shown to
482 strongly correlate with YAP activity in HNSCC (Saladi *et al*, 2017), and knockout of the Hippo
483 pathway scaffold proteins Sav1 or Mob1a/b in mice caused rapid YAP-driven squamous
484 carcinogenesis (Lee *et al*, 2008; Nishio *et al*, 2012; Omori *et al.*, 2020). *NF2* mutations have
485 been discovered in various types of SCC, with frequencies varying between 2.6% and 17%,
486 depending on study and cancer context (Chakravarthy *et al*, 2022; Ghias *et al*, 2019; Li *et al*,
487 2015b; Shin & Kim, 2020; Winer *et al*, 2006). Of note, a distinct tumour subtype with
488 alterations in Hippo pathway genes exists in CeSCC that also displays increased expression of
489 YAP/TAZ target genes (Chakravarthy *et al.*, 2022). Thus, in the context of human squamous
490 cancers, somatic alterations in *NF2*, *WWC1*, and *SAV1* can serve as reasonable indicators of
491 Hippo pathway activity status. We found that in both HNSCC (Fig. 5E) and LSCC
492 (Supplementary Fig. 9E) increased RIF1 protein expression predominantly correlated with
493 somatic Hippo pathway alterations in contrast to alterations in other signalling pathways,
494 implying altered Hippo pathway activity in the regulation of RIF1 expression. This agrees with
495 our finding that RIF1 is regulated by YAP at both the transcriptional and post-translational

496 levels (Fig. 3). Interestingly, in other cancer types, alterations in pathways other than Hippo
497 signalling also had a strong impact on increased tumour expression of RIF1 (Supplementary
498 Fig. 9F, G). Collectively, our multi-omics analysis confirmed a close relationship between
499 Hippo/YAP/TAZ signalling, replication stress, and RIF1 expression, and pointed towards a role
500 of RIF1 in squamous cell carcinogenesis.
501
502 ***Depletion of RIF1 causes increased origin firing in early S phase and accelerated S phase***
503 ***progression of squamous cell carcinoma cells.***
504 A highly conserved role of RIF1 is the genome-wide orchestration of DNA replication timing
505 (Cornacchia *et al.*, 2012; Gnan *et al.*, 2021; Klein *et al*, 2021; Melendez Garcia *et al.*, 2022;
506 Yamazaki *et al.*, 2012). Although the precise mechanisms are still not fully understood,
507 multiple pieces of evidence point to a scenario where RIF1 serves as a molecular hub that co-
508 regulates spatiotemporal replication patterns and nuclear architecture. Through its abilities
509 to bind multiple molecules of DNA and to interact with the nuclear lamina, RIF1 organizes
510 higher order chromatin structure into zones of coordinated DNA replication (RIF1-associated
511 domains) (Foti *et al.*, 2016; Gnan *et al.*, 2021; Klein *et al.*, 2021; Moriyama *et al*, 2018;
512 Yamazaki *et al.*, 2012). In addition, through its interaction with PP1, RIF1 was shown to
513 suppress the firing of late replicating origins within RIF1-associated domains by preventing
514 MCM subunit phosphorylation through Dbf4-dependent kinase (DDK; composed of Cdc7
515 kinase and its activator, Dbf4; MCM, minichromosome maintenance complex, core of the
516 replicative helicase containing six subunits MCM2-7), thereby antagonizing the activation of
517 the CMG (Cdc45–MCM–GINS) helicase complex (Alver *et al.*, 2017; Hiraga *et al.*, 2017;
518 Moiseeva *et al.*, 2019; Yamazaki *et al.*, 2012).

519 Consistent with a role of RIF1 in controlling S phase progression of SCC cells, we observed that
520 on release from a double thymidine block, shRIF1 SCC13 cells progressed more rapidly
521 through S phase (Fig. 6A). The phosphorylation levels of MCM2 and MCM4 proteins, targets
522 of the Cdc7 kinase (Alver *et al.*, 2017; Yamazaki *et al.*, 2012), were increased in RIF1-depleted
523 SCC13 cells in a RIF1 dosage-dependent manner (Fig. 6B), particularly in early S phase (Fig.
524 6C), indicating alterations in the dynamics of origin firing (Alver *et al.*, 2017; Hiraga *et al.*,
525 2017; Moiseeva *et al.*, 2019; Yamazaki *et al.*, 2012). Accordingly, chromatin loading of PCNA,
526 which is required for DNA replication after the action of Cdc7, was also increased during the
527 early S phase of shRIF1 SCC13 cells (Fig. 6C). Therefore, the faster progression of SCC13 cells
528 through S phase after RIF1 depletion likely reflects an increase in DNA replication initiation
529 events in early S phase (Alver *et al.*, 2017; Yamazaki *et al.*, 2012), suggestive of an altered
530 replication timing programme. This could also explain the changes in gene expression
531 observed upon siRIF1 in SCC13 cells (Fig. 3A).
532
533 ***RIF1 protects against endogenous and exogenous replication stress in squamous cell***
534 ***carcinoma cells.***
535 Since a key function of RIF1 is the protection of stalled replication forks and the promotion of
536 replication restart (Alver *et al.*, 2017; Buonomo *et al.*, 2009; Garzon *et al.*, 2019; Lebdy *et al.*,
537 2023; Mukherjee *et al.*, 2019), increased expression of RIF1 in SCC cells could therefore
538 indicate a role for RIF1 in enabling cells to deal with high levels of endogenous replication
539 stress. Indeed, there was a strong correlation between the expression of *RIF1* and a
540 replication stress signature (Takahashi *et al.*, 2022) in HNSCC cell lines (Supplementary Fig.
541 5A, E). Knockdown of RIF1 in SCC13 cells increased their endogenous replication stress, as
542 evident from increased levels of pS4/8-RPA32 (indicating accumulation of single stranded

543 DNA at replication forks and recruitment and activation of the replication stress kinases
544 ATR/ATM/DNA-PK) as well as increased levels of γH2Ax (indicating accumulation of DNA
545 DSBs) (Fig. 7A). In contrast to the strong activation of the replication stress checkpoint
546 (phosphorylation of CHK1 on Ser317; (Ashley *et al.*, 2014; Liu *et al.*, 2012)) observed upon HU
547 treatment, the elevated endogenous replication stress in shRIF1 SCC13 cells did not translate
548 into robust CHK1 activation (Fig. 7A). Consequently, asynchronously proliferating shRIF1 cells
549 displayed no dramatic alterations to their cell cycle profiles (Fig. 7B). However, the
550 accumulation of DNA damage in cultures of shRIF1 SCC13 cells became more accentuated
551 after a few passages, when cells had undergone multiple rounds of cell division (Fig. 7C),
552 resulting in reduced clonal colony growth (Fig. 7D). Together, our results are thus consistent
553 with a scenario where SCC cells depend on elevated RIF1 expression to deal with high levels
554 of endogenous replication stress that are, at least in part, controlled by YAP-driven oncogenic
555 mechanisms.

556 Since we found that depletion of YAP reduced RIF1 protein levels (Fig. 3), we hypothesised
557 that shYAP SCC13 cells should therefore be more sensitive to exogenous replication stress
558 induced by treatment with HU (Fig. 7A). Indeed, we observed a synergistic effect of YAP
559 depletion and low doses of HU on SCC13 clonal colony growth (Fig. 7E, F).

560

561 **Discussion**

562 Our findings provide a novel insight into the oncogenic mechanisms of hyperactive YAP/TAZ
563 in SCC. While YAP/TAZ promote proliferation by regulating transcriptional programmes that
564 drive cell cycle progression, they also suppress commitment to terminal differentiation. Thus,
565 the functions of YAP/TAZ appear to be highly conserved within the epidermal lineage, as both
566 normal epidermal stem cells (De Rosa *et al.*, 2019; Walko *et al.*, 2017; Yuan *et al.*, 2020) and

567 neoplastic keratinocytes in BCC (Yuan *et al.*, 2021) and cSCC (this study) show strong
568 dependency on YAP/TAZ signalling for cell proliferation. This suggests that cancers originating
569 from epidermal stem/progenitor cells 'hijack' the tissue regeneration-promoting functions of
570 YAP/TAZ to fuel their high rates of proliferation while remaining in an undifferentiated cell
571 state. The increased expression of genes that are positively regulated by YAP/TAZ in both non-
572 lesional and tumour tissue of human cSCCs that underwent metastatic progression
573 (Supplementary Fig. 7) provides strong support for this idea. Our RIME experiments revealed
574 that the transcriptional co-regulator functions of YAP/TAZ are likely mediated by the BAF-type
575 SWI/SNF and the NuRD chromatin remodelling complexes. Indeed, in HNSCC cells, BAF-type
576 SWI/SNF and YAP-TEAD complexes were shown to be co-dependent for chromatin binding,
577 whereby they create a positive-feedback mechanism to maintain open chromatin for
578 transcription (Chang *et al.*, 2021). In contrast, recruitment of the NuRD complex (Kim *et al.*,
579 2015) could be involved in the observed co-repressor functions of YAP/TAZ.

580 We found that the cyclin-dependent kinase inhibitor p21/CDKN1A became strongly
581 upregulated in response to YAP depletion, suggesting that suppression of p21 is a key function
582 of YAP in squamous cancers. Of note, p21 was shown to act as an important brake to SCC
583 development (Cardinali *et al*, 1998; Topley *et al.*, 1999). Previous studies have also noted that
584 keratinocytes express a pool of p21 that is regulated in a TP53-independent fashion (de Pedro
585 *et al.*, 2021; Freije *et al.*, 2014). YAP/TAZ thus appear to serve as an extra control layer for p21
586 expression in keratinocytes. In future work, it will be important to establish if *CDKN1A* is direct
587 transcriptional target of YAP-TEAD. A previous study which employed a transgenic mouse
588 model where cSCC development was driven by expression of oncogenic *Kras*^{G12D} and knock-
589 out of *Tp53* in epidermal stem cells (Debaugnies *et al.*, 2018), that simultaneous activation of
590 Kras^{G12D} and YAP/TAZ knock-down induces apoptosis. In our human cSCC cell line-focused

591 study we found that YAP/TAZ depletion has cytostatic- and differentiation-promoting, rather
592 than cytotoxic effects. It is worth noting that activating mutations in the *RAS* proto-oncogenes
593 are not very frequent in human cSCC (Winge *et al.*, 2023), with some tumours (~10%) actually
594 showing copy number loss of *HRAS* (Inman *et al*, 2018). Induction of apoptosis in response to
595 YAP/TAZ depletion might thus be specific only to cSCCs expressing oncogenic RAS (Debaugnies
596 *et al.*, 2018).

597 A major finding of this study was the identification of a complex functional relationship
598 between YAP and RIF1, whereby YAP modulates *RIF1* gene expression via TEAD TFs, but also
599 forms a complex with RIF1 on the chromatin. We found that the key functions of RIF1
600 (regulation of DNA replication dynamics (Alver *et al.*, 2017; Cornacchia *et al.*, 2012; Klein *et*
601 *al.*, 2021; Yamazaki *et al.*, 2012) and protection of replication forks under replication stress
602 (Buonomo *et al.*, 2009; Garzon *et al.*, 2019; Lebdy *et al.*, 2023; Mukherjee *et al.*, 2019)) are
603 conserved in squamous cancers. RIF1 enables SCC cells to deal with their high levels of
604 endogenous replication stress, since RIF1 depletion leads to accumulation of DNA damage,
605 which ultimately reduces clonal colony growth. Increased formation of the YAP-RIF1 complex
606 in response to HU treatment suggested a specific role of YAP in enabling RIF1's functions at
607 stalled and deactivated replication forks (Garzon *et al.*, 2019; Mukherjee *et al.*, 2019). Indeed,
608 we found that YAP depletion and the concomitant reduction in RIF1 expression sensitised cSCC
609 cells to HU treatment. Of note, HU is sometimes used in chemoradiotherapy for HNSCC
610 patients (Li *et al*, 2023). RIF1 protein is subject to proteolytic degradation (Wang *et al*, 2009;
611 Yoshizawa-Sugata *et al.*, 2021). We thus speculate that the interaction with YAP on the
612 chromatin stabilizes RIF1 and enables its proper functions for DDR. This scenario is supported
613 by our observation that the combination of YAP knockdown and inhibition of protein synthesis
614 caused a much stronger depletion of RIF1 protein than shYAP alone. Our findings thus provide

615 evidence for a non-canonical role of YAP in SCC, whereby it engages RIF1 to dampen the high
616 levels of endogenous replication stress in these cancers, which are—at least in part—caused
617 by YAP's oncogenic functions itself. Since normal human epidermal keratinocytes respond to
618 expression of constitutively nuclear YAP with oncogene-induced senescence (De Rosa *et al.*,
619 2019), upregulation and stabilization of RIF1 expression in cSCC cells through YAP-TEAD serves
620 as an elegant mechanism whereby cancer cells with hyperactivated YAP are able to escape
621 senescence.
622

623 **Materials and Methods**

624 ***Human tissues***

625 All human tissue work was performed in the lab of Dr Beate Lichtenberger at the Medical
626 University of Vienna, Austria. Written informed patient consent was obtained before tissue
627 collection in accordance with the Declaration of Helsinki. The study was approved by the
628 Institutional Review Board under the ethical permits EK#1695/2021 and EK#1783/2020.
629

630 ***Cell culture***

631 All cell lines were routinely (quarterly test intervals) confirmed to be free of mycoplasma
632 infection using PCR LookOut® Mycoplasma PCR Detection Kit (Merck, UK).

633 Mouse 3T3 embryonic fibroblasts (subclone J2), originally established from random-bred
634 Swiss mice (Todaro *et al*, 1965), were used to provide optimal clonal growth support to normal
635 and neoplastic human epidermal keratinocytes grown in co-culture (Rheinwald & Green,
636 1975). Stocks were kindly provided by Prof Fiona Watt (Centre for Gene Therapy and
637 Regenerative Medicine, King's College London, UK; EMBL, Heidelberg, Germany; not
638 authenticated), or were purchased from Kerafast (Catalogue #EF3003). 3T3-J2 fibroblasts

639 were routinely cultured in high-glucose DMEM (Merck) supplemented with 10% (v/v) bovine
640 serum (Fisher Scientific), 100 IU/mL penicillin and 100 µg/mL streptomycin (Merck), and 2 mM
641 L-glutamine (Merck) (complete fibroblast medium) at 37°C, 5% CO2. Fibroblast cultures were
642 not allowed to grow to confluence and were not grown beyond passage 12 to prevent
643 senescence or spontaneous transformation. To prepare feeder cell layers, 3T3-J2 fibroblasts
644 were treated for 3 hours with 4 µg/mL mitomycin C (Merck) at 37°C, 5% CO2, to irreversibly
645 stall the cell cycle (Rheinwald, 1980).

646 Stock cultures of primary normal human keratinocytes (NHKs, strain km) were obtained from
647 surgically discarded foreskin (Walko *et al.*, 2017). SCC13 cells are a cell line established from a
648 recurring cutaneous SCC (cSCC) of facial epidermis and were obtained from Dr James
649 Rheinwald (Department of Dermatology, Harvard Skin Research Centre, USA), not
650 authenticated (Rheinwald & Beckett, 1981). To study the progression of human cSCC, we used
651 four isogenic human cell lines that were isolated from skin biopsies from a immune-
652 suppressed patient at progressive disease stages: PM1 cells were derived from a pre-
653 malignant dysplastic lesion on the patient's head, MET1 was derived from a primary invasive
654 cSCC growing on the patient's right hand, MET2 was established from a rapid local recurrence
655 after surgical removal of the primary tumour, and MET4 was established from an axillary
656 lymph node metastasis that developed from the primary cSCC (Proby *et al.*, 2000). The
657 progression series cell lines were purchased from Ximbio (PM1 #153571, MET1 #153539,
658 MET2 #153569, MET4 #153570), and were last re-authenticated in Autumn of 2023. SCC-NR
659 cells were isolated by Dr Nicholas Rabey at Addenbrooke's Hospital (Cambridge, UK) from a
660 portion of a surgically excised cutaneous SCC from the back of the hand of an elderly male
661 patient and were used in all experiments at passages 3 or 4 (Walko *et al.*, 2017). All other cell
662 lines were used at passages 2–8. NHKs and cSCC cells were grown in FAD medium (1 part high

663 glucose DMEM GlutaMAX™ supplemented with pyruvate (Fisher Scientific) plus 3 parts Ham's
664 F12 GlutaMAX™ (Fisher Scientific), supplemented with $1.8x10^{-4}$ M adenine (Merck), 10% (v/v)
665 foetal bovine serum (Fisher Scientific, batch-tested for optimal clonal growth support), 5
666 µg/ml insulin (Merck), 0.5 µg/ml hydrocortisone (Merck), 10 ng/mL epidermal growth factor
667 (Peprotech), 8.5 ng/mL cholera toxin (Merck), 2 nM T3 supplement (3,3',5-triiodo-l-thyronine
668 sodium salt) (Merck), and 100 IU/mL penicillin and 100 µg/mL streptomycin (Merck) on a
669 feeder layer of mitotically inactivated 3T3-J2 cells, and grown at 37°C at 5% CO_2, as previously
670 described (Walko *et al.*, 2017).

671 HARA lung SCC cells (Ichinose *et al*, 1993) were purchased from the National Institutes of
672 Biomedical Innovation, Health, and Nutrition (NIBIOHN) JCRB Cell Bank, Japan (catalogue
673 #JCRB1080.0), and were re-authenticated in August 2024. HARA cells were cultured in
674 complete RPMI medium (10% (v/v) fetal bovine serum, 100 IU/mL penicillin and 100 µg/mL
675 streptomycin (Merck), and 2 mM L-glutamine (Merck).

676

677 ***Generation of stable shRNA-expressing cell lines***

678 SCC13 cells, cultured on feeder cells to ~70% confluence, were disaggregated in trypsin/EDTA
679 and cells (2.5×10^5) were seeded into 6-well cell culture plates (Corning™ Costar™, UK) and
680 cultured for 24 h in FAD medium. Medium was then changed to Opti-MEM (Fisher Scientific).
681 To generate stable SCC13 cell lines expressing RIF1-targeting shRNAs, SCC13 cells were
682 infected with MISSION® lentiviral particles (Merck, the sequences of the shRNAs can be found
683 in (Supplementary Table 1A) at a multiplicity of infection (MOI) of 2–3 in the presence of
684 5 µg/ml polybrene (Hexadimethrine bromide, Merck). For creating stable SCC13 cell lines
685 expressing YAP- or TAZ-targeting shRNAs, the SMARTvector™ inducible lentiviral platform was

686 used, which implements a microRNA-scaffolded Tet-On 3G bipartite induction system
687 (Horizon Discovery-Dharmacon™, the sequences of the shRNAs can be found in
688 Supplementary Table 1B). The lentiviral vector included a puromycin resistance element
689 (PuroR) for selection post-infection, as well as a 2A self-cleaving peptide which allowed for
690 PuroR and Tet-On 3G expression from a single mCMV promoter that was selected for
691 negligible basal expression and strong activation when induced (data not shown). A
692 doxycycline-inducible TRE3G promoter was driving expression of the shRNA as well as a
693 fluorescent turbo-RFP reporter. After 24 h incubation with viral particles, medium was
694 changed to FAD medium, and shRNA-expressing cells were selected for 7 days using
695 puromycin (2.5 µg/ml, Merck) in co-culture with puromycin-resistant 3T3-J2 fibroblasts
696 (kindly provided by Prof Fiona Watt, Centre for Gene Therapy and Regenerative Medicine,
697 King's College London, UK; EMBL, Heidelberg, Germany). For experiments using the stable
698 SCC13 cell lines with doxycycline inducible shRNAs, cells were incubated with FAD medium
699 supplemented with 5 µg/mL doxycycline (Tocris) for 48 hours before trypsinisation and
700 seeding for downstream experiments.
701
702 ***siRNA transfection***

703 24 hours after seeding, cells were transfected with 10-20 nM of ON-TARGET plus SMARTpool
704 siRNAs (Horizon Discovery, Supplementary Table 1C) using INTERFERin® transfection reagent
705 (Polyplus, VWR) in Opti-MEM (|Fisher Scientific) for 5 hours, then washed with PBS and grown
706 in FAD medium for up to 72 hours.
707
708 ***Colony formation assay***

709 1x10^3 cells per well were seeded in triplicate technical replicates into 6-well cell culture
710 plates (Corning™ Costar™, UK) without feeder cells and were cultured for 10-14 days with
711 frequent (every 2–3 days) media changes, then fixed in 4% PFA for 30 minutes at room
712 temperature. In case of treatment with hydroxyurea, different drug concentrations were
713 added 24 hours after seeding and fresh drug was added with each medium change. Colonies
714 were stained using crystal violet solution (2% (w/v) crystal violet (Merck, UK) dissolved in 20%
715 (v/v) methanol) for one hour at room temperature and then washed extensively in deionised
716 water and air-dried. Colonies were either imaged using a transilluminator and cell phone
717 camera or were scanned using a flat-bed scanner. Quantification of culture area covered by
718 colonies were performed using ImageJ.
719
720 ***Cell synchronisation by double thymidine block***
721 Cells were seeded in FAD medium and treated with 2.5 mM thymidine (Merck, UK) for 24
722 hours at 37°C, 5% CO_2. Cells were then washed with FAD medium (without thymidine), fresh
723 FAD medium (without thymidine) was added, and cells were incubated for 15 hours before
724 the medium was supplemented again with 2.5 mM thymidine for a further 24 hours. Following
725 thymidine washout, cells were grown in FAD medium.
726
727 ***Cell cycle analysis by flow cytometry***
728 Prior to trypsinization, Click-iT™ EdU (Fisher Scientific, UK) was added to the cell culture
729 medium to a final concentration of 10 µM, and cells were incubated for 30 minutes at 37°C.
730 Trypsinized cells were then centrifuged at 500 x g for 3 minutes (RT), the supernatant was
731 removed, and the pellet resuspended in 3 mL PBS, followed by another centrifugation at 500
732 x g (RT) for 5 minutes. Pelleted cells were next resuspended in 100 µl 0.9% (w/v) NaCl and

733 added dropwise to 1.8 ml ice cold 70% (v/v) ethanol for fixation and stored at -20°C for a
734 minimum of 2 hours before being centrifuged again for 5 minutes at 400 x g (4°C). The cell
735 pellet was then resuspended in 0.5 ml PBS and transferred to a clean tube, and cells were
736 centrifuged for 5 minutes at 400 x g (4°C). This cell pellet was then resuspended in 100 µl Click-
737 iT™ cell reaction buffer (Fisher Scientific, UK) and incubated at RT in the dark for 30 minutes.
738 EdU-labelled cells were then centrifuged for 5 minutes at 400 x g (4°C), cell pellets were
739 resuspended in 500 µl 1% (w/v) BSA in PBS and centrifuged for 5 minutes at 400 x g (4°C), then
740 resuspended in 500 µl PBS. RNase (Merck) was added to a final concentration of 0.5 µg/ml
741 and the sample was incubated on a heat block at 37°C for 15 minutes. Propidium iodide
742 (Merck) was added to a final concentration of 20 µg/ml and the sample was incubated on ice
743 for 20 minutes in the dark before a minimum of 20,000 cells were analysed on a FACS Canto™
744 cell sorter (BBD Biosciences). Data were analysed using FCS Express™, De Novo Software
745 (version 7.14.0020).
746
747 ***Rapid immunoprecipitation mass spectrometry of endogenous proteins (RIME)***
748 NHK and SCC13 cells were seeded at clonal density (500,000 cells) into 15 cm dishes
749 containing a mitotically inhibited 3T3-J2 fibroblast feeder layer and cultured for 4 days. This
750 enabled the formation of small colonies with predominantly nuclear YAP/TAZ expression
751 (Supplementary Fig. 1B). Two independent cultures (=independent experiments, starting from
752 separate cell stocks) were grown for each cell type. Following removal of the feeder layer on
753 day 4 of culture, cells were grown in complete FAD medium (that had been conditioned by
754 mitotically inhibited 3T3-J2 fibroblast cells) for a further 24 hours. Cells were fixed with 1%
755 (v/v) methanol-free formaldehyde for 8 min at RT and the fixation reaction was subsequently
756 rapidly quenched with 0.125 M glycine for 5 min. Fixed cells were gently scraped into ice-cold

757 washing buffer (0.5% (v/v) IGEPAL CA-630, 100 µm PMSF, in PBS, pH 7.4) and were washed
758 three times by centrifugation (800 x g, 10 minutes, 4°C) and resuspension. The final cell pellets
759 (containing between 2 x 10^7 and 7 x 10^7 cells) were stored at -80°C and shipped to Active Motif
760 (USA) on dry ice.

761 RIME was performed by Active Motif (USA). Chromatin was isolated from formaldehyde-fixed
762 cell pellets by the addition of lysis buffer (custom, proprietary to Active Motif), followed by
763 cell disruption with a Dounce homogenizer (15 ml volume with tight-fitting pestle) to release
764 nuclei. Nuclei were sonicated on ice in ChIP buffer (custom, proprietary to Active Motif) using
765 an EpiShear Probe Sonicator (68% pulsed sonication: 30sec on/30sec off, 10 minutes total
766 sonication time) to lyse the cells and shear the DNA to an average fragment length of 300-500
767 bp. Genomic DNA for chromatin quantification was prepared by treating aliquots of chromatin
768 with RNase (Merck), proteinase K (Merck) and heat treatment (65°C overnight) for de-
769 crosslinking, followed by ethanol precipitation. Pellets were resuspended in 1/5 volume Tris-
770 EDTA buffer, and the DNA concentration was quantified on a NanoDrop 2000 (Fisher Scientific,
771 USA) spectrophotometer. An aliquot of sheared chromatin (150 µg) was precleared with
772 protein G agarose beads (Invitrogen). For each chromatin preparation, YAP RIME was
773 performed in technical replicates. Control RIME was performed using isotype-matched IgG,
774 and for each independent experiment, the two replicate IgG control immunoprecipitations
775 were pooled for mass spectrometry analysis. YAP chromatin immunoprecipitation was
776 performed using 15 µg of purified rabbit polyclonal YAP-specific antibody (US Biologicals,
777 Y1200-01D) or isotype-matched rabbit IgG (control) and protein G magnetic beads (Active
778 Motif). Immunoprecipitated chromatin-protein complexes were washed extensively with RIPA
779 buffer (1x, Active Motif) and then with 100 mM ammonium bicarbonate (Merck, USA). On-
780 bead proteolytic digestion was performed using trypsin (Worthington Biochemical, USA; 10

781 ng/µl). Protein digests were separated from the beads using a magnetic rack, and digested
782 peptide mixtures were desalted by solid-phase separation using a C18 spin column (Harvard
783 Apparatus, USA). The eluted peptides were vacuum dried using a speedvac.

784 Digested peptides were reconstituted in 5% (v/v) acetonitrile and 0.1% (v/v) trifluoroacetic
785 acid and analysed by LC-MS/MS on a Thermo Scientific Q Exactive Orbitrap Mass spectrometer
786 linked to Dionex Ultimate 3000 HPLC (Thermo Scientific, USA) and a nanospray Flex^{TM} ion
787 source. The digested and desalted peptides were loaded directly onto the separation column
788 (Waters BEH C18, 75 µm x 100 mm, 130Å 1.7u particle size). Peptides were eluted using a 120-
789 minute gradient with a flow rate of 323 nl/min. The gradient was formed using
790 increasing/decreasing concentrations of buffer B (0.1% formic acid in acetonitrile); (1)
791 increase to 5% (v/v) B over 12 min, (1) gradual increase to 25% (v/v) B until the 90 min mark,
792 (3) gradual increase to 95% (v/v) B for 5 min, (4) 95% (v/v) B for another 4 min, (5) gradual
793 decrease to 5% (v/v) B over 20 min. An MS survey scan was obtained for the m/z range 340-
794 1600; MS/MS spectra were acquired using a top 15 method, where the top 15 ions in the MS
795 spectra were subjected to HCD (High Energy Collisional Dissociation). An isolation mass
796 window of 1.6 m/z was set for precursor ion selection, and normalized collision energy of 27%
797 was used for fragmentation. A 20-second duration was used for the dynamic exclusion.

798 Tandem mass spectra were extracted and analysed by PEAKS Studio (version X+,
799 Bioinformatics Solutions Inc., Canada). Charge state deconvolution and de-isotoping were not
800 performed. Reference databases consisted of the UniProtKB/Swiss-Prot database (version
801 180508; 71,771 curated entries) and the cRAP database of common laboratory contaminants
802 (www.thegpm.org/crap; 114 entries). Databases were searched with a mass tolerance of 0.02
803 Da for fragment ions in MS/MS mode, and a parent ion tolerance of 10 PPM in MS mode. Post-

804 translational protein modifications allowed were methionine oxidation, asparagine and
805 glutamine deamidation, which were searched as variable modifications.

806 PEAKS Studio software built-in decoy sequencing and FDR determination was used to validate
807 MS/MS-based peptides. PEAKS Studio uses the "Decoy Fused Method" when calculating FDR
808 where the default cut-off is set to -10logP > 20 to ensure high-quality peptide spectrum
809 matches and to increase confidence in the proteins list obtained. Protein identifications were
810 accepted if they could pass the -10logP of > 20 and contained at least 1 identified unique
811 peptide. FDR for peptide spectrum matches was set at <1%. Proteins that contained similar
812 peptides and could not be differentiated based on MS/MS analysis alone were grouped to
813 satisfy the principles of parsimony. Proteins sharing significant peptide evidence were
814 grouped into protein groups.

815

816 ***Semiquantitative analysis of RIME proteomics data by spectral counting***

817 The following filtering criteria were applied to the protein data obtained in PEAKS studio for
818 each cell type (Supplementary Dataset 1). (1) Identified proteins with <2 unique peptides were
819 removed. (2) We then filtered out proteins with a spectral count average >2 in the IgG
820 immunoprecipitation controls for experiments 1 and 2 combined, and proteins with a spectral
821 count average of <4 in any of the two YAP RIME experiments. (3) Proteins matched to
822 commonly identified IgG contaminant proteins (data downloaded from the contaminant
823 repository for affinity purification (CRAPome, Crapome.org, accessed November 2019)) and
824 to mitochondrial proteins were excluded from further analysis. (4) Proteins displaying a fold
825 change <4 of mean spectral counts in YAP immunoprecipitations vs spectral counts in the
826 respective IgG control immunoprecipitation in any of the two independent experiments were
827 removed to eliminate low confidence hits that were not considerably more represented in the

828 YAP immunoprecipitation than the IgG immunoprecipitation. High confidence YAP-interacting
829 proteins were further screened for potential physiological significance by filtering against lists
830 of candidate genes positively and negatively regulating clonal growth of NHK and SCC-13 cells
831 (Walko et al., 2017). Interaction networks were created using Cytoscape version 3.9.1 and
832 using the Cytoscape STRING app version 1.7.1 and manually curated into functional groups
833 using input from Gene Ontology Enrichment Analysis performed using gprofiler
834 (https://biit.cs.ut.ee/gprofiler/gost) functional profiling tool with electronic GO annotations
835 unselected (Reimand et al., 2019) and visualised using EnrichmentMap (Cytoscape app
836 version: 3.3.4) in Cytoscape (version:3.9.1).
837
838 ***Immunofluorescence microscopy***
839 Cells were seeded onto acid-washed and UV-sterilized glass coverslips coated with rat tail
840 collagen I (10 µg/ml; Fisher Scientific, UK) and fixed using 4% (v/v) paraformaldehyde (PFA)
841 for 30 minutes at RT. Immunostaining was performed in a PBS-humidified chamber. Cells were
842 permeabilised with 0.1% (v/v) Triton-X100 (Merck, UK) for 25 minutes then blocked in 10%
843 (v/v) BSA (Merck, UK) + 0.1% (v/v) Triton-X100. Primary antibodies (Supplementary Table 2)
844 were diluted in antibody diluent buffer (2% (v/v) BSA + 0.1% (v/v) Triton-X100) and incubated
845 overnight at 4°C. Coverslips were washed thoroughly with PBS, secondary antibodies
846 (Supplementary Table 2), diluted in antibody diluent, were added, and the samples incubated
847 for 1 hour at RT in the dark, then washed multiple times with PBS and once with MilliQ water.
848 Coverslips were mounted onto glass microscope slides using ProLong Gold™ anti-fade
849 mounting medium with DAPI (Fisher Scientific, UK,) or alternatively, incubated with 2 µg/ml
850 Hoechst 33342 (Fisher Scientific, UK) in PBS for 5 minutes, washed once with PBS, and
851 mounted with ProLong Gold™ anti-fade glass mounting medium without DAPI (Fisher

852 Scientific, UK). For confocal microscopy, images were acquired using a ZEISS LSM 880 laser
853 scanning confocal microscope using 40x/1.3 Oil DIC UV-IR M27 or 63x/1.4 Oil DIC UV-IR M27
854 objectives at 16 Bit depth, 0.5 µm optical Sections for Z-stacks, and 2048x2048 pixel
855 resolution. Images were processed using ImageJ (https://imagej.nih.gov/ij/) or ZEN blue
856 (Zeiss) with maximal orthogonal projection of Z-stacks. Quantification was performed using
857 CellProfiler (version 4.0.7). Immunofluorescence images in Supplementary Figure 1B were
858 obtained on a ZOE® Fluorescent Cell Imager (Bio Rad) using standard setup (20x objective)
859 and digital zoom. Minimal processing (changes in brightness and contrast) was applied equally
860 across entire images and applied equally to controls.
861
862 ***Quantification of RIF1 expression in human tissues***
863 Immunofluorescence staining was performed on 4 µm human FFPE sections according to
864 standard protocols. Antigen retrieval was conducted in Dako Target Retrieval Solution, pH 9.0
865 (Agilent Technologies, Santa Clara, California, USA), and 3% (w/v) BSA in PBS containing 0.05%
866 (v/v) Tween 20 (PBS-T) was used for blocking. Primary antibodies against Keratin 14 (chicken
867 pAb (Poly9060), BioLegend Cat# 906004, RRID:AB_2616962; 1:250) and RIF1 (rabbit mAb
868 (D2F2M), Cell Signalling Technology Cat# 95558, RRID:AB_2800249; 1:50) were diluted in 1%
869 (w/v) BSA in PBS-T and incubated overnight. Fluorescently labelled donkey anti-chicken (IgY
870 (H+L) highly cross adsorbed, Alexa Fluor™ 594, Fisher Scientific, catalogue # A78951, RRID
871 AB_2921073; 1:500,) and donkey anti-rabbit (IgG (H+L) highly cross-adsorbed secondary
872 antibody, Alexa Fluor™ 488, Fisher Scientific, catalogue # A-21206, RRID AB_2535792; 1:500,)
873 secondary antibodies were incubated for 90 minutes at ambient temperature. DAPI was used
874 for nuclear counter-staining. Images were captured using the Vectra Polaris™ imaging system,
875 and image analysis was conducted with the HALO® image analysis platform v3.6.4134. The

876 HighPlex FL v4.2.14 plugin was employed for image analysis, with signal intensity thresholds
877 set for the Opal620 (AF594) channel to differentiate positive from negative cells. The
878 DenseNet V2 (Halo AI) classifier was trained and applied to differentiate between tumour and
879 stroma regions. Depending on the size of the tissue, between 2-13 regions of interest with an
880 area of 1 mm^2, representing the tumour were analyzed. Data analysis was performed using
881 GraphPad Prism version 8.0.0 for Windows (GraphPad Software, San Diego, California USA,
882 www.graphpad.com).

883 Additional images of human squamous cell carcinoma samples were obtained by datamining
884 the www.proteinatlas.org database (Ponten *et al*, 2008; Uhlen *et al*, 2015).

885

886 ***In-situ proximity ligation assay***

887 Cells were fixed and permeabilised as described above. Coverslips were blocked in Proximity
888 Ligation Assay (PLA) (Duolink®, Sigma) blocking buffer, and primary antibodies
889 (Supplementary Table 2), diluted in Duolink® antibody diluent, were added overnight.
890 Proximity ligation assay reactions were performed as per the manufacturer's instructions.
891 Coverslips were mounted onto glass slides using Duolink® PLA mounting medium with DAPI
892 and sealed with clear nail polish. Images were acquired on a Zeiss LSM-880 confocal
893 microscope using a 40x/1.3 Oil DIC UV-IR M27 objective. All images belonging to the same
894 experimental repeat were acquired in one imaging session at 16-Bit depth using a Z-stack (0.5
895 µm slice interval) and a 2048x2048 pixels dimension. Images were analysed on ZEN blue
896 version 3.3.89.0000 and processed using a maximal frontal orthogonal projection including all
897 Z-stack slices. Background fluorescence was removed using the same parameters for each
898 image belonging to the same image set (= experimental repeat). Image quantifications were
899 performed using CellProfiler version 4.0.7. Nuclei were defined as parent objects using the

900 'IdentifyPrimaryObjects' module based on DAPI fluorescence signal and intensity of PLA signal
901 per nucleus was quantified within the defined nuclear area using the 'MeasureIntensity'
902 module. To account for differences in YAP-RIF1 and YAP-TEAD fluorescence signal intensities
903 between different experimental repeats (Figure 1), mean nuclear PLA signal fluorescence
904 intensity in shYAP/TAZ cells was normalized to that in shNTC cells (Melendez Garcia *et al.*,
905 2022). A one sample two-tailed t test was then used to test for statistical significance
906 (Melendez Garcia *et al.*, 2022). Statistical significance between the mean PLA signal intensities
907 in the shNTC and shY/T cell populations (assessed by Mann-Whitney test) was high ($p<0.0001$)
908 for each individual experiment (not shown).
909
910 ***Preparation of protein extracts for immunoblotting***
911 RIPA buffer (1x) (Cell Signalling Technologies) or Cell Lysis buffer (1x; Cell Signalling
912 Technologies, #9803; for co-immunoprecipitation experiments), supplemented with protease
913 inhibitors (cOmplete™ ULTRA, EDTA-free, Merck, UK) and phosphatase inhibitors (PhosStop,
914 Merck, UK), was added to cell culture plates and cells were lysed on ice for 15 minutes. Cell
915 remnants were then scraped into the lysis buffer, the lysate was transferred into a tube and
916 sonicated in an ice bath using an MSE Soniprep 150 plus sonicator at 12 Amp for 15 minutes
917 with shaking. Lysates were centrifuged at 16,000 x g for 10 minutes (4°C). For co-
918 immunoprecipitation experiments, sample sonication was not performed. The supernatant
919 was collected, and BCA assay was performed to measure protein concentration using Pierce
920 BCA Protein Assay Kit (Thermo Fisher, UK).
921
922 ***Preparation of chromatin-associated protein fractions***

923 Chromatin fractions were prepared as described (Alver *et al.*, 2017). Briefly, cytoskeleton
924 buffer (300 mM sucrose, 3 mM $MgCl_2$, 100 mM NaCl, 0.5% (v/v) Triton X-100, 10 mM HEPES
925 (pH 7.4)) supplemented with protease inhibitors (cOmplete™ ULTRA Tablets, EDTA-free,
926 Merck, UK) and phosphatase inhibitors (PhosStop, Merck, UK) was added to cells growing in
927 cell culture dishes, and these were incubated on ice for 5 minutes. Cells were then scraped
928 into the buffer and the extract was transferred to a microcentrifuge tube and incubated on ice
929 for further 10 minutes. Samples were then centrifuged at 500 x g for 5 minutes at 4°C, and the
930 supernatant was removed and discarded. Chromatin pellets were washed twice in
931 cytoskeleton buffer without Triton-X100 and resuspended in 50 µl RIPA buffer (Cell Signalling
932 Technologies, UK) containing protease and phosphatase inhibitors, and incubated on ice for 5
933 minutes. 50 units Benzonase® Nuclease (Merck, UK) and $MgCl_2$ (Sigma, UK, final
934 concentration: 3 mM) were added, and the chromatin fraction was incubated on ice for 20
935 minutes until it had visibly reduced viscosity. The chromatin fraction was then centrifuged at
936 16,000 x g for 10 minutes at 4°C, and the supernatant was recovered for immunoblotting
937 analysis.
938
939 ***Co-immunoprecipitation from nuclei-enriched fractions***
940 Cells were grown to ~70% confluency and were washed twice with ice-cold PBS before
941 incubation on ice for 15 minutes with nuclear extraction buffer (50 mM KCl, 2 mM $MgCl_2$, 1
942 mM EDTA, 1 mM DTT, 0.1% (v/v) IGEPAL CA-630, 10 mM HEPES (pH 7.4)), supplemented with
943 protease inhibitors (cOmplete™ ULTRA, EDTA-free, Merck, UK) and phosphatase inhibitors
944 (PhosStop, Merck, UK)). Cell remnants were then scraped into the buffer, the suspension was
945 collected into pre-cooled microcentrifuge tubes, vortexed for 10 seconds, and centrifuged at
946 750 x g for 5 minutes (4°C) to pellet nuclei. The cytoplasmic fraction was removed and the

947 nuclear pellet was washed once in ice-cold PBS, resuspended in ice-cold nuclear lysis buffer
948 (450 mM NaCl, 0.1 mM EDTA, 3 mM $MgCl_2$, 0.1% Triton X-100, 1% (v/v) IGEPAL CA-630, 1 mM
949 DTT, 20 mM HEPES (pH 7.4)) supplemented with protease inhibitors (cOmplete™ ULTRA, EDTA-
950 free, Merck, UK) and phosphatase inhibitors (PhosStop, Merck, UK), transferred to a clean pre-
951 cooled micro-centrifuge tube, and incubated on ice for 15 minutes. Chromatin was then
952 sheared either by passaging 10 times through a 27G needle attached to a 1 ml syringe or by
953 the addition of Benzonase® Nuclease (Merck, UK). Needle-sheared nuclear fractions were
954 centrifuged at 13,000 x g for 10 minutes (4°C) and the supernatant was diluted (1:3) to a final
955 concentration of 150 mM NaCl using nuclear lysis buffer without NaCl. For Benzonase®-
956 treatment of nuclear fractions, chromatin suspension in nuclear lysis buffer was similarly
957 adjusted to 150 mM NaCl using nuclear lysis buffer. Benzonase® was then added, and the
958 chromatin suspension was incubated on ice for 15 minutes with intermittent vortexing. EDTA
959 was added to a 1 mM final concentration and samples were centrifuged at 13,000 x g for 10
960 minutes (4°C).

961 BCA assay was performed to measure protein concentration, and agarose gel electrophoresis
962 of DNA was used to validate the Benzonase digest. To this end, a 1% (w/v) agarose (Sigma, UK)
963 gel was prepared using 1x Tris-acetate-EDTA buffer (Fisher Scientific, UK) and GelRed® Nucleic
964 Acid Stain (Merck, UK). 10 µl of sample was incubated with 1 µl proteinase K for 1 hour at 65C
965 and then diluted with TriTrack DNA loading dye (Fisher Scientific, UK) and run for 1-2 hours at
966 100V in parallel with GeneRuler1 kb Plus DNA Ladder (Thermo Fisher, UK). Gels were imaged
967 using a Syngene Gel Doc system.

968 Nuclear protein samples (containing 2 mg/ml protein) were incubated with 0.07 ug anti-YAP
969 (D8H1X, Lot 4, Cell Signalling Technology) antibody or 0.07 ug of isotype-matched IgG control

970 antibody (Supplementary Table 2) and DTT (1 mM) in micro-centrifuge tubes overnight at 4°C
971 with constant rotation. Protein G Dynabeads™ (Thermo Fisher, UK) were washed four times in
972 PBS supplemented with 0.05% (v/v) Tween-20 (PBS-T, IP wash buffer) using a DynaMag™
973 magnetic rack (Thermo Fisher, UK), transferred to a new tube and washed once in IP wash
974 buffer. Protein G Dynabeads were then resuspended in 50 µL IP-buffer and added to IP
975 reactions, which were then incubated with the beads for 4 hours at 4°C with constant rotation.
976 To pellet the beads, samples were then placed on the DynaMag™ magnetic rack, the
977 supernatant was removed, bead-bound protein complexes were washed 3 times in PBS-T,
978 transferred to a fresh micro-centrifuge tube, resuspended in 20 µl 50 mM glycine (pH 2.8) and
979 10 µl 3x Laemmli buffer (BioRad, UK) + β-mercaptoethanol (elution buffer), and incubated for
980 10 minutes at 95°C. Beads were removed using the DynaMag™ magnetic rack and the eluted
981 proteins were analysed by SDS-PAGE (alongside 10 ug (1%) of input lysate) and
982 immunoblotting.
983
984 ***Immunoblotting analysis***
985 Protein samples were denatured and reduced in Laemmli buffer (BioRad, UK) containing 10%
986 (v/v) β-mercaptoethanol for 5 minutes at 95°C and loaded onto precast 4-20% or 4-15%
987 polyacrylamide mini-PROTEAN Tris-Glycine eXtended (TGX) gels (BioRad, UK). Proteins were
988 transferred onto either 0.2 µm pore-size Nitrocellulose membranes or methanol-activated
989 0.45 µm pore-size PVDF membranes (BioRad, USA), using either the Trans-Blot Turbo Transfer
990 System (BioRad, UK) or tank (wet) transfer depending on protein molecular mass. Large
991 proteins were transferred by wet transfer in wet transfer buffer (3.05 g/l Tris-base, 14.4 g/l
992 glycine) either overnight at 25V (4°C) or for 60 minutes with extensive cooling in wet transfer
993 buffer containing 20% (v/v) methanol at 300 mA. Membranes were blocked in 5% (w/v) BSA

994 dissolved in Tris-buffered saline (TBS) containing 0.1% (v/v) Tween 20 (TBS-T)(=blocking
995 buffer) for 1 hour at RT and primary antibodies (Supplementary Table 2), diluted in blocking
996 buffer, were incubated with the membranes overnight at 4°C with agitation. Membranes were
997 washed three times for 10 minutes with TBS-T and then incubated with secondary horseradish
998 peroxidase (HRP)-conjugated antibodies. Clarity western ECL substrate reagent (BioRad, UK)
999 was used to image immunoblots using a Fusion Solo chemiluminescence imager (Vilber
1000 Lourmat, UK). Where possible, over-saturated images were avoided and exposures within the
1001 dynamic range were selected. Band intensities were quantified based on pixel volume of the
1002 bands using Fusion software (Vilber Lourmat, UK) or Image software (Bio Rad).
1003
1004 ***RNA preparation and Illumina sequencing***
1005 RNA was extracted from cells using the RNeasy Plus Mini kit (Qiagen, UK) and the QIAshredder
1006 shredding system (Qiagen, UK) as per the manufacturer's instructions. RNA yield and purity
1007 were analysed using the Quant-iT™ Qubit RNA BR Assay Kit (Thermo Fisher, UK) in Qubit™
1008 Assay Tubes (Thermo Fisher, UK) on a Qubit 4 Fluorometer (Thermo Fisher, UK). RNA
1009 sequencing was outsourced to Novogene Ltd. (UK). Messenger RNA was purified from total
1010 RNA by poly-A enrichment method using poly-T oligo-attached magnetic beads. RNA library
1011 preparation was performed using the Novogene in-house kit NGS RNA Library Prep Set
1012 (PT042) for the preparation of a 250~300 bp insert cDNA library (unstranded). The library was
1013 checked with Qubit and real-time PCR for quantification and bioanalyzer for size distribution
1014 detection. Paired end PE150 sequencing was performed on Novaseq6000 short-read
1015 sequencing machine (6Gb raw data per sample) platform. Base calling was performed by
1016 Novogene using RTA (Real Time Analysis) software. All samples had a Phred score >30.
1017

1018 ***RNA sequencing data analysis***

1019 Paired reads were aligned to Ensembl GRCh38.105 2.7.4a (Harrison *et al*, 2024) using bowtie2
1020 (v2.4.4)(Langmead & Salzberg, 2012) default settings, sorted and indexed with Samtools
1021 (v1.2)(Li *et al*, 2009), and unstranded exonic read pairs were counted using FeatureCounts
1022 (v2.0.7)(Liao *et al*, 2014) using a slightly modified Ensembl gtf with 'chr' prefix nomenclature.
1023 DESeq2 (v1.44.0)(Love *et al*, 2014) was used in R (v4.4.2) to assess features with >10 reads
1024 across conditions and differential expression of transcripts with a fold change >1.5 and FDR
1025 <0.05. All other results were given the value 0 and genes with no differential expression were
1026 removed from the final data frame for visualisation purposes only.

1027

1028 ***Pathway analysis***

1029 Gene Set Enrichment Analysis (Subramanian *et al*, 2005) was performed in R, using
1030 clusterProfiler (v4.12.6)(Xu *et al*, 2024) on all genes annotated with Entrez IDs using
1031 AnnotationDbi (v1.66.0) and org.Hs.eg.db.Hs (v3.19.1) packages. GO Biological Processes
1032 (Ashburner *et al*, 2000; Gene Ontology *et al*, 2023), Hallmark (Liberzon *et al*, 2015) and
1033 Reactome (Milacic *et al*, 2024) pathway gene sets were downloaded from the Molecular
1034 Signature Database (https://www.gsea-msigdb.org/gsea/msigdb) using msigdbr (v7.5.1).
1035 Specific sets of genes defining progenitor cell populations, early differentiation and late
1036 (terminal) differentiation have been experimentally validated using organotypic models
1037 (Lopez-Pajares *et al.*, 2015). 'set.seed' in R (v4.4.2) was set to '1234' and Benjamini-Hochberg
1038 correction (adjusted p-value <0.05) was used for multiple comparison corrections.

1039

1040 ***Gene set variation analysis***

1041 A more stringent p-value threshold ($<1\times10^{-8}$) was applied to the SCC13 siYAP/TAZ RNA-
1042 seq dataset to reduce the gene set size to <500, as recommended for robust gene set
1043 variation analysis (GSVA) (Hanzelmann *et al*, 2013). This yielded 486 upregulated and 250
1044 downregulated DEGs in siYAP/TAZ compared to siNTC SCC13 cells. GSVA was performed
1045 using the GSVA function (GSVA R package v1.52.3) with default settings. The input comprised
1046 the selected SCC13 RNA-seq gene sets and an expression matrix from 237 cSCC patients with
1047 known clinical outcome (Wang *et al.*, 2023), covering primary cSCC (metastatic and non-
1048 metastatic), perilesional normal skin and metastasis where available. GSVA enrichment scores
1049 were calculated for each sample, and boxplots were used to visualize differential pathway
1050 activity across tissue types. T-tests were applied to assess significant differences in enrichment
1051 scores between groups.
1052
1053 ***RT-qPCR***
1054 mRNA was converted to cDNA (including the removal of genomic DNA) using the QuantiTect
1055 Reverse Transcription Kit (Qiagen, UK) as per the manufacturers' instructions. For the
1056 Comparative C_T method, qPCR reactions were set up using 50 ng cDNA, 10 µL 2x TaqMan™
1057 Fast Advanced Master Mix (Applied Biosystems™, Fisher Scientific, UK), 1 µL 20x TaqMan™
1058 Gene Expression Assay (FAM) (Fisher Scientific, UK) (Supplementary Table 1D) and nuclease-
1059 free water. Reactions were performed in technical triplicates in MicroAmp® Fast 96-Well
1060 reaction plates (Applied Biosystems™, Fisher Scientific, UK)) and run on a StepOnePlus™ Real-
1061 Time PCR System (Fisher Scientific, UK) for 40 cycles; 20 seconds at 95°C, 1 second at 95°C, 20
1062 seconds at 60°C. Relative gene expression was analysed by the $2^{(-\Delta\Delta C_T)}$ method. GAPDH was
1063 used as housekeeping gene for normalization.
1064

1065 ***Reproducibility of experiments***

1066 RIME was performed on two independent cell cultures for each cell type, starting from freshly
1067 thawed cell stocks. For each fixed cell pellet prepared from the independent cell cultures, YAP
1068 RIME was then performed in technical replicates. Control RIME was performed using isotype-
1069 matched IgG, and for each independent experiment, the two replicate IgG control
1070 immunoprecipitations were pooled for mass spectrometry analysis. For RNA-seq analysis, two
1071 independent cell cultures, starting from freshly thawed cell stocks were separately transfected
1072 with siRNA SMARTpools. For co-immunoprecipitations two to three independent experiments
1073 were performed with similar results. For immunostainings of cells, representative images from
1074 one out of three experiments are shown. Western blots are representative of at least two
1075 independent experiments. Cell cycle analysis was performed on two to four independent
1076 experiments. For clonal growth assays at least three independent experiments were
1077 performed with three technical replicates per condition. RT-qPCR analysis was performed on
1078 three independent experiments with three technical replicates.

1079

1080 ***Statistical analysis and data presentation***

1081 Statistical analyses were performed with GraphPad Prism software (version 10.3) or R (v7.5.1).
1082 No statistical method was used to predetermine sample size. Statistical tests used to
1083 determine p-values are specified in Figure Legends. Sample size is indicated in Figure Legends,
1084 Data sets with sufficient *n* numbers were first analysed for normal distribution. In cases where
1085 the data were not found to be normally distributed, they were subsequently analysed using
1086 appropriate non-parametric tests (specified in Figure Legends), provided that the variance was
1087 comparable between the groups analysed. In some figures, superplots (Lord *et al*, 2020) were
1088 used to communicate both the cell-level variability and the experimental reproducibility. The

investigators analysing the data were not blind to the identity of the samples. Further R (v7.5.1) data manipulation packages included genefilter (v1.86.0), dplyr (v1.1.4), tibble (v3.2.1), reshape2 (v1.4.4), plyr (v1.8.9), gage (v2.54.0), gageData (v2.42.0), and rrvgo (v1.16.0), and data were visualised in R using gplots (v3.2.0), ggplot2 (v3.5.1), viridis (v0.6.5), DOSE (v3.30.5), pheatmap (v1.0.12), RColorBrewer (v1.1-3), eulerr (7.0.2), and ggrepel (v0.9.6) packages.

Funding information

This work was supported by the UK Research & Innovation (UKRI) Biotechnology and Biological Sciences Research Council (BBSRC, grant BB/T012978/1 to Gernot Walko), the Academy of Medical Sciences (grant SBF005\1005 to Gernot Walko), the British Skin Foundation (grants 004/SG/18, 036/S/18 ('Peter Massey Skin Cancer Grant'), and 011_SG_22 to Gernot Walko), the Royal Society (grant RGS\R1\191087 to Gernot Walko), the LEO Foundation (grant LF-AW_EMEA-21-400116 to Beate Lichtenberger), the City of Vienna Fund for Innovative Interdisciplinary Cancer Research (grant 22059 to Beate Lichtenberger), and the Austrian Science Fund (FWF) (grant 36368-B to Beate Lichtenberger). Gernot Walko, Jun Wang, Elodie Sins, Benjamin Flynn, and Emma Bailey also acknowledge funding support from the Barts Charity (UK) Strategic Award to the Barts Centre for Squamous Cancer (Centre grant 'A Centre of Excellence for Squamous Cancer', grant G-002030). Jun Wang and Emma Bailey further acknowledge funding support from the Cancer Research UK City of London Major Centre Award core funding support to the Barts Cancer Institute. Jodie Bojko was recipient of a Raoul & Catherine Hughes Scholarship through the University of Bath 'Alumni and Friends' network.

Acknowledgements

We wish to thank our colleagues from the Barts Centre for Squamous Cancer at Queen Mary University of London for critical feedback on our draft manuscript.

Data availability

The authors declare that all data supporting the findings of this study are available within the paper and its supplementary information files. Raw Illumina sequencing data have been deposited in the Gene Expression Omnibus (GEO) following the MIAME guidelines, under the accession number GSE284725.

Author contributions

Jodie Bojko: Data Curation, Formal Analysis, Investigation, Methodology, Visualization, Writing: Original Draft Preparation; Benjamin Flynn: Data Curation, Formal Analysis, Investigation, Methodology, Software, Validation, Visualization; Bertram Aschenbrenner: Data Curation, Formal Analysis, Investigation, Methodology, Software, Visualization; Alexander Howard: Formal Analysis, Investigation, Methodology; Emily Lay: Formal Analysis, Investigation, Methodology; Emma Bailey: Formal Analysis, Investigation, Methodology, Software, Visualization; Natalia Krajic**:** Investigation, Methodology; Sandra Catalan: Investigation, Methodology; Kelli Gallacher: Investigation, Methodology; Elodie Sins: Investigation, Methodology; Jun Wang: Funding acquisition, Methodology, Resources, Supervision; Ute Jungwirth: Formal Analysis, Validation, Visualization, Writing: Original Draft Preparation, Writing: Review &Editing; Beate Lichtenberger: Funding acquisition, Resources, Supervision, Validation, Writing: Original Draft Preparation; Gernot Walko: Conceptualization, Data Curation, Formal Analysis, Funding acquisition, Methodology, Project Administration,

Resources, Supervision, Validation, Visualization, Writing: Original Draft Preparation, Writing: Review &Editing.

Conflict of interest statement

The authors declare that they have no conflict of interest.

References

Al-Hazmi N, Alhazzazi T, Williams G, Stoeber K, Al-Dabbagh R (2018) DNA replication licensing factor MCM2, geminin, and Ki67 define proliferative state and are linked with survival in oral squamous cell carcinoma. *Eur J Oral Sci* 126: 186-196

Alver RC, Chadha GS, Gillespie PJ, Blow JJ (2017) Reversal of DDK-Mediated MCM Phosphorylation by Rif1-PP1 Regulates Replication Initiation and Replisome Stability Independently of ATR/Chk1. *Cell Rep* 18: 2508-2520

Amirifar P, Kissil J (2023) The role of Motin family proteins in tumorigenesis-an update. *Oncogene* 42: 1265-1271

Ashburner M, Ball CA, Blake JA, Botstein D, Butler H, Cherry JM, Davis AP, Dolinski K, Dwight SS, Eppig JT *et al* (2000) Gene ontology: tool for the unification of biology. The Gene Ontology Consortium. *Nat Genet* 25: 25-29

Ashley AK, Shrivastav M, Nie J, Amerin C, Troksa K, Glanzer JG, Liu S, Opiyo SO, Dimitrova DD, Le P *et al* (2014) DNA-PK phosphorylation of RPA32 Ser4/Ser8 regulates replication stress checkpoint activation, fork restart, homologous recombination and mitotic catastrophe. *DNA Repair (Amst)* 21: 131-139

Atemin A, Ivanova A, Kanev PB, Uzunova S, Nedelcheva-Veleva M, Stoynov S (2024) Dynamics of Replication-Associated Protein Levels through the Cell Cycle. *Int J Mol Sci* 25

Bartkova J, Rezaei N, Liontos M, Karakaidos P, Kletsas D, Issaeva N, Vassiliou LV, Kolettas E, Niforou K, Zoumpourlis VC *et al* (2006) Oncogene-induced senescence is part of the tumorigenesis barrier imposed by DNA damage checkpoints. *Nature* 444: 633-637

Battilana G, Zanconato F, Piccolo S (2021) Mechanisms of YAP/TAZ transcriptional control. *Cell Stress* 5: 167-172

Beltrami S, Kim R, Gordon J (2013) Neurofibromatosis type 2 protein, NF2: an uncoventional cell cycle regulator. *Anticancer Res* 33: 1-11

Blanpain C, Fuchs E (2009) Epidermal homeostasis: a balancing act of stem cells in the skin. *Nat Rev Mol Cell Biol* 10: 207-217

Bowry A, Kelly RDW, Petermann E (2021) Hypertranscription and replication stress in cancer. *Trends Cancer* 7: 863-877

Bradner JE, Hnisz D, Young RA (2017) Transcriptional Addiction in Cancer. *Cell* 168: 629-643

Bui DA, Lee W, White AE, Harper JW, Schackmann RC, Overholtzer M, Selfors LM, Brugge JS (2016) Cytokinesis involves a nontranscriptional function of the Hippo pathway effector YAP. *Sci Signal* 9: ra23

Buonomo SB, Wu Y, Ferguson D, de Lange T (2009) Mammalian Rif1 contributes to replication stress survival and homology-directed repair. *J Cell Biol* 187: 385-398

Burns JE, Baird MC, Clark LJ, Burns PA, Edington K, Chapman C, Mitchell R, Robertson G, Soutar D, Parkinson EK (1993) Gene mutations and increased levels of p53 protein in human squamous cell carcinomas and their cell lines. *Br J Cancer* 67: 1274-1284

1179 Burrell RA, McClelland SE, Endesfelder D, Groth P, Weller MC, Shaikh N, Domingo E, Kanu N, Dewhurst
1180 SM, Gronroos E *et al* (2013) Replication stress links structural and numerical cancer chromosomal
1181 instability. *Nature* 494: 492-496
1182 Cardinali M, Jakus J, Shah S, Ensley JF, Robbins KC, Yeudall WA (1998) p21(WAF1/Cip1) retards the
1183 growth of human squamous cell carcinomas in vivo. *Oral Oncol* 34: 211-218
1184 Chakravarthy A, Reddin I, Henderson S, Dong C, Kirkwood N, Jeyakumar M, Rodriguez DR, Martinez
1185 NG, McDermott J, Su X *et al* (2022) Integrated analysis of cervical squamous cell carcinoma cohorts
1186 from three continents reveals conserved subtypes of prognostic significance. *Nat Commun* 13: 5818
1187 Chandrashekar DS, Karthikeyan SK, Korla PK, Patel H, Shovon AR, Athar M, Netto GJ, Qin ZS, Kumar S,
1188 Manne U *et al* (2022) UALCAN: An update to the integrated cancer data analysis platform. *Neoplasia*
1189 25: 18-27
1190 Chang CY, Shipony Z, Lin SG, Kuo A, Xiong X, Loh KM, Greenleaf WJ, Crabtree GR (2021) Increased
1191 ACTL6A occupancy within mSWI/SNF chromatin remodelers drives human squamous cell carcinoma.
1192 *Mol Cell* 81: 4964-4978 e4968
1193 Chang L, Azzolin L, Di Biagio D, Zanconato F, Battilana G, Lucon Xiccato R, Aragona M, Giulitti S, Panciera
1194 T, Gandin A *et al* (2018) The SWI/SNF complex is a mechanoregulated inhibitor of YAP and TAZ. *Nature*
1195 563: 265-269
1196 Chow SE, Hsu CC, Yang CT, Meir YJ (2023) YAP co-localizes with the mitotic spindle and midbody to
1197 safeguard mitotic division in lung-cancer cells. *FEBS J* 290: 5704-5719
1198 Contreras L, Garcia-Gaipo L, Casar B, Gandarillas A (2024) DNA damage signalling histone H2AX is
1199 required for tumour growth. *Cell Death Discov* 10: 99
1200 Cornacchia D, Dileep V, Quivy JP, Foti R, Tili F, Santarella-Mellwig R, Antony C, Almouzni G, Gilbert DM,
1201 Buonomo SB (2012) Mouse Rif1 is a key regulator of the replication-timing programme in mammalian
1202 cells. *EMBO J* 31: 3678-3690
1203 da Costa A, Chowdhury D, Shapiro GI, D'Andrea AD, Konstantinopoulos PA (2023) Targeting replication
1204 stress in cancer therapy. *Nat Rev Drug Discov* 22: 38-58
1205 de Pedro I, Galan-Vidal J, Freije A, de Diego E, Gandarillas A (2021) p21CIP1 controls the squamous
1206 differentiation response to replication stress. *Oncogene* 40: 152-162
1207 De Rosa L, Secone Seconetti A, De Santis G, Pellacani G, Hirsch T, Rothoeft T, Teig N, Pellegrini G, Bauer
1208 JW, De Luca M (2019) Laminin 332-Dependent YAP Dysregulation Depletes Epidermal Stem Cells in
1209 Junctional Epidermolysis Bullosa. *Cell Rep* 27: 2036-2049 e2036
1210 Debaugnies M, Sanchez-Danes A, Rorive S, Raphael M, Liagre M, Parent MA, Brisebarre A, Salmon I,
1211 Blanpain C (2018) YAP and TAZ are essential for basal and squamous cell carcinoma initiation. *EMBO*
1212 *Rep*
1213 Dempster JM, Pacini C, Pantel S, Behan FM, Green T, Krill-Burger J, Beaver CM, Younger ST, Zhivich V,
1214 Najgebauer H *et al* (2019) Agreement between two large pan-cancer CRISPR-Cas9 gene dependency
1215 data sets. *Nat Commun* 10: 5817
1216 Dey A, Varelas X, Guan KL (2020) Targeting the Hippo pathway in cancer, fibrosis, wound healing and
1217 regenerative medicine. *Nat Rev Drug Discov* 19: 480-494
1218 Dotto GP, Rustgi AK (2016) Squamous Cell Cancers: A Unified Perspective on Biology and Genetics.
1219 *Cancer Cell* 29: 622-637
1220 Dungrawala H, Rose KL, Bhat KP, Mohni KN, Glick GG, Couch FB, Cortez D (2015) The Replication
1221 Checkpoint Prevents Two Types of Fork Collapse without Regulating Replisome Stability. *Mol Cell* 59:
1222 998-1010
1223 Elbediwy A, Vincent-Mistiaen ZI, Spencer-Dene B, Stone RK, Boeing S, Wculek SK, Cordero J, Tan EH,
1224 Ridgway R, Brunton VG *et al* (2016) Integrin signalling regulates YAP and TAZ to control skin
1225 homeostasis. *Development* 143: 1674-1687
1226 Flora P, Ezhkova E (2020) Regulatory mechanisms governing epidermal stem cell function during
1227 development and homeostasis. *Development* 147

1228 Foti R, Gnan S, Cornacchia D, Dileep V, Bulut-Karslioglu A, Diehl S, Buness A, Klein FA, Huber W,
1229 Johnstone E *et al* (2016) Nuclear Architecture Organized by Rif1 Underpins the Replication-Timing
1230 Program. *Mol Cell* 61: 260-273
1231 Franklin JM, Wu Z, Guan KL (2023) Insights into recent findings and clinical application of YAP and TAZ
1232 in cancer. *Nat Rev Cancer* 23: 512-525
1233 Freije A, Ceballos L, Coisy M, Barnes L, Rosa M, De Diego E, Blanchard JM, Gandarillas A (2012) Cyclin
1234 E drives human keratinocyte growth into differentiation. *Oncogene* 31: 5180-5192
1235 Freije A, Molinuevo R, Ceballos L, Cagigas M, Alonso-Lecue P, Rodriguez R, Menendez P, Aberdam D,
1236 De Diego E, Gandarillas A (2014) Inactivation of p53 in Human Keratinocytes Leads to Squamous
1237 Differentiation and Shedding via Replication Stress and Mitotic Slippage. *Cell Rep* 9: 1349-1360
1238 Furukawa KT, Yamashita K, Sakurai N, Ohno S (2017) The Epithelial Circumferential Actin Belt Regulates
1239 YAP/TAZ through Nucleocytoplasmic Shuttling of Merlin. *Cell Rep* 20: 1435-1447
1240 Gaillard H, Garcia-Muse T, Aguilera A (2015) Replication stress and cancer. *Nat Rev Cancer* 15: 276-289
1241 Gandarillas A (2012) The mysterious human epidermal cell cycle, or an oncogene-induced
1242 differentiation checkpoint. *Cell Cycle* 11: 4507-4516
1243 Gandarillas A, Davies D, Blanchard JM (2000) Normal and c-Myc-promoted human keratinocyte
1244 differentiation both occur via a novel cell cycle involving cellular growth and endoreplication.
1245 *Oncogene* 19: 3278-3289
1246 Garzon J, Ursich S, Lopes M, Hiraga SI, Donaldson AD (2019) Human RIF1-Protein Phosphatase 1
1247 Prevents Degradation and Breakage of Nascent DNA on Replication Stalling. *Cell Rep* 27: 2558-2566
1248 e2554
1249 Gene Ontology C, Aleksander SA, Balhoff J, Carbon S, Cherry JM, Drabkin HJ, Ebert D, Feuermann M,
1250 Gaudet P, Harris NL *et al* (2023) The Gene Ontology knowledgebase in 2023. *Genetics* 224
1251 Ghias K, Rehmani SS, Razzak SA, Madhani S, Azim MK, Ahmed R, Khan MJ (2019) Mutational landscape
1252 of head and neck squamous cell carcinomas in a South Asian population. *Genet Mol Biol* 4242: 526-
1253 542
1254 Gnan S, Flyamer IM, Klein KN, Castelli E, Rapp A, Maiser A, Chen N, Weber P, Enervald E, Cardoso MC
1255 *et al* (2021) Nuclear organisation and replication timing are coupled through RIF1-PP1 interaction. *Nat*
1256 *Commun* 12: 2910
1257 Hanahan D, Weinberg RA (2011) Hallmarks of cancer: the next generation. *Cell* 144: 646-674
1258 Hanzelmann S, Castelo R, Guinney J (2013) GSVA: gene set variation analysis for microarray and RNA-
1259 seq data. *BMC Bioinformatics* 14: 7
1260 Harrison PW, Amode MR, Austine-Orimoloye O, Azov AG, Barba M, Barnes I, Becker A, Bennett R, Berry
1261 A, Bhai J *et al* (2024) Ensembl 2024. *Nucleic Acids Res* 52: D891-D899
1262 Hassan S, Purdie KJ, Wang J, Harwood CA, Proby CM, Pourreyron C, Mladkova N, Nagano A, Dhayade
1263 S, Athineos D *et al* (2019) A Unique Panel of Patient-Derived Cutaneous Squamous Cell Carcinoma Cell
1264 Lines Provides a Preclinical Pathway for Therapeutic Testing. *Int J Mol Sci* 20
1265 He L, Pratt H, Gao M, Wei F, Weng Z, Struhl K (2021) YAP and TAZ are transcriptional co-activators of
1266 AP-1 proteins and STAT3 during breast cellular transformation. *Elife* 10
1267 Hillmer RE, Link BA (2019) The Roles of Hippo Signaling Transducers Yap and Taz in Chromatin
1268 Remodeling. *Cells* 8
1269 Hiraga SI, Ly T, Garzon J, Horejsi Z, Ohkubo YN, Endo A, Obuse C, Boulton SJ, Lamond AI, Donaldson AD
1270 (2017) Human RIF1 and protein phosphatase 1 stimulate DNA replication origin licensing but suppress
1271 origin activation. *EMBO Rep* 18: 403-419
1272 Hou S, Zhou S, Qin Z, Yang L, Han X, Yao S, Ji H (2017) Evidence, Mechanism, and Clinical Relevance of
1273 the Transdifferentiation from Lung Adenocarcinoma to Squamous Cell Carcinoma. *Am J Pathol* 187:
1274 954-962
1275 Howard A, Bojko J, Flynn B, Bowen S, Jungwirth U, Walko G (2022) Targeting the Hippo/YAP/TAZ
1276 signalling pathway: Novel opportunities for therapeutic interventions into skin cancers. *Exp Dermatol*
1277 31: 1477-1499

Ichinose Y, Iguchi H, Ohta M, Katakami H (1993) Establishment of lung cancer cell line producing parathyroid hormone-related protein. *Cancer Lett* 74: 119-124

Inman GJ, Wang J, Nagano A, Alexandrov LB, Purdie KJ, Taylor RG, Sherwood V, Thomson J, Hogan S, Spender LC *et al* (2018) The genomic landscape of cutaneous SCC reveals drivers and a novel azathioprine associated mutational signature. *Nat Commun* 9: 3667

Jessen M, Gertzmann D, Liss F, Zenk F, Bahner L, Schoffler V, Schulte C, Maric HM, Ade CP, von Eyss B *et al* (2024) Inhibition of the YAP-MMB interaction and targeting NEK2 as potential therapeutic strategies for YAP-driven cancers. *Oncogene* 43: 578-593

Johnson DE, Burtness B, Leemans CR, Lui VWY, Bauman JE, Grandis JR (2020) Head and neck squamous cell carcinoma. *Nat Rev Dis Primers* 6: 92

Kim M, Kim T, Johnson RL, Lim DS (2015) Transcriptional co-repressor function of the hippo pathway transducers YAP and TAZ. *Cell Rep* 11: 270-282

Klein KN, Zhao PA, Lyu X, Sasaki T, Bartlett DA, Singh AM, Tasan I, Zhang M, Watts LP, Hiraga SI *et al* (2021) Replication timing maintains the global epigenetic state in human cells. *Science* 372: 371-378

Kypriotou M, Huber M, Hohl D (2012) The human epidermal differentiation complex: cornified envelope precursors, S100 proteins and the 'fused genes' family. *Exp Dermatol* 21: 643-649

Langmead B, Salzberg SL (2012) Fast gapped-read alignment with Bowtie 2. *Nat Methods* 9: 357-359

Lau SCM, Pan Y, Velcheti V, Wong KK (2022) Squamous cell lung cancer: Current landscape and future therapeutic options. *Cancer Cell* 40: 1279-1293

Lavado A, Park JY, Pare J, Finkelstein D, Pan H, Xu B, Fan Y, Kumar RP, Neale G, Kwak YD *et al* (2018) The Hippo Pathway Prevents YAP/TAZ-Driven Hypertranscription and Controls Neural Progenitor Number. *Dev Cell* 47: 576-591 e578

Lebdy R, Patouillard J, Larroque M, Urbach S, Abou Merhi R, Larroque C, Ribeyre C (2023) The organizer of chromatin topology RIF1 ensures cellular resilience to DNA replication stress. *Life Sci Alliance* 6

Lee JH, Kim TS, Yang TH, Koo BK, Oh SP, Lee KP, Oh HJ, Lee SH, Kong YY, Kim JM *et al* (2008) A crucial role of WW45 in developing epithelial tissues in the mouse. *EMBO J* 27: 1231-1242

Li H, Handsaker B, Wysoker A, Fennell T, Ruan J, Homer N, Marth G, Abecasis G, Durbin R, Genome Project Data Processing S (2009) The Sequence Alignment/Map format and SAMtools. *Bioinformatics* 25: 2078-2079

Li Q, Tie Y, Alu A, Ma X, Shi H (2023) Targeted therapy for head and neck cancer: signaling pathways and clinical studies. *Signal Transduct Target Ther* 8: 31

Li W, Cooper J, Zhou L, Yang C, Erdjument-Bromage H, Zagzag D, Snuderl M, Ladanyi M, Hanemann CO, Zhou P *et al* (2014) Merlin/NF2 loss-driven tumorigenesis linked to CRL4(DCAF1)-mediated inhibition of the hippo pathway kinases Lats1 and 2 in the nucleus. *Cancer Cell* 26: 48-60

Li Y, Li B, Xu B, Han B, Xia H, Chen QM, Li LJ (2015a) Expression of p53, p21(CIP1/WAF1) and eIF4E in the adjacent tissues of oral squamous cell carcinoma: establishing the molecular boundary and a cancer progression model. *Int J Oral Sci* 7: 161-168

Li YY, Hanna GJ, Laga AC, Haddad RI, Lorch JH, Hammerman PS (2015b) Genomic analysis of metastatic cutaneous squamous cell carcinoma. *Clin Cancer Res* 21: 1447-1456

Liao Y, Smyth GK, Shi W (2014) featureCounts: an efficient general purpose program for assigning sequence reads to genomic features. *Bioinformatics* 30: 923-930

Liberzon A, Birger C, Thorvaldsdottir H, Ghandi M, Mesirov JP, Tamayo P (2015) The Molecular Signatures Database (MSigDB) hallmark gene set collection. *Cell Syst* 1: 417-425

Liu C, Yu P, Ren Z, Yao F, Wang L, Hu G, Li P, Zhao Q (2023) Rif1 Regulates Self-Renewal and Impedes Mesendodermal Differentiation of Mouse Embryonic Stem Cells. *Stem Cell Rev Rep* 19: 1540-1553

Liu S, Opiyo SO, Manthey K, Glanzer JG, Ashley AK, Amerin C, Troksa K, Shrivastav M, Nickoloff JA, Oakley GG (2012) Distinct roles for DNA-PK, ATM and ATR in RPA phosphorylation and checkpoint activation in response to replication stress. *Nucleic Acids Res* 40: 10780-10794

Liu Y, Guo B, Aguilera-Jimenez E, Chu VS, Zhou J, Wu Z, Francis JM, Yang X, Choi PS, Bailey SD *et al* (2020) Chromatin Looping Shapes KLF5-Dependent Transcriptional Programs in Human Epithelial Cancers. *Cancer Res* 80: 5464-5477

Lopez-Pajares V, Qu K, Zhang J, Webster DE, Barajas BC, Siprashvili Z, Zarnegar BJ, Boxer LD, Rios EJ, Tao S *et al* (2015) A LncRNA-MAF:MAFB transcription factor network regulates epidermal differentiation. *Dev Cell* 32: 693-706

Lord SJ, Velle KB, Mullins RD, Fritz-Laylin LK (2020) SuperPlots: Communicating reproducibility and variability in cell biology. *J Cell Biol* 219

Love MI, Huber W, Anders S (2014) Moderated estimation of fold change and dispersion for RNA-seq data with DESeq2. *Genome Biol* 15: 550

Maehama T, Nishio M, Otani J, Mak TW, Suzuki A (2021) The role of Hippo-YAP signaling in squamous cell carcinomas. *Cancer Sci* 112: 51-60

Melendez Garcia R, Haccard O, Chesneau A, Narassimprakash H, Roger J, Perron M, Marheineke K, Bronchain O (2022) A non-transcriptional function of Yap regulates the DNA replication program in Xenopus laevis. *Elife* 11

Milacic M, Beavers D, Conley P, Gong C, Gillespie M, Griss J, Haw R, Jassal B, Matthews L, May B *et al* (2024) The Reactome Pathway Knowledgebase 2024. *Nucleic Acids Res* 52: D672-D678

Mittal P, Roberts CWM (2020) The SWI/SNF complex in cancer - biology, biomarkers and therapy. *Nat Rev Clin Oncol* 17: 435-448

Mohammed H, Taylor C, Brown GD, Papachristou EK, Carroll JS, D'Santos CS (2016) Rapid immunoprecipitation mass spectrometry of endogenous proteins (RIME) for analysis of chromatin complexes. *Nat Protoc* 11: 316-326

Moiseeva TN, Yin Y, Calderon MJ, Qian C, Schamus-Haynes S, Sugitani N, Osmanbeyoglu HU, Rothenberg E, Watkins SC, Bakkenist CJ (2019) An ATR and CHK1 kinase signaling mechanism that limits origin firing during unperturbed DNA replication. *Proc Natl Acad Sci U S A* 116: 13374-13383

Moleirinho S, Hoxha S, Mandati V, Curtale G, Troutman S, Ehmer U, Kissil JL (2017) Regulation of localization and function of the transcriptional co-activator YAP by angiomotin. *Elife* 6

Molinuevo R, Freije A, Contreras L, Sanz JR, Gandarillas A (2020) The DNA damage response links human squamous proliferation with differentiation. *J Cell Biol* 219

Moriyama K, Yoshizawa-Sugata N, Masai H (2018) Oligomer formation and G-quadruplex binding by purified murine Rif1 protein, a key organizer of higher-order chromatin architecture. *J Biol Chem* 293: 3607-3624

Mukherjee C, Tripathi V, Manolika EM, Heijink AM, Ricci G, Merzouk S, de Boer HR, Demmers J, van Vugt M, Ray Chaudhuri A (2019) RIF1 promotes replication fork protection and efficient restart to maintain genome stability. *Nat Commun* 10: 3287

Nappi A, Miro C, Pezone A, Tramontano A, Di Cicco E, Sagliocchi S, Cicatiello AG, Murolo M, Torabinejad S, Abbotto E *et al* (2023) Loss of p53 activates thyroid hormone via type 2 deiodinase and enhances DNA damage. *Nat Commun* 14: 1244

Negri VA, Logtenberg MEW, Renz LM, Oules B, Walko G, Watt FM (2019) Delta-like 1-mediated cis-inhibition of Jagged1/2 signalling inhibits differentiation of human epidermal cells in culture. *Sci Rep* 9: 10825

Ning B, Tilston-Lunel AM, Simonetti J, Hicks-Berthet J, Matschulat A, Pfefferkorn R, Spira A, Edwards M, Mazzilli S, Lenburg ME *et al* (2023) Convergence of YAP/TAZ, TEAD and TP63 activity is associated with bronchial premalignant severity and progression. *J Exp Clin Cancer Res* 42: 116

Nishio M, Hamada K, Kawahara K, Sasaki M, Noguchi F, Chiba S, Mizuno K, Suzuki SO, Dong Y, Tokuda M *et al* (2012) Cancer susceptibility and embryonic lethality in Mob1a/1b double-mutant mice. *J Clin Invest* 122: 4505-4518

Nowak DE, Tian B, Brasier AR (2005) Two-step cross-linking method for identification of NF-kappaB gene network by chromatin immunoprecipitation. *Biotechniques* 39: 715-725

Omori H, Nishio M, Masuda M, Miyachi Y, Ueda F, Nakano T, Sato K, Mimori K, Taguchi K, Hikasa H *et al* (2020) YAP1 is a potent driver of the onset and progression of oral squamous cell carcinoma. *Sci Adv* 6: eaay3324

1378 Pattschull G, Walz S, Grundl M, Schwab M, Ruhl E, Baluapuri A, Cindric-Vranesic A, Kneitz S, Wolf E,
1379 Ade CP *et al* (2019) The Myb-MuvB Complex Is Required for YAP-Dependent Transcription of Mitotic
1380 Genes. *Cell Rep* 27: 3533-3546 e3537
1381 Petermann E, Orta ML, Issaeva N, Schultz N, Helleday T (2010) Hydroxyurea-stalled replication forks
1382 become progressively inactivated and require two different RAD51-mediated pathways for restart and
1383 repair. *Mol Cell* 37: 492-502
1384 Piccolo S, Panciera T, Contessotto P, Cordenonsi M (2023) YAP/TAZ as master regulators in cancer:
1385 modulation, function and therapeutic approaches. *Nat Cancer* 4: 9-26
1386 Ponten F, Jirstrom K, Uhlen M (2008) The Human Protein Atlas--a tool for pathology. *J Pathol* 216: 387-
1387 393
1388 Proby CM, Purdie KJ, Sexton CJ, Purkis P, Navsaria HA, Stables JN, Leigh IM (2000) Spontaneous
1389 keratinocyte cell lines representing early and advanced stages of malignant transformation of the
1390 epidermis. *Exp Dermatol* 9: 104-117
1391 Ragni CV, Diguet N, Le Garrec JF, Novotova M, Resende TP, Pop S, Charon N, Guillemot L, Kitasato L,
1392 Badouel C *et al* (2017) Amotl1 mediates sequestration of the Hippo effector Yap1 downstream of Fat4
1393 to restrict heart growth. *Nat Commun* 8: 14582
1394 Ratushny V, Gober MD, Hick R, Ridky TW, Seykora JT (2012) From keratinocyte to cancer: the
1395 pathogenesis and modeling of cutaneous squamous cell carcinoma. *J Clin Invest* 122: 464-472
1396 Rheinwald JG (1980) Serial cultivation of normal human epidermal keratinocytes. *Methods Cell Biol*
1397 21A: 229-254
1398 Rheinwald JG, Beckett MA (1981) Tumorigenic keratinocyte lines requiring anchorage and fibroblast
1399 support cultured from human squamous cell carcinomas. *Cancer Res* 41: 1657-1663
1400 Rheinwald JG, Green H (1975) Serial cultivation of strains of human epidermal keratinocytes: the
1401 formation of keratinizing colonies from single cells. *Cell* 6: 331-343
1402 Saladi SV, Ross K, Karaayvaz M, Tata PR, Mou H, Rajagopal J, Ramaswamy S, Ellisen LW (2017) ACTL6A
1403 Is Co-Amplified with p63 in Squamous Cell Carcinoma to Drive YAP Activation, Regenerative
1404 Proliferation, and Poor Prognosis. *Cancer Cell* 31: 35-49
1405 Sanchez-Danes A, Blanpain C (2018) Deciphering the cells of origin of squamous cell carcinomas. *Nat*
1406 *Rev Cancer* 18: 549-561
1407 Schlegelmilch K, Mohseni M, Kirak O, Pruszak J, Rodriguez JR, Zhou D, Kreger BT, Vasioukhin V, Avruch
1408 J, Brummelkamp TR *et al* (2011) Yap1 acts downstream of alpha-catenin to control epidermal
1409 proliferation. *Cell* 144: 782-795
1410 Shin E, Kim J (2020) The potential role of YAP in head and neck squamous cell carcinoma. *Exp Mol Med*
1411 52: 1264-1274
1412 Stojkovic-Filipovic J, Brasanac D, Bosic M, Boricic N, Lekic B (2018) Expression of Minichromosome
1413 Maintenance Proteins in Actinic Keratosis and Squamous Cell Carcinoma. *Appl Immunohistochem Mol*
1414 *Morphol* 26: 165-172
1415 Subramanian A, Tamayo P, Mootha VK, Mukherjee S, Ebert BL, Gillette MA, Paulovich A, Pomeroy SL,
1416 Golub TR, Lander ES *et al* (2005) Gene set enrichment analysis: a knowledge-based approach for
1417 interpreting genome-wide expression profiles. *Proc Natl Acad Sci U S A* 102: 15545-15550
1418 Szklarczyk D, Gable AL, Lyon D, Junge A, Wyder S, Huerta-Cepas J, Simonovic M, Doncheva NT, Morris
1419 JH, Bork P (2019) STRING v11: protein–protein association networks with increased coverage,
1420 supporting functional discovery in genome-wide experimental datasets. *Nucleic acids research* 47:
1421 D607-D613
1422 Takahashi N, Kim S, Schultz CW, Rajapakse VN, Zhang Y, Redon CE, Fu H, Pongor L, Kumar S, Pommier
1423 Y *et al* (2022) Replication stress defines distinct molecular subtypes across cancers. *Cancer Res*
1424 *Commun* 2: 503-517
1425 Todaro GJ, Lazar GK, Green H (1965) The initiation of cell division in a contact-inhibited mammalian
1426 cell line. *J Cell Physiol* 66: 325-333

1427 Topley GI, Okuyama R, Gonzales JG, Conti C, Dotto GP (1999) p21(WAF1/Cip1) functions as a
1428 suppressor of malignant skin tumor formation and a determinant of keratinocyte stem-cell potential.
1429 *Proc Natl Acad Sci U S A* 96: 9089-9094
1430 Uhlen M, Fagerberg L, Hallstrom BM, Lindskog C, Oksvold P, Mardinoglu A, Sivertsson A, Kampf C,
1431 Sjostedt E, Asplund A *et al* (2015) Proteomics. Tissue-based map of the human proteome. *Science* 347:
1432 1260419
1433 Vincent-Mistiaen Z, Elbediwy A, Vanyai H, Cotton J, Stamp G, Nye E, Spencer-Dene B, Thomas GJ, Mao
1434 J, Thompson B (2018) YAP drives cutaneous squamous cell carcinoma formation and progression. *Elife*
1435 7
1436 Walko G, Woodhouse S, Pisco AO, Rognoni E, Liakath-Ali K, Lichtenberger BM, Mishra A, Telerman SB,
1437 Viswanathan P, Logtenberg M *et al* (2017) A genome-wide screen identifies YAP/WBP2 interplay
1438 conferring growth advantage on human epidermal stem cells. *Nat Commun* 8: 14744
1439 Wang H, Zhao A, Chen L, Zhong X, Liao J, Gao M, Cai M, Lee DH, Li J, Chowdhury D *et al* (2009) Human
1440 RIF1 encodes an anti-apoptotic factor required for DNA repair. *Carcinogenesis* 30: 1314-1319
1441 Wang J, Harwood CA, Bailey E, Bewicke-Copley F, Anene CA, Thomson J, Qamar MJ, Laban R, Nourse
1442 C, Schoenherr C *et al* (2023) Transcriptomic analysis of cutaneous squamous cell carcinoma reveals a
1443 multigene prognostic signature associated with metastasis. *J Am Acad Dermatol* 89: 1159-1166
1444 Wang P, Bai Y, Song B, Wang Y, Liu D, Lai Y, Bi X, Yuan Z (2011) PP1A-mediated dephosphorylation
1445 positively regulates YAP2 activity. *PLoS One* 6: e24288
1446 Weichselbaum R, Dahlberg W, Little JB, Ervin TJ, Miller D, Hellman S, Rheinwald JG (1984) Cellular X-
1447 ray repair parameters of early passage squamous cell carcinoma lines derived from patients with
1448 known responses to radiotherapy. *Br J Cancer* 49: 595-601
1449 Winer D, Alsaad KO, Bray P, Smith R, Ghazarian D (2006) Early onset cutaneous squamous cell
1450 carcinoma associated with neurofibromatosis type 2 (NF2). *Eur J Dermatol* 16: 448-449
1451 Winge MCG, Kellman LN, Guo K, Tang JY, Swetter SM, Aasi SZ, Sarin KY, Chang ALS, Khavari PA (2023)
1452 Advances in cutaneous squamous cell carcinoma. *Nat Rev Cancer* 23: 430-449
1453 Xie X, Clausen OP, Boysen M (2002) Prognostic significance of p21WAF1/CIP1 expression in tongue
1454 squamous cell carcinomas. *Arch Otolaryngol Head Neck Surg* 128: 897-902
1455 Xu S, Hu E, Cai Y, Xie Z, Luo X, Zhan L, Tang W, Wang Q, Liu B, Wang R *et al* (2024) Using clusterProfiler
1456 to characterize multiomics data. *Nat Protoc* 19: 3292-3320
1457 Yamazaki S, Ishii A, Kanoh Y, Oda M, Nishito Y, Masai H (2012) Rif1 regulates the replication timing
1458 domains on the human genome. *EMBO J* 31: 3667-3677
1459 Yanofsky VR, Mercer SE, Phelps RG (2011) Histopathological variants of cutaneous squamous cell
1460 carcinoma: a review. *J Skin Cancer* 2011: 210813
1461 Yoshizawa-Sugata N, Yamazaki S, Mita-Yoshida K, Ono T, Nishito Y, Masai H (2021) Loss of full-length
1462 DNA replication regulator Rif1 in two-cell embryos is associated with zygotic transcriptional activation.
1463 *J Biol Chem* 297: 101367
1464 Yuan Y, Park J, Feng A, Awasthi P, Wang Z, Chen Q, Iglesias-Bartolome R (2020) YAP1/TAZ-TEAD
1465 transcriptional networks maintain skin homeostasis by regulating cell proliferation and limiting KLF4
1466 activity. *Nat Commun* 11: 1472
1467 Yuan Y, Salinas Parra N, Chen Q, Iglesias-Bartolome R (2021) Oncogenic Hedgehog-smoothened
1468 signaling depends on YAP1-TAZ/TEAD transcription to restrain differentiation in basal cell carcinoma. *J*
1469 *Invest Dermatol*
1470 Zanconato F, Battilana G, Forcato M, Filippi L, Azzolin L, Manfrin A, Quaranta E, Di Biagio D, Sigismondo
1471 G, Guzzardo V *et al* (2018) Transcriptional addiction in cancer cells is mediated by YAP/TAZ through
1472 BRD4. *Nat Med* 24: 1599-1610
1473 Zanconato F, Forcato M, Battilana G, Azzolin L, Quaranta E, Bodega B, Rosato A, Bicciato S, Cordenonsi
1474 M, Piccolo S (2015) Genome-wide association between YAP/TAZ/TEAD and AP-1 at enhancers drives
1475 oncogenic growth. *Nat Cell Biol* 17: 1218-1227

1476 Zhang N, Bai H, David KK, Dong J, Zheng Y, Cai J, Giovannini M, Liu P, Anders RA, Pan D (2010) The
1477 Merlin/NF2 tumor suppressor functions through the YAP oncoprotein to regulate tissue homeostasis
1478 in mammals. *Dev Cell* 19: 27-38
1479 Zhang X, Tang JZ, Vergara IA, Zhang Y, Szeto P, Yang L, Mintoff C, Colebatch A, McIntosh L, Mitchell KA
1480 *et al* (2019) Somatic Hypermutation of the YAP Oncogene in a Human Cutaneous Melanoma. *Molecular*
1481 *cancer research : MCR* 17: 1435-1449
1482 Zhang Y, Chen F, Chandrashekar DS, Varambally S, Creighton CJ (2022) Proteogenomic characterization
1483 of 2002 human cancers reveals pan-cancer molecular subtypes and associated pathways. *Nat Commun*
1484 13: 2669
1485 Zhou Y, Zhang J, Li H, Huang T, Wong CC, Wu F, Wu M, Weng N, Liu L, Cheng ASL *et al* (2020) AMOTL1
1486 enhances YAP1 stability and promotes YAP1-driven gastric oncogenesis. *Oncogene* 39: 4375-4389
1487 Zhu M, Peng R, Liang X, Lan Z, Tang M, Hou P, Song JH, Mak CSL, Park J, Zheng SE *et al* (2021) P4HA2-
1488 induced prolyl hydroxylation suppresses YAP1-mediated prostate cancer cell migration, invasion, and
1489 metastasis. *Oncogene* 40: 6049-6056

1490

1491 **Figure legends**

1492 ***Figure 1. RIME identifies RIF1 as an interactor of chromatin-associated YAP in squamous cell***

1493 ***carcinoma cells.***

1494 (**A**) Interaction network of YAP protein interactors identified by RIME in SCC13 cells. Oval

1495 nodes indicate proteins that were previously identified as candidate regulators of SCC13 cell

1496 proliferation and/or survival in a genome wide RNA-interference (RNAi) screen (hit:

1497 'Yes')(Walko *et al.*, 2017), while rectangular shaped nodes indicate proteins that were not

1498 identified in the RNAi screen (hit: 'No'). Red connecting lines (edges) show previously

1499 identified YAP interactions according to the STRING Homo sapiens database, and nodes with

1500 red borders indicate known YAP interactors (manually curated from STRING and literature

1501 search); dashed red lines show manually curated known YAP interactions that were not yet

1502 present in the STRING database. Proteins were manually grouped based on function (gene

1503 names displayed, generated in Cytoscape 3.9.1 using STRING app 1.7.1). (**B**) Gene ontology

1504 terms ('molecular functions' and 'biological process') enriched within the high-confidence

1505 YAP-interacting proteins identified by RIME. (**C**) Confocal fluorescence images (z-projections)

1506 of YAP (green) and RIF1 (red) nuclear localisation in SCC13 cells. DNA was counterstained with

1507 Hoechst dye DAPI (blue). Scale bar, 10 µm. (**D**, **E**) Immunoblotting analysis of YAP and IgG-
1508 control immunoprecipitates and respective inputs from SCC13 (D) whole cell extracts and (E)
1509 and nuclei-enriched fractions using the indicated antibodies. Blots from one representative
1510 experiment out of two (D) and three (E) are shown. (**F**, **G**) Representative confocal microscopy
1511 images (z-projections) and image quantifications of (F) YAP-RIF1 and (G) YAP-TEAD1 in-situ PLA
1512 in control (siNTC/shNTC) and YAP/TAZ knockdown (siYAP&TAZ/shYAP) cells (PLA signal, green;
1513 DNA (DAPI) blue; n >250 cells (YAP-RIF1), n >500 cells (YAP-TEAD1) per condition in n-3
1514 independent experiments). Scale bars, 5 µm. Datapoints show fold decrease in mean nuclear
1515 PLA signal intensity in siYAP&TAZ/shYAP cells compared to siNTC/shNTC cells. Lines show
1516 means from all three experiments, error bars show SD. Exact p-values are shown, one sample
1517 two-tailed *t* test.
1518
1519 ***Figure 2. YAP/TAZ-mediated oncogenic transcriptional programmes control the balance***
1520 ***between proliferation and differentiation in squamous cell carcinoma.***
1521 (**A**,) Significantly enriched or depleted RNAs in siYAP/TAZ SCC13 cells identified by RNA-Seq
1522 analysis using DESeq2. Volcano plot shows statistical significance (-log 10 (p-value)) versus
1523 relative RNA abundance (log2 -fold change) in siYAP/TAZ compared to siNTC cells. The vertical
1524 dotted grey lines identify the log2-fold change cut-off (0.58, 1.5-fold change). The horizontal
1525 grey dotted lines identify the cut-off for statistical significance (p<0.05). (**B**) Heatmaps show
1526 the log2-fold change of selected genes relating to cell cycle control, the epidermal
1527 differentiation complex, and transcriptional regulators of terminal differentiation. Black colour
1528 indicates that the gene is not differentially regulated in the pairwise comparison. (**C**)
1529 Photograph shows lack of medium acidification by doxycycline-induced shYAP SCC13 cells
1530 compared to shNTC cells during a 4-day culture period indicative of decreased proliferation.

1531 (**D**) Immunoblot analysis of SCC13 cells expressing doxycycline-induced shYAP, shTAZ, or
1532 shNTC, using the indicated antibodies. Actin and cyclophilin B (CBP) were used as loading
1533 controls. (**E**) Cell cycle analysis by propidium iodide (PI) labelling of asynchronous populations
1534 of shNTC and shYAP SCC13 cells (grey profiles) and of cells synchronised at the G1/S boundary
1535 by double thymidine block (dTb) at indicated time points. Note that the doxycycline treatment
1536 required for induction of shRNA expression slightly reduces cell proliferation (compare with
1537 Fig. 6A). One out of n=2 independent experiments is shown. (**F**) Colony formation assays were
1538 quantified by measuring the percentage of well area occupied by colonies. Bars show the
1539 means from n=3 independent experiments (performed with 3 technical replicates), individual
1540 data points show the means from each experiment, error bars show SD. Exact p-values are
1541 shown, RM one way ANOVA with Geisser-Greenhouse correction and Dunnett's multiple
1542 comparison test. (**G**) Immunoblot analysis of shNTC, shYAP, and shTAZ SCC13 cells using the
1543 indicated antibodies. Tubulin was used as loading control.
1544
1545 ***Figure 3. YAP modulates RIF1 transcription and promotes RIF1 protein stability.***
1546 (**A**,) Significantly enriched or depleted RNAs in siRIF1 SCC13 cells identified by RNA-Seq
1547 analysis using DESeq2. Volcano plot shows statistical significance (-log 10 (p-value)) versus
1548 relative RNA abundance (log2 -fold change) in siRIF1 compared to siNTC cells. The vertical
1549 dotted grey lines identify the log2-fold change cut-off (0.58, 1.5-fold change). The horizontal
1550 grey dotted lines identify the cut-off for statistical significance ($p<0.05$). (**B**) Scatter plot shows
1551 correlations between the 710 genes that were found to be differentially expressed in both
1552 siYAP/TAZ and siRIF1 SCC13 cell datasets. (**C**) qRT-PCR analysis of *RIF1* mRNA expression in
1553 SCC13 cells transfected with an siRNA SMARTpool targeting YAP/TAZ (siY/T) or siNTC. Data
1554 shown are from n=3 independent experiments performed with three technical replicates.

1555 Individual data points represent the mean fold change in mRNA abundance (normalized to
1556 GAPDH) compared to siNTC in each experiment. Bars represent the means from all
1557 experiments, error bars represent SD. Exact p-values are shown, paired *t* test. (**D**, **E**)
1558 Immunoblot analysis of SCC13 cells transfected with (D) an siRNA SMARTpool targeting
1559 YAP/TAZ (siY/T) or an siNTC SMARTpool, or (E) expressing different doxycycline-induced shYAP,
1560 shTAZ, or shNTC, using the indicated antibodies. Tubulin or cyclophilin B (CBP) were used as
1561 loading controls. In (D) numbers below lanes represent protein ratios relative to an arbitrary
1562 level of 1.0 set for siNTC. (**F**) Log2-fold change in *YAP1* and *RIF1* mRNA abundances (based on
1563 RNA-seq analysis performed in (Yuan *et al.*, 2020)) in N/TERT-2G immortalised NHKs
1564 transfected with YAP/TAZ-targeting siRNAs (siY/T) compared N/TERT-2G cells transfected with
1565 siNTC. (**G**) Correlation analysis between the single sample GSEA scores for the MSigDB
1566 GO:Hippo_Signalling gene set and *RIF1* mRNA expression levels (batch corrected, 24Q2
1567 release) in a panel of 64 HNSCC cell lines. Spearman correlation coefficient and statistical
1568 significance are indicated. (**H**) Immunoblot analysis of RIF1 protein levels in SCC13 cells
1569 transfected with siRNA SMARTpools targeting TEAD1, TEAD3, TEAD4, or YAP/TAZ (siY/T), or an
1570 siNTC SMARTpool. Cyclophilin B (CBP) was used as loading control. Lower panel, quantification
1571 of RIF1 protein expression. Individual data points show fold change in RIF1 protein levels
1572 (normalised to tubulin) in siTEAD1, siTEAD3, siTEAD4, siTEAD1/3/4, and siY/T compared to
1573 siNTC in n=3 different experiments, bars show the mean, error bars show SD. (**I**) Immunoblot
1574 analysis, using the indicated antibodies, of SCC13 cells expressing a doxycycline-induced shYAP
1575 or a shNTC, treated for the indicated times with cycloheximide (CHX, 100 µg/ml). Cyclophilin
1576 B (CBP) was used as loading control.

1577

1578 ***Figure 4. Increased association of YAP with RIF1 in response to replication stress.***

1579 (**A**) Immunoblot analysis of chromatin fractions from SCC13 cells expressing a doxycycline-
1580 induced shYAP or shNTC, using the indicated antibodies. Cells were synchronised at the G1/S
1581 boundary by double thymidine block (dTB) and released into the S phase. Samples were taken
1582 at the indicated timepoints. Histone H3 (HH3) was used as loading control. Blots from one
1583 representative experiment out of two are shown. (**B**, **C**) Representative confocal microscopy
1584 images of (B) z-projection and (C); orthogonal projection of YAP-RIF1 in-situ PLA in SCC13 cells
1585 (PLA signal, green; DNA (DAPI) blue). In (B) cells were labelled with a 1-hour EdU pulse prior
1586 to fixation (EdU signal, red). Arrows in (C) indicate cells completing mitosis. Scale bars, 5 µm.
1587 (**D**) Immunoblot analysis of SCC13 control cells and cells exposed to 4 mM hydroxyurea (HU)
1588 for 24 hours, using the indicated antibodies. Washout, medium removal and replacement with
1589 fresh medium. Tubulin and cyclophilin B (CBP) were used as loading controls. (**E**, **F**) Image
1590 quantifications of (E) YAP-RIF1 and (F) YAP-γH2AX in-situ PLA in SCC13 cells treated with 4 mM
1591 HU for the indicated times. >200 cells were measured per experimental condition in n=3
1592 independent experiments. Superplots show nuclear PLA signal intensity per cell (grey
1593 datapoints), mean nuclear PLA signal intensity of the respective cell populations in each of
1594 n=3 experiments (black datapoints), and mean nuclear PLA signal intensity from all three
1595 experiments (lines). Error bars show SD from all three experiments. Exact p-values are shown.
1596 (E) Brown-Forsythe and Welsh ANOVA test with Dunett's multiple comparison test, (F)
1597 unpaired *t* test.
1598
1599 ***Figure 5. Increased expression of RIF1 in squamous cell carcinoma.***
1600 (**A**) Immunoblot analysis of normal human epidermal keratinocytes (NHKs), keratinocytes
1601 isolated from a pre-malignant dysplastic skin lesion (PM1), various cell lines isolated from
1602 primary cutaneous SCCs (cSCC; SCC13, SCC-NR, MET1), a recurrent cSCC (MET2), and a lymph

1603 node metastasis (MET4), using the indicated antibodies. Actin was used as loading control. (**B**,
1604 **C**) Quantification (B) and representative images (C) of RIF1 expression in healthy adult human
1605 skin (HS), nodular (Nod) and (Inf) infiltrative basal cell carcinoma (BCC), and well-differentiated
1606 (WD) and poorly differentiated (PD) cSCC. Tissue sections were immunolabelled with
1607 antibodies against RIF1 (green), and keratin 14 (Krt14, blue) to identify normal and neoplastic
1608 epidermal keratinocytes. White dotted line demarcates dermal–epidermal boundary in HS.
1609 Scale bar, 50 µm. Superplots in (B) show percentage of RIF1-positive keratinocytes in different
1610 areas of the same tumour (coloured symbols), mean percentage of RIF1-positive keratinocytes
1611 in 3–5 different patient samples (black datapoints), and mean percentage of RIF1-positive
1612 keratinocytes in each sample group (lines). Error bars show SD from each sample group.
1613 *$p < 0.05$, Brown-Forsythe and Welsh ANOVA test with Dunett's multiple comparison test. (**D**,
1614 **E**) RIF1 protein expression in HNSCC samples from the Clinical Proteomic Tumour Analysis
1615 Consortium (CPTAC), stratified according to (D) tumour stage, or (E) presence of alterations
1616 in the Hippo pathway or other signalling pathways. Jitter plots (overlayed onto box plots) show
1617 Z-values (standard deviations from the median across samples for the given sample type) from
1618 individual samples. Box plots indicate the median (middle line), 25th percentile (bottom line),
1619 75th percentile (top line), and minimum and maximum (whiskers). Log2 spectral count ratio
1620 values from CPTAC were first normalized within each sample profile, then normalized across
1621 samples. Graphs were downloaded from the UALCAN database
1622 (https://ualcan.path.uab.edu/). (D) $p < 0.05$ for all pairwise comparisons. In (E) exact p-values
1623 are shown.
1624
1625 ***Figure 6. Depletion of RIF1 in squamous cell carcinoma cells affect DNA replication dynamics.***

1626 (**A**) Cell cycle analysis by PI labelling of asynchronous populations of shNTC and shRIF1 (shRIF1-
1627 017, see (B)) SCC13 cells (grey profiles) and of cells synchronised at the G1/S boundary by
1628 double thymidine block (dTb) and released into S-phase (T=hours post thymidine release,
1629 coloured profiles). One of n=2 experiments is shown. (**B**, **C**) Immunoblot analysis of (B) cell
1630 extracts and (C) chromatin fractions from shNTC and shRIF1 SCC13 cells, using the indicated
1631 antibodies. In (C) cells were synchronised at the G1/S boundary by double thymidine block
1632 (dTB) and released into the S phase. Samples were taken at the indicated timepoints. Note
1633 that DDK-induced phosphorylation of MCM4 results in a band shift. Cyclophilin B (CPB),
1634 tubulin, and histone H3 (HH3) were used as loading controls. shRIF1-017 was used in
1635 experiments shown in (A, C).
1636
1637 ***Figure 7. RIF1 protects against endogenous and exogenous replication stress.***
1638 (**A**) Immunoblott analysis of cell extracts from SCC13 cells expressing shNTC or different
1639 shRIF1, using the indicated antibodies. Cyclophilin B (CPB), and tubulin were used as loading
1640 controls. Cells treated for 24 hours with 4 mM HU served as positive controls for severe
1641 replication stress. The position of the RPA32 band is indicated with an arrow. (**B**)
1642 Representative cell cycle profile (PI labelling following a 30-minute EdU pulse) of
1643 unsynchronised shNTC and shRIF1 SCC13 cells. Gates used for quantification and percentages
1644 of cells in different cell cycle phases are indicated. One out of n=4 independent experiments
1645 is shown. (**C**) Immunoblot analysis of cell extracts from SCC13 cells expressing shNTC or
1646 different shRIF1, using the indicated antibodies. Tubulin was used as loading control. (**D**)
1647 Representative images of colony formation efficiency of shNTC and shRIF1 SCC13 cells. Cells
1648 in triplicate wells were stained with crystal violet. Colony formation assays were quantified by
1649 measuring the percentage of well area occupied by colonies. Bars show the means from n=3

independent experiments (performed with 3 technical replicates), individual data points show the means from each experiment, error bars show SD. Exact p-values are shown, RM one way ANOVA with Geisser-Greenhouse correction and Dunnett's multiple comparison test. (**E, F**) Synergism of YAP depletion (shYAP) and HU treatment on clonal colony growth was quantified by measuring the percentage of well area occupied by colonies after 10 days in culture. In (F) values have been normalized to controls (no HU treatment) for shYAP and shNTC. Bars show the means from n=3 independent experiments (performed with 3 technical replicates), individual data points show the means from each experiment, error bars show SD. p-values are shown for multiple comparisons, RM two-way ANOVA with Geisser-Greenhouse correction (matched values both stacked and spread across rows) and Šidak's multiple comparison test. *p<0.05, **p<0.01, ***p<0.001. Sources of variation in (E): HU concentration, p=0.04; shRNA, p=0.002; HU concentration x shRNA, p<0.001. Sources of variation in (F): HU concentration, p=0.008; shRNA, p=0.02; HU concentration x shRNA, p=0.007.

Supplementary Figure 1. Validation of YAP antibody and cell culture conditions for RIME.

(**A**) Immunoblot analysis of cell extracts from SCC13 cells expressing a non-targeting control shRNA (shNTC), two different shRNAs targeting YAP (shYAP-1, shYAP-2), or two different shRNAs targeting TAZ (shTAZ-1, shTAZ-2) using the indicated antibodies. Note that the rabbit anti-human YAP antibody used for RIME (Y1200-01D, US Biologicals) did not recognize TAZ. Tubulin was used as loading control. (**B**) Representative wide-field microscopy images of YAP/TAZ (monoclonal anti-YAP/TAZ antibody, clone 63.7, Santa Cruz) nuclear localisation in NHK and SCC13 cells prior to RIME experiments. F-actin was counterstained with phalloidin. Scale bar, 100 µm. (**C**) Coverage of bait protein YAP across both experiments and all technical

1674 replicates. Regions shown in blue represent peptides detected by mass spectrometry. Km5 =
1675 NHK cells, strain km, passage 5.
1676
1677 ***Supplementary Figure 2. RIME identifies RIF1 as an interactor of chromatin-associated YAP***
1678 ***in normal human keratinocytes.***
1679 (**A**) Interaction network of YAP protein interactors identified by RIME in NHKs. Red connecting
1680 lines (edges) show previously identified YAP interactions according to the STRING Homo
1681 sapiens database, and nodes with red borders indicate known YAP interactors (manually
1682 curated from STRING and literature search); dashed red lines show manually curated known
1683 YAP interactions that were not yet present in the STRING database. Proteins were manually
1684 grouped based on function (gene names displayed, generated in Cytoscape 3.9.1 using STRING
1685 app 1.7.1). (**B**) Gene ontology terms ('molecular functions' and 'biological process') enriched
1686 within the high-confidence YAP-interacting proteins identified by RIME in NHKs. (**C**) Mean
1687 spectral counts (total number of identified peptide spectra per protein) for YAP and RIF1 in
1688 the YAP-RIME from the two independently performed experiments in SCC13 and NHK cells.
1689 (**D**) Immunoblot analysis of chromatin fractions from NHK and SCC13 cells, using the indicated
1690 antibodies. Similar amounts of total chromatin-associated proteins were loaded on SDS-PAGE,
1691 as validated by Coomassie staining.
1692
1693 ***Supplementary Figure 3. Validation of YAP/TAZ knockdown efficiency and antibody***
1694 ***specificity for in-situ PLA experiments, and confirmation of YAP-RIF1 interaction in HARA***
1695 ***lung squamous cell carcinoma cells.***
1696 (**A**) Immunoblot analysis of YAP (rabbit monoclonal anti-YAP antibody; D8H1X, Cell Signalling))
1697 and IgG-control immunoprecipitates and respective inputs from SCC13 cell extracts using the

1698 indicated antibodies. (**B**) Immunoblot analysis of lysates from cells used in in-situ PLA
1699 experiments shown in Fig. 1F and 1G. To achieve the strongest YAP/TAZ depletion possible,
1700 SCC13 cells expressing inducible shNTC or shYAP were treated with doxycycline for 72 hours
1701 and were in parallel also transfected with non-targeting control or YAP/TAZ-targeting siRNA
1702 SMARTpools, respectively. Tubulin was used as loading control. (**C**, **D**) Representative confocal
1703 microscopy images (z-projections) of in-situ PLA (PLA signal, green; DNA (DAPI)) blue) in cells
1704 labelled with (C) no primary antibodies or (D) only one of the two primary antibodies. Scale
1705 bars, 5 µm. (**E**) Representative confocal microscopy images (z-projections) of YAP-RIF1 in-situ
1706 PLA (PLA signal, green; DNA (DAPI)) blue in miotic cells. Scale bars, 5 µm. (**F**) Confocal
1707 fluorescence image (z-projection) of YAP (green) and RIF1 (red) nuclear localisation in HARA
1708 cells. DNA was counterstained with Hoechst dye (DAPI, blue). Scale bar, 10 µm. (**G**)
1709 Immunoblot analysis of YAP and IgG-control immunoprecipitates and respective inputs from
1710 HARA cell nuclei-enriched fractions (treated with Benzonase® nuclease) using the indicated
1711 antibodies. (**H**) Agarose gel electrophoresis of DNA extracts from Benzonase®-treated and
1712 untreated HARA cells shows efficient DNA degradation upon Benzonase® treatment. Left lane:
1713 Thermo Scientific™ GeneRuler 1 kb Plus DNA Ladder (Fisher, UK).
1714
1715 ***Supplementary Figure 4. Gene set enrichment analysis in differentially expressed genes***
1716 ***upon YAP/TAZ knockdown in SCC13 cells.***
1717 (**A**, **B**) Bubble plots show results of gene set enrichment analysis (GSEA) on RNA-seq data from
1718 siYAP/TAZ SCC13 cells. The top 10 downregulated (suppressed) or upregulated (activated)
1719 pathways in siYAP/TAZ SCC13 cells are shown. (**C**) Heatmaps show the log2-fold change of
1720 selected genes representing high confidence YAP/TAZ-TEAD target genes, YAP-MMB target
1721 genes, and genes directly involved in DNA replication, in the indicated pairwise comparisons.

1722 Black colour indicates that the gene is not differentially regulated in that pairwise comparison.
1723 (**D**) GSEA showing enrichment of epidermal late differentiation (upper panel) and progenitor
1724 cell (lower panel) signatures (Lopez-Pajares *et al.*, 2015) among the differentially expressed
1725 genes in siYAP/TAZ (siY/T) versus siNTC SCC13 cells.
1726
1727 ***Supplementary Figure 5. Correlation analysis of YAP/TAZ target genes, replication stress-***
1728 ***associated genes, and RIF1 in HNSCC cell lines.***
1729 (**A**–**C**) Correlation heatmaps of the indicated genes (mean mRNA expression) distinguished by
1730 (A, C) 64 HNSCC or (B) 5 cSCC cell lines. Graphs were exported from the DepMap portal. (**D**–
1731 **F**) Correlation analysis between the expression of replication stress-associated genes and (D)
1732 YAP/TAZ target genes or (E) *RIF1* mRNA expression levels (expression public 24Q2 release),
1733 and (F) correlation of YAP/TAZ target genes and *RIF1* mRNA expression levels in a panel of 64
1734 HNSCC cell lines. Spearman correlation coefficient and statistical significance are indicated.
1735 Data were accessed using the DepMap portal (https://depmap.org/portal/).
1736
1737 ***Supplementary Figure 6. Cell cycle withdrawal and terminal differentiation commitment of***
1738 ***SCC cells upon conditional YAP depletion are reversible.***
1739 Phase contrast images show morphological appearance of shNTC and shYAP SCC13 cells
1740 growing in the presence of doxycycline (dox), and at the indicated timepoint after doxycycline
1741 withdrawal. Note reduced density, impaired colony formation, and elongated and flattened
1742 shape (indicative of terminal differentiation (Negri *et al*, 2019)) of shYAP cells in the presence
1743 of doxycycline, and rapid recovery of normal cell morphology and growth behaviour upon
1744 doxycycline withdrawal leading to re-expression of YAP.
1745

1746 ***Supplementary Figure 7. Involvement of YAP/TAZ target genes in human cSCC progression.***

1747 Boxplots show the distribution of Gene Set Variation Analysis (GSVA) scores for differentially
1748 expressed genes (DEGs) that were (**A**) downregulated or (**B**) upregulated in siYAP/TAZ SCC13
1749 cells across different cSCC patient samples (Wang *et al.*, 2023). Norm_no_met / tum_no_met:
1750 perilesional normal skin and primary cSCC tissue from patients with no metastasis over 3
1751 years; norm_with_met / tum_with_met: perilesional normal skin and primary cSCC tissue
1752 from patients with metastasis during 3 years follow-up; met: tissue from metastasis. Pairwise
1753 comparisons between sample groups were conducted using a *t* test. The p-values from these
1754 comparisons are indicated above the boxplots with brackets linking the compared groups. The
1755 significance levels are denoted as follows: *: p <= 0.05; **: p <= 0.01; ***: p <= 0.001; ****: p
1756 <= 0.0001.

1757

1758 ***Supplementary Figure 8. Gene set enrichment analysis in differentially expressed genes***
1759 ***upon RIF1 knockdown in SCC13 cells.***

1760 (**A**–**C**) Bubble plots show results of gene set enrichment analysis (GSEA) on RNA-seq data from
1761 siRIF1 SCC13 cells. The top 10 downregulated (suppressed) or upregulated (activated)
1762 pathways in siRIF1 SCC13 cells are shown.

1763

1764 ***Supplementary Figure 9. RIF1 expression in different types of squamous cancers.***

1765 (**A**–**C**) Representative RIF1 immunohistochemistry (anti-RIF1 rabbit polyclonal antibody
1766 HPA036887, Atlas Antibodies) of normal tissue and squamous cell carcinoma tissue from (A)
1767 skin, (B) oral cavity and (C) cervix, exported from the Human Protein Atlas database. NS,
1768 normal skin; cSCC-IS, cutaneous squamous cell carcinoma in-situ; WD cSCC, well differentiated
1769 cSCC; PD cSCC, poorly differentiated cSCC; NOM, normal oral mucosa; WD OSCC, well

1770 differentiated oral SCC; PD, poorly differentiated oral SCC; NC, normal cervix; CeSCC, cervical
1771 SCC. (**D**) RIF1 protein expression across different cancers, with tumour (red) and normal (blue)
1772 samples, from the Clinical Proteomic Tumour Analysis Consortium (CPTAC). Box plots indicate
1773 median Z-values (middle line), 25th percentile (bottom line), 75th percentile (top line), and
1774 minimum and maximum (whiskers). Log2 spectral count ratio values from CPTAC were first
1775 normalized within each sample profile, then normalized across samples. Graphs were
1776 downloaded from the UALCAN database (https://ualcan.path.uab.edu/). BRCA, breast cancer
1777 (18 normal and 125 tumour samples); COAD, colon adenocarcinoma (100 normal and 97
1778 tumour samples); OV, ovarian serous cystadenocarcinoma (25 normal and 100 tumour
1779 samples); KIRC, kidney renal clear cell carcinoma (84 normal and 110 tumour samples); UCEC,
1780 uterine corpus endometrial carcinoma (31 normal and 100 tumour samples); LUAD, lung
1781 adenocarcinoma (111 normal and 111 tumour samples); PAAD, pancreatic adenocarcinoma
1782 (74 normal and 137 tumour samples); HNSCC, head and neck squamous cell carcinoma (71
1783 normal and 108 tumour samples); GBM, glioblastoma multiforme (10 normal and 99 tumour
1784 samples); LIHC, liver hepatocellular carcinoma (165 normal and 165 tumour samples). (**E**–**G**)
1785 RIF1 protein expression in (E) lung SCC, (F) GMB, and (G) OV samples from the Clinical
1786 Proteomic Tumour Analysis Consortium (CPTAC), stratified according to presence of
1787 alterations in the Hippo pathway or other signalling pathways. Jitter plots (overlayed onto box
1788 plots) show Z-values (standard deviations from the median across samples for the given
1789 sample type) from individual samples. Box plots indicate the median (middle line), 25th
1790 percentile (bottom line), 75th percentile (top line), and minimum and maximum (whiskers).
1791 Log2 spectral count ratio values from CPTAC were first normalized within each sample profile,
1792 then normalized across samples. Graphs were downloaded from the UALCAN database
1793 (https://ualcan.path.uab.edu/). Exact p-values are shown.

1794

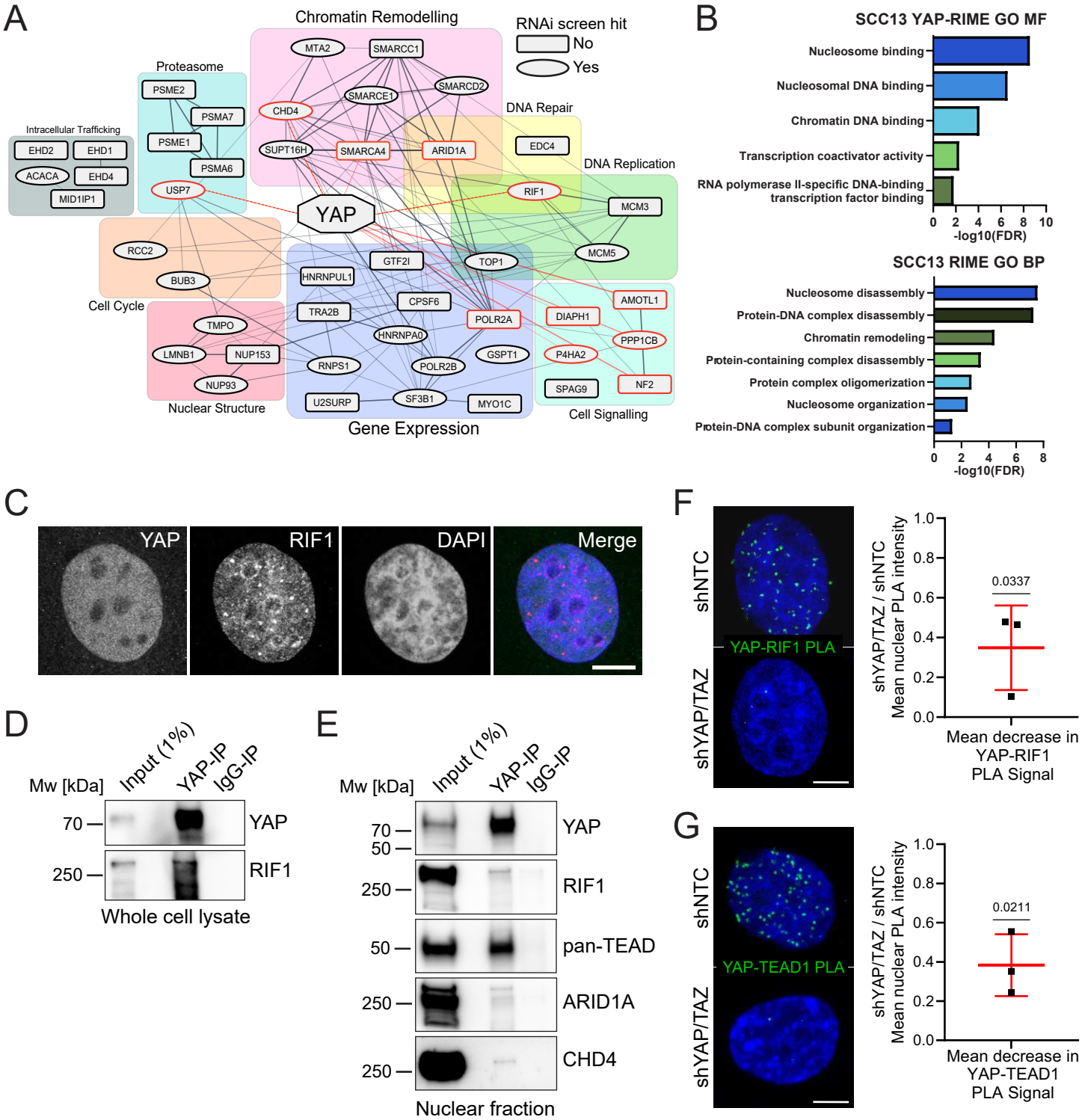

Figure 1_Bojko et al.

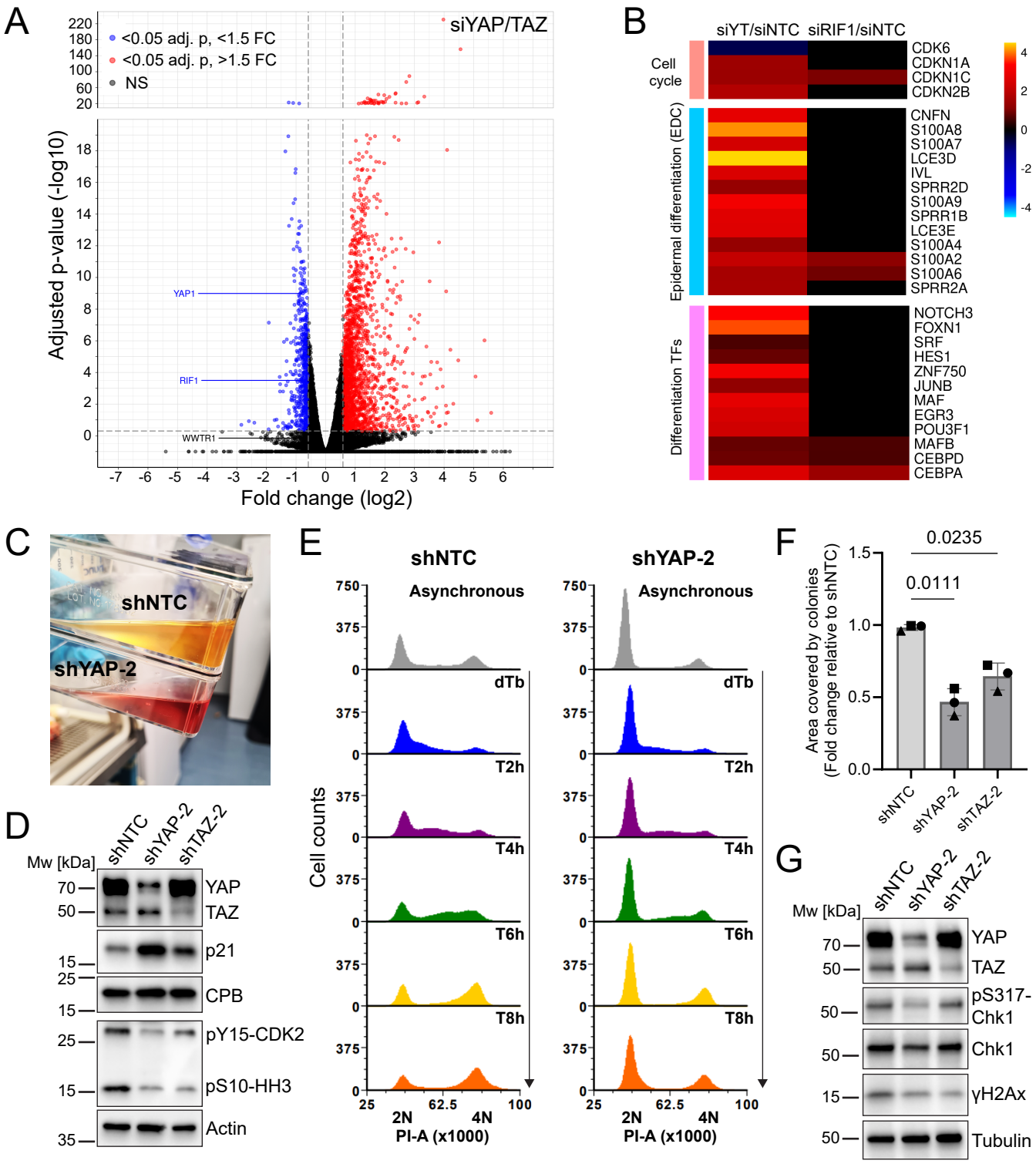

Figure 2_Bojko et al.

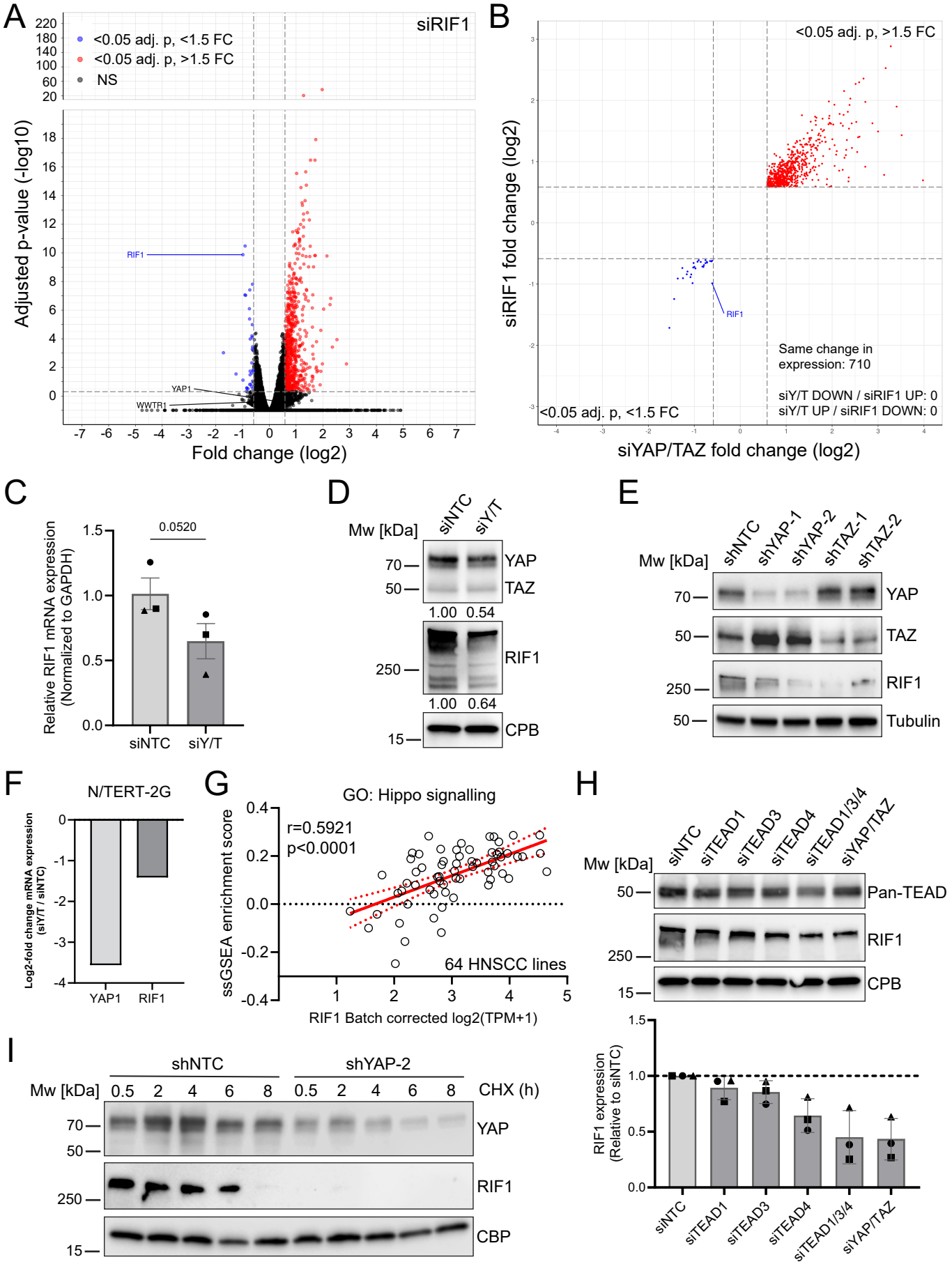

Figure 3_Bojko et al.

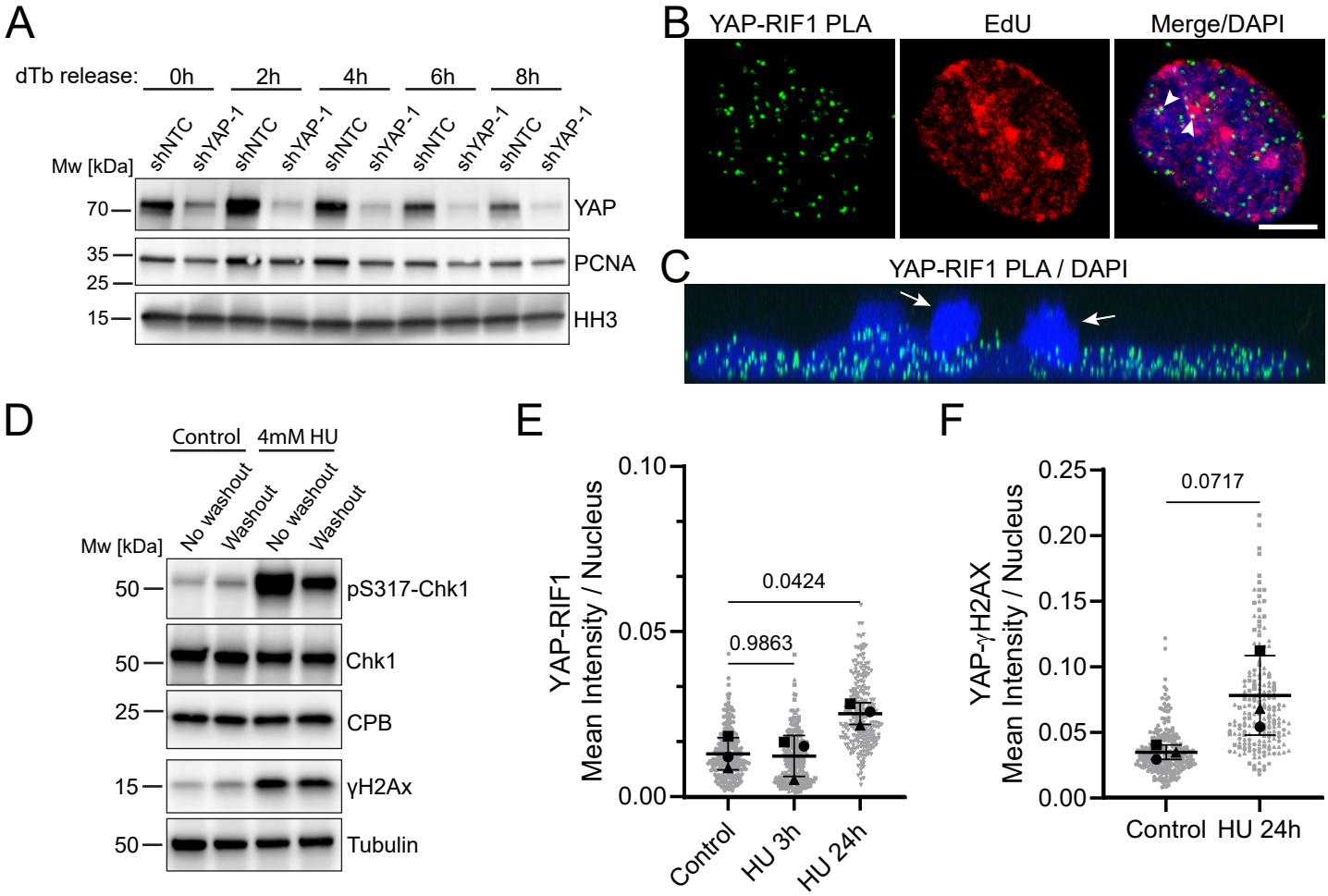

Figure 4_Bojko et al.

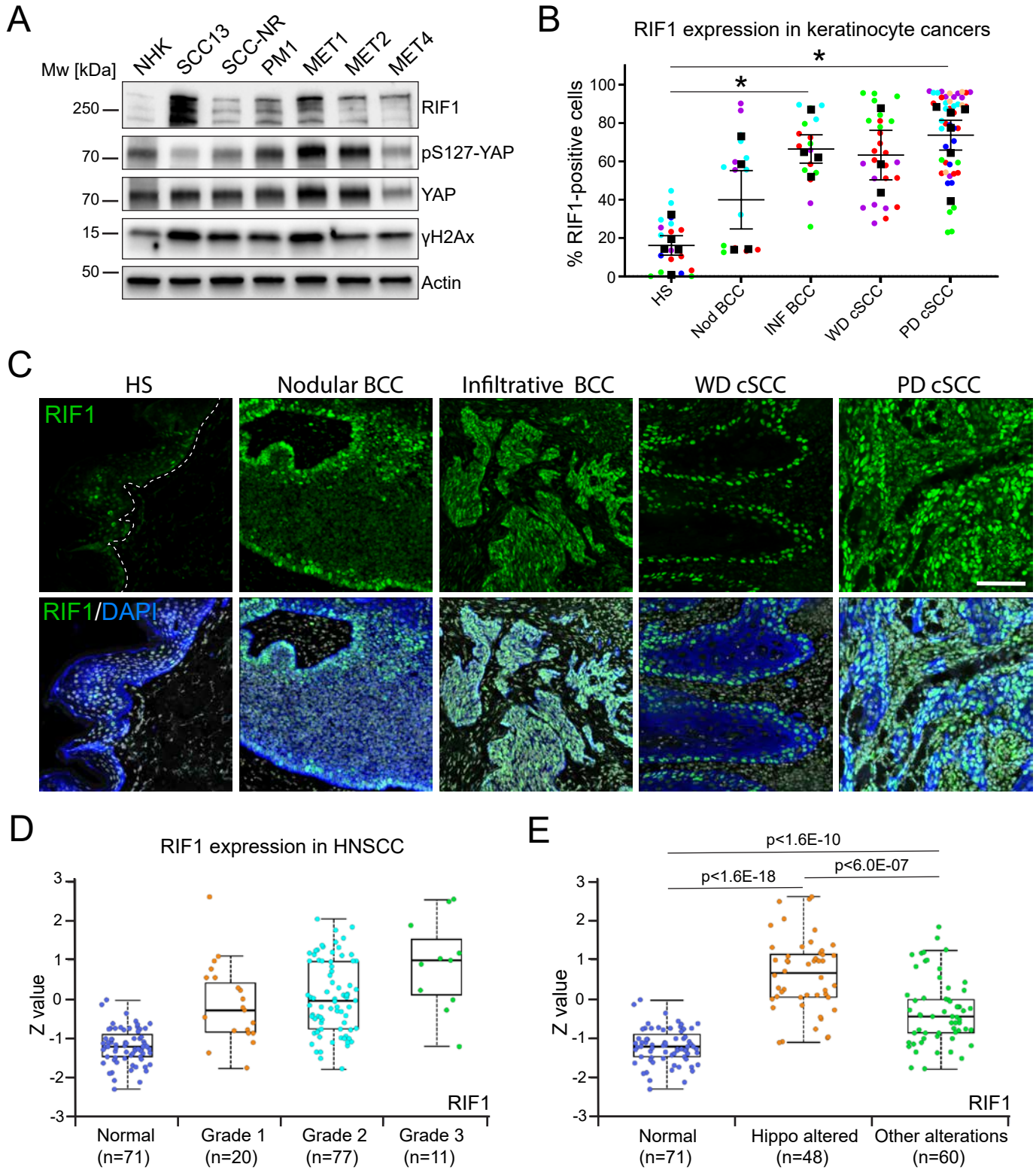

Figure 5_Bojko et al.

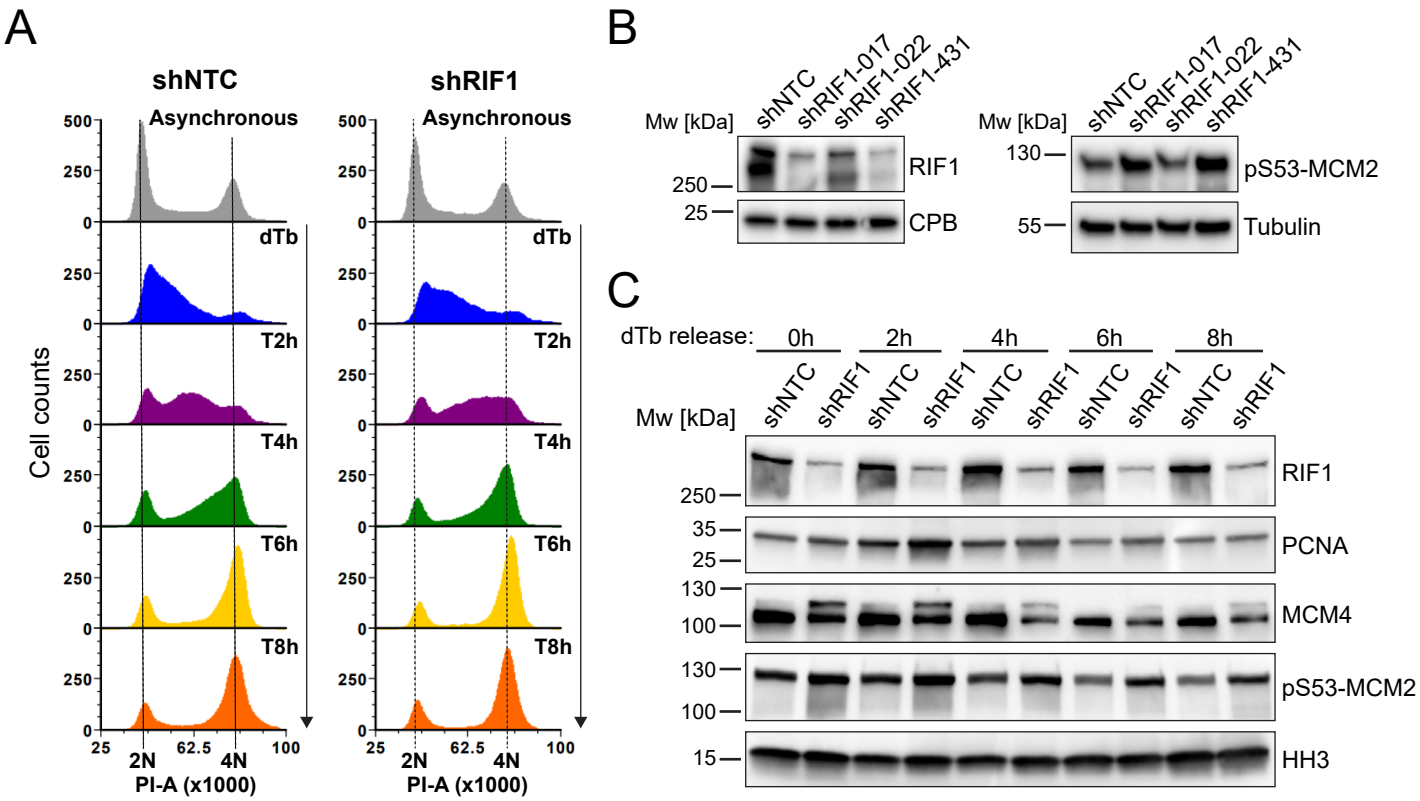

Figure 6_Bojko et al.

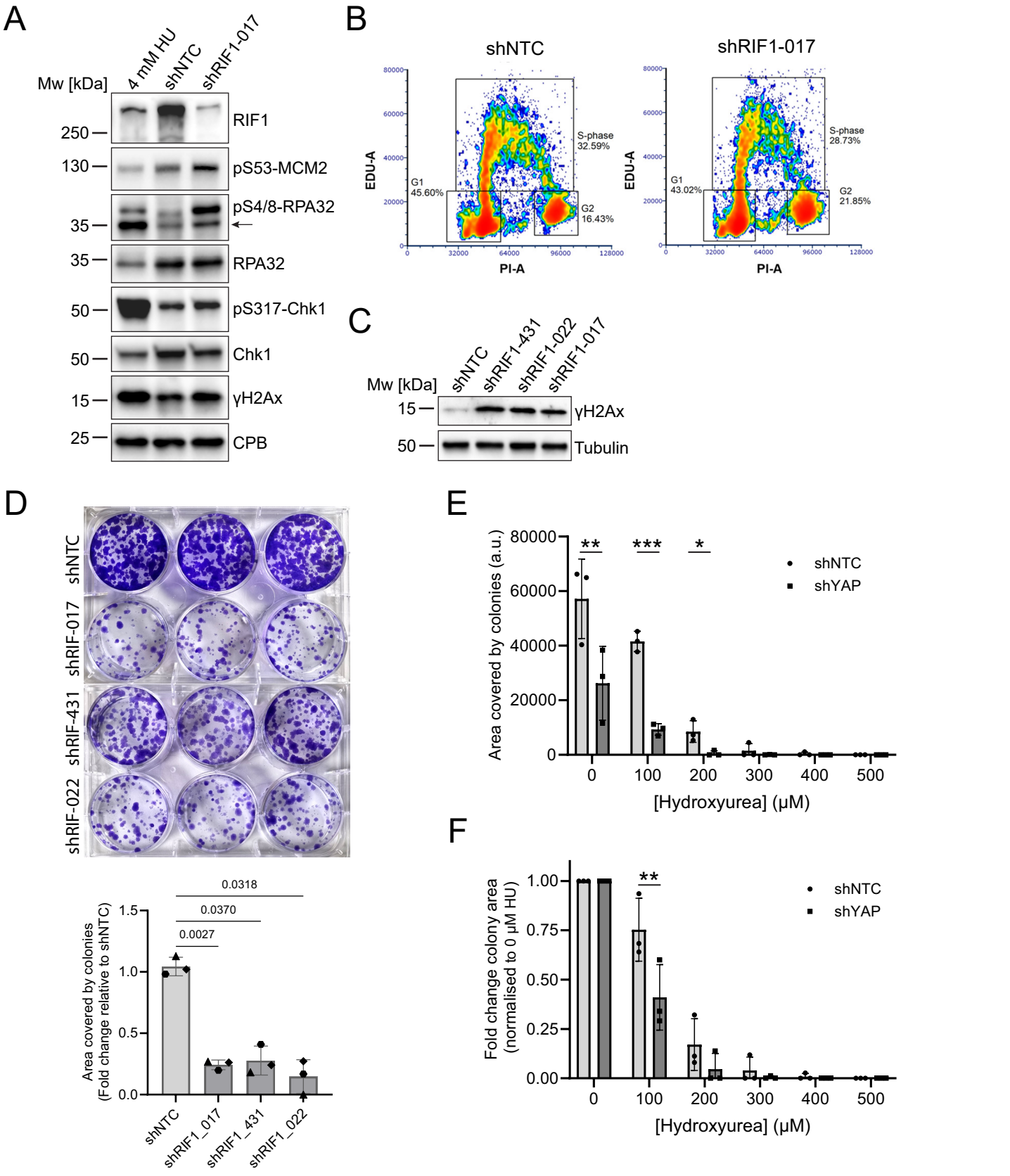

Figure 7_Bojko et al.

A

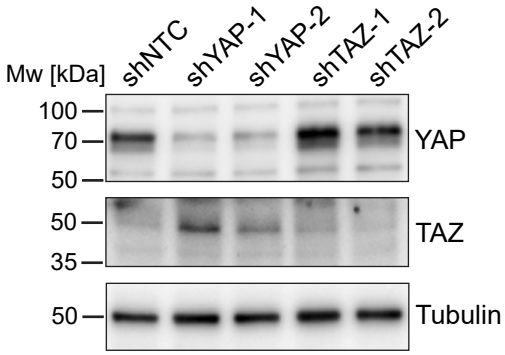

B

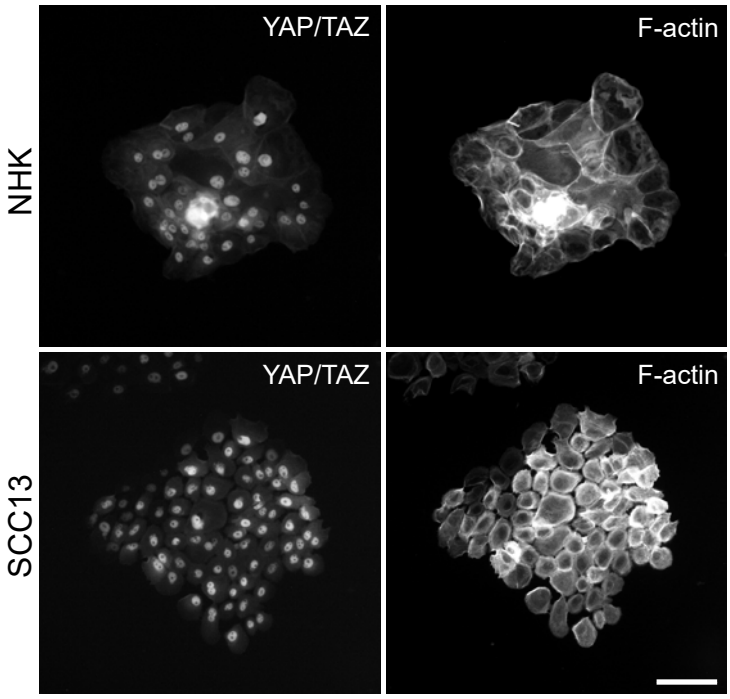

C

Accession	Description	Coverage	#Spec	Sample
P46937	Transcriptional coactivator YAP1...	60%	40	1Km5_Exp1_R1
P46937	Transcriptional coactivator YAP1...	60%	31	1Km5_Exp1_R2
P46937	Transcriptional coactivator YAP1...	63%	52	2SCC13_Exp1_R1
P46937	Transcriptional coactivator YAP1...	63%	48	2SCC13_Exp1_R2
P46937	Transcriptional coactivator YAP1...	60%	38	3Km5_Exp2_R1
P46937	Transcriptional coactivator YAP1...	65%	49	3Km5_Exp2_R2
P46937	Transcriptional coactivator YAP1...	65%	51	4SCC13_Exp2_R1
P46937	Transcriptional coactivator YAP1...	63%	48	4SCC13_Exp2_R2

Figure S1_Bojko et al.

A

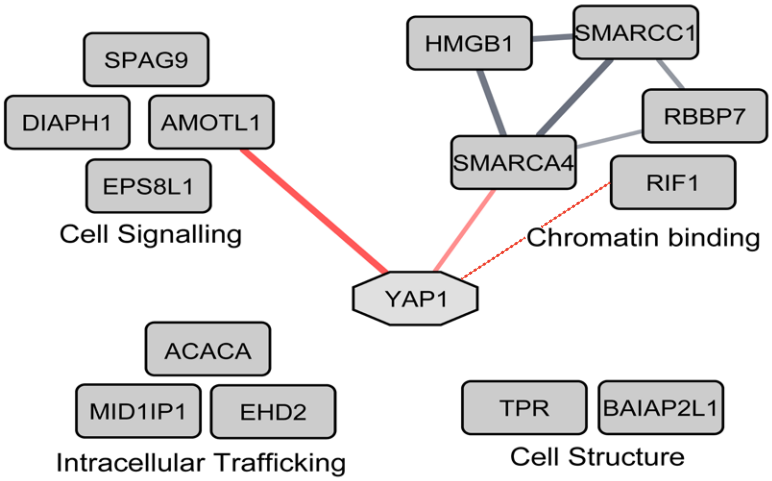

B

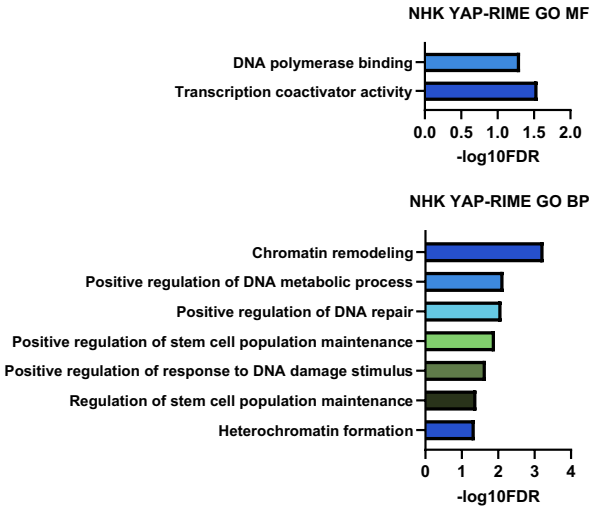

C

	YAP-IP_EXP1_mean spectral counts	YAP-IP_EXP2_mean spectral counts
SCC13	72.5	47.5
NHK	15.5	17

D

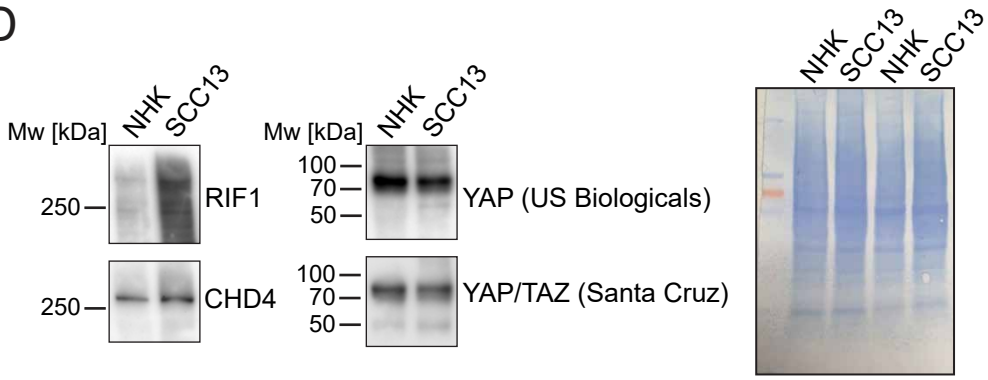

Figure S2_Bojko et al.

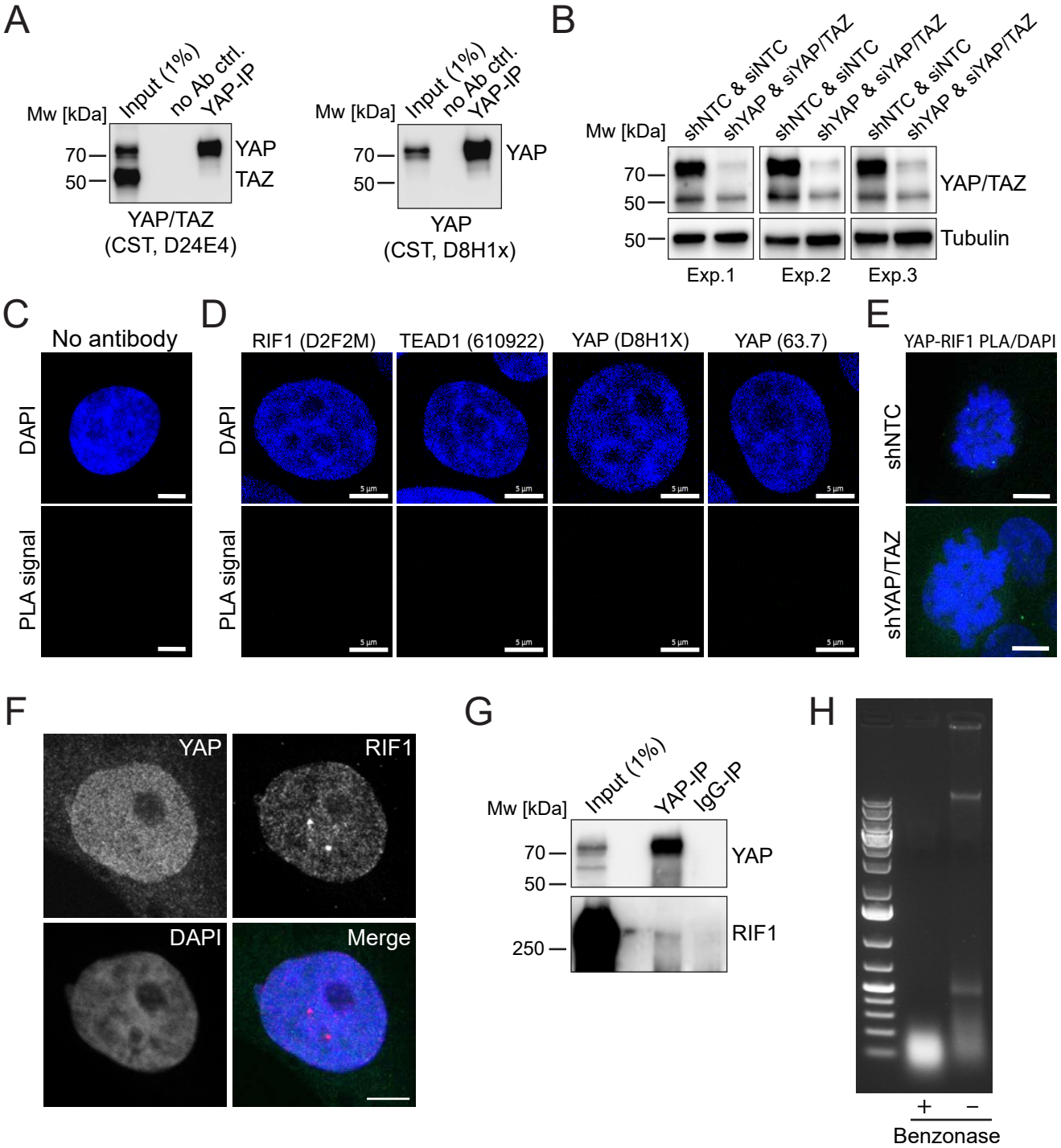

Figure S3_Bojko et al.

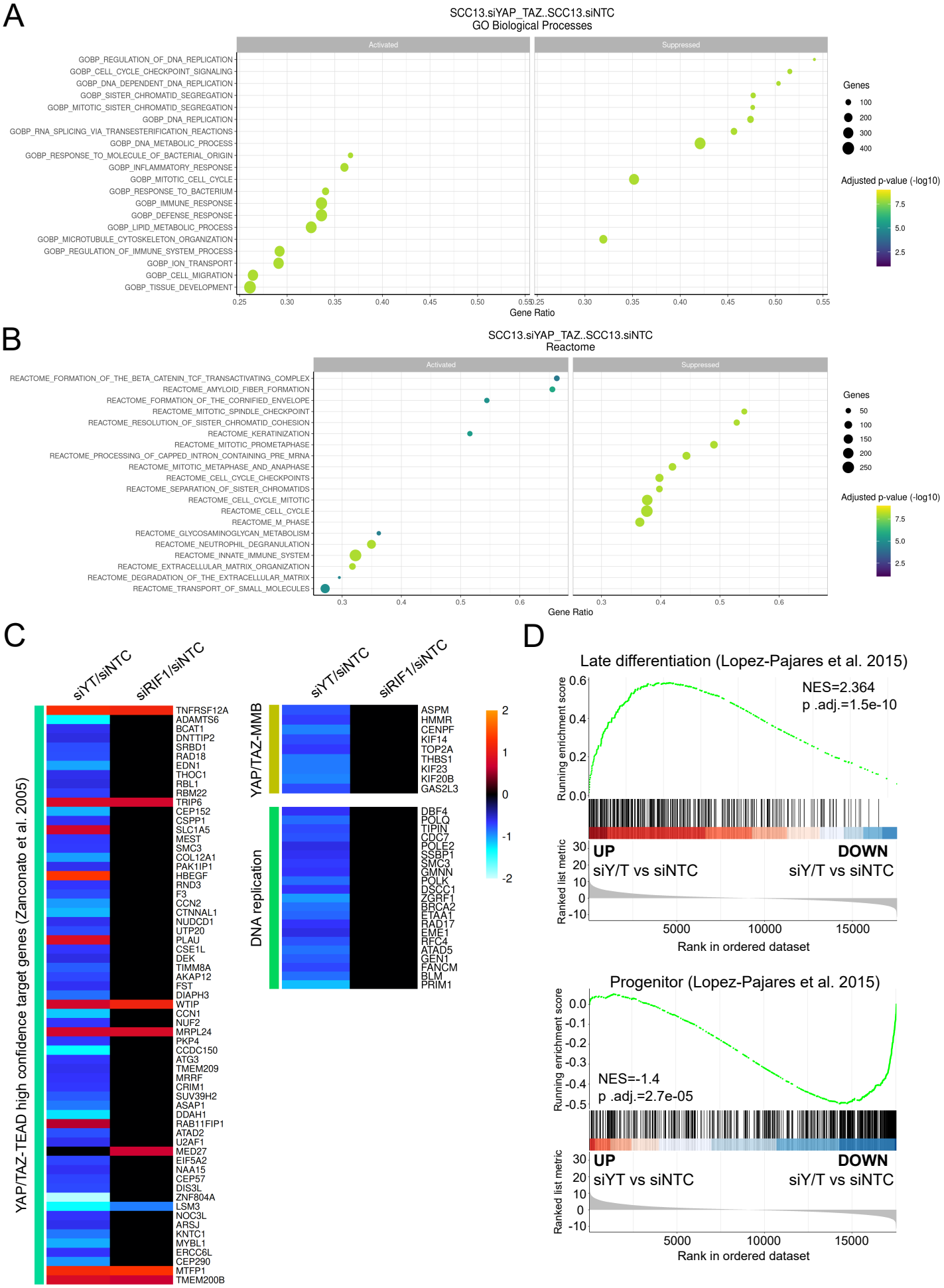

Figure S4_Bojko et al.

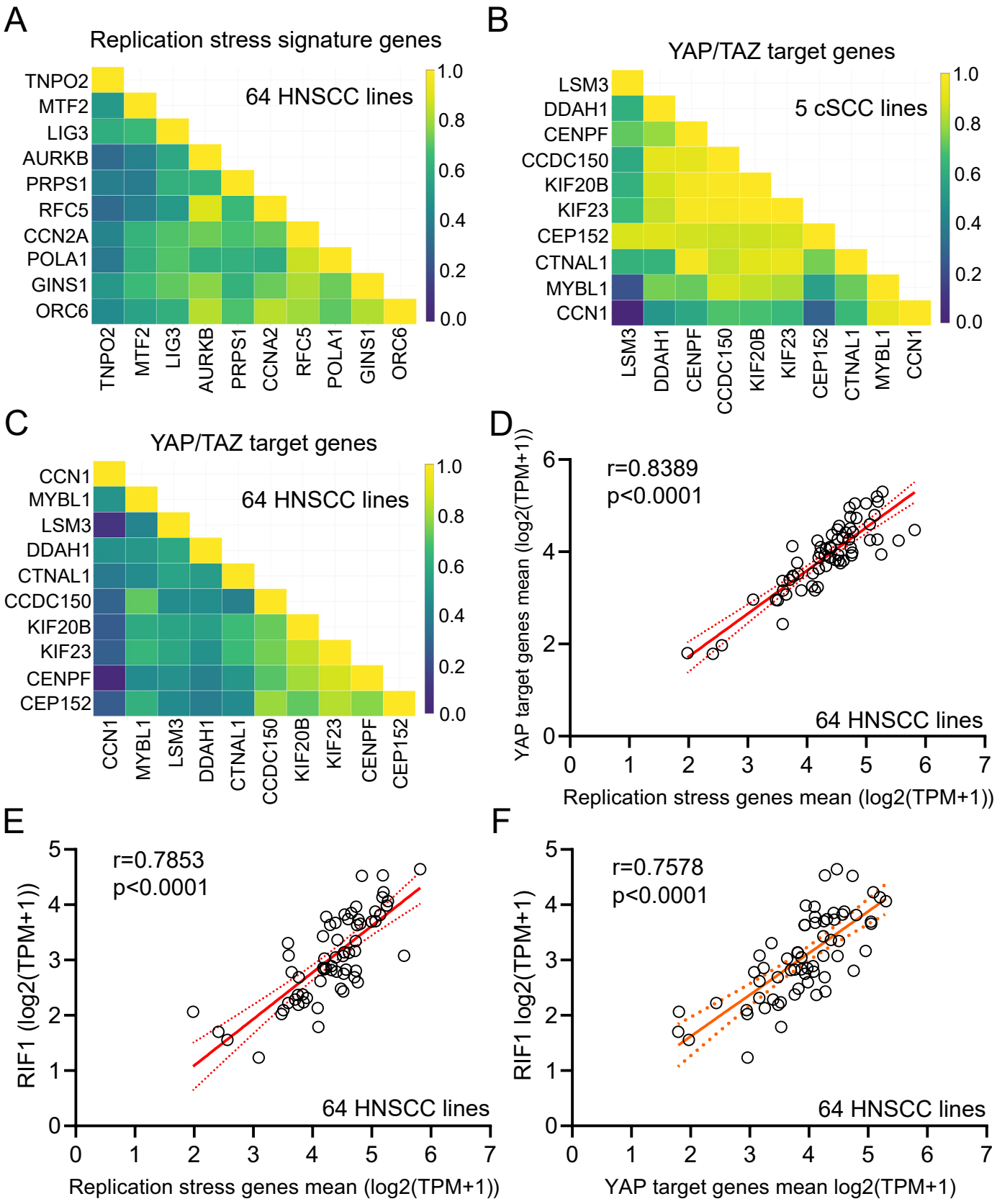

Figure S5_Bojko et al.

A

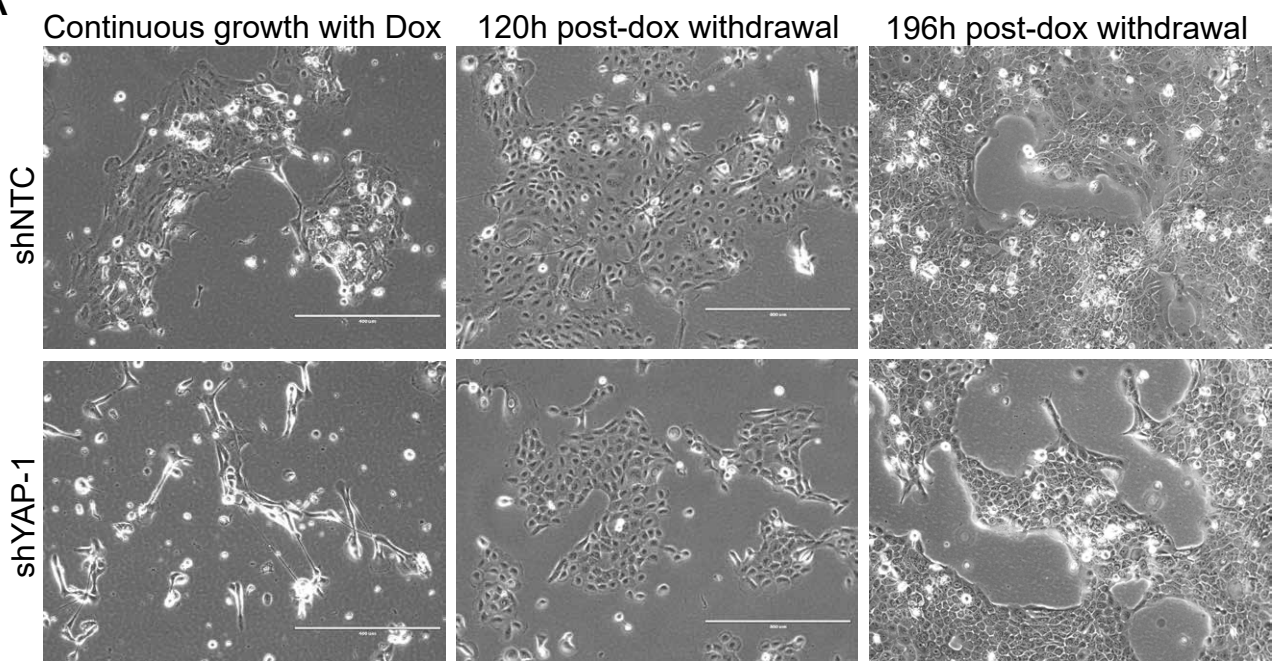

Figure S6_Bojko et al.

A

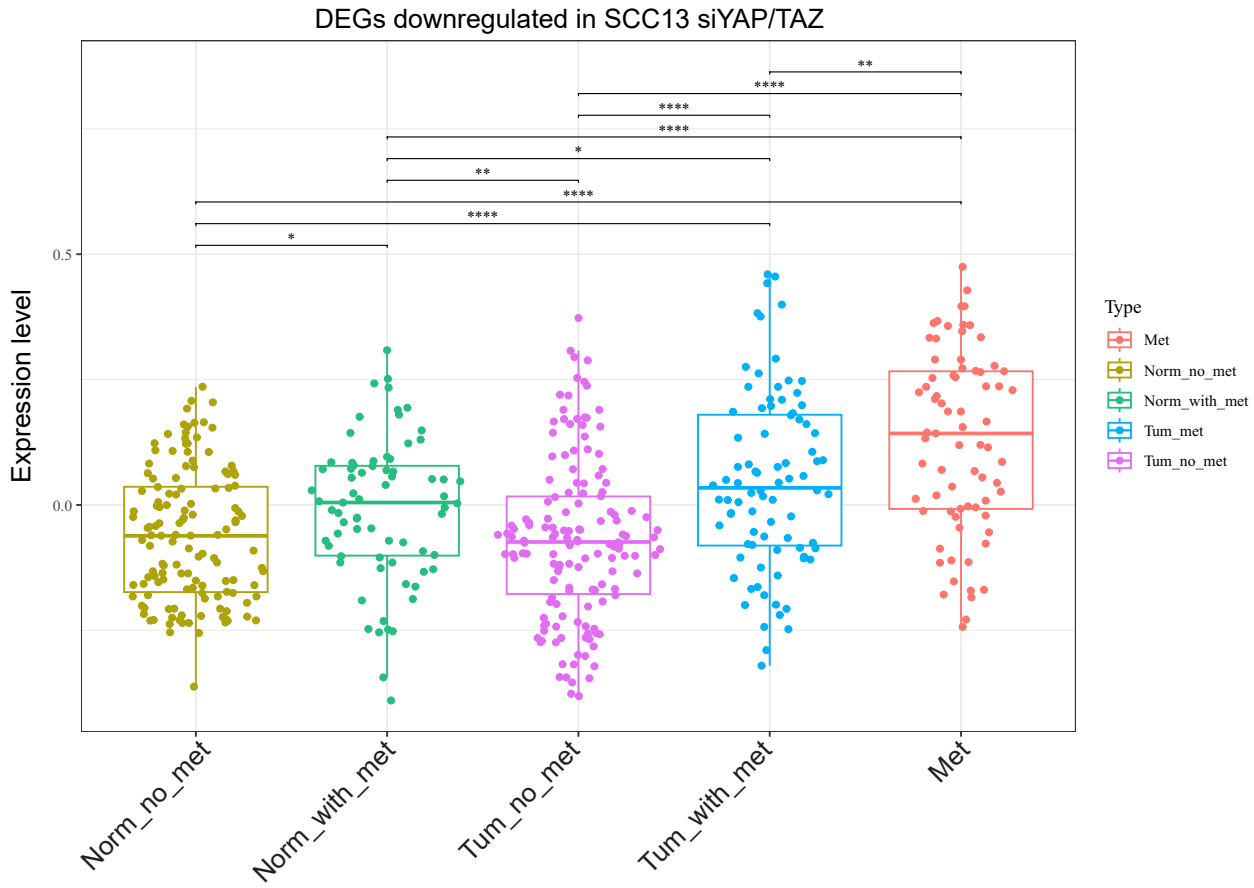

B

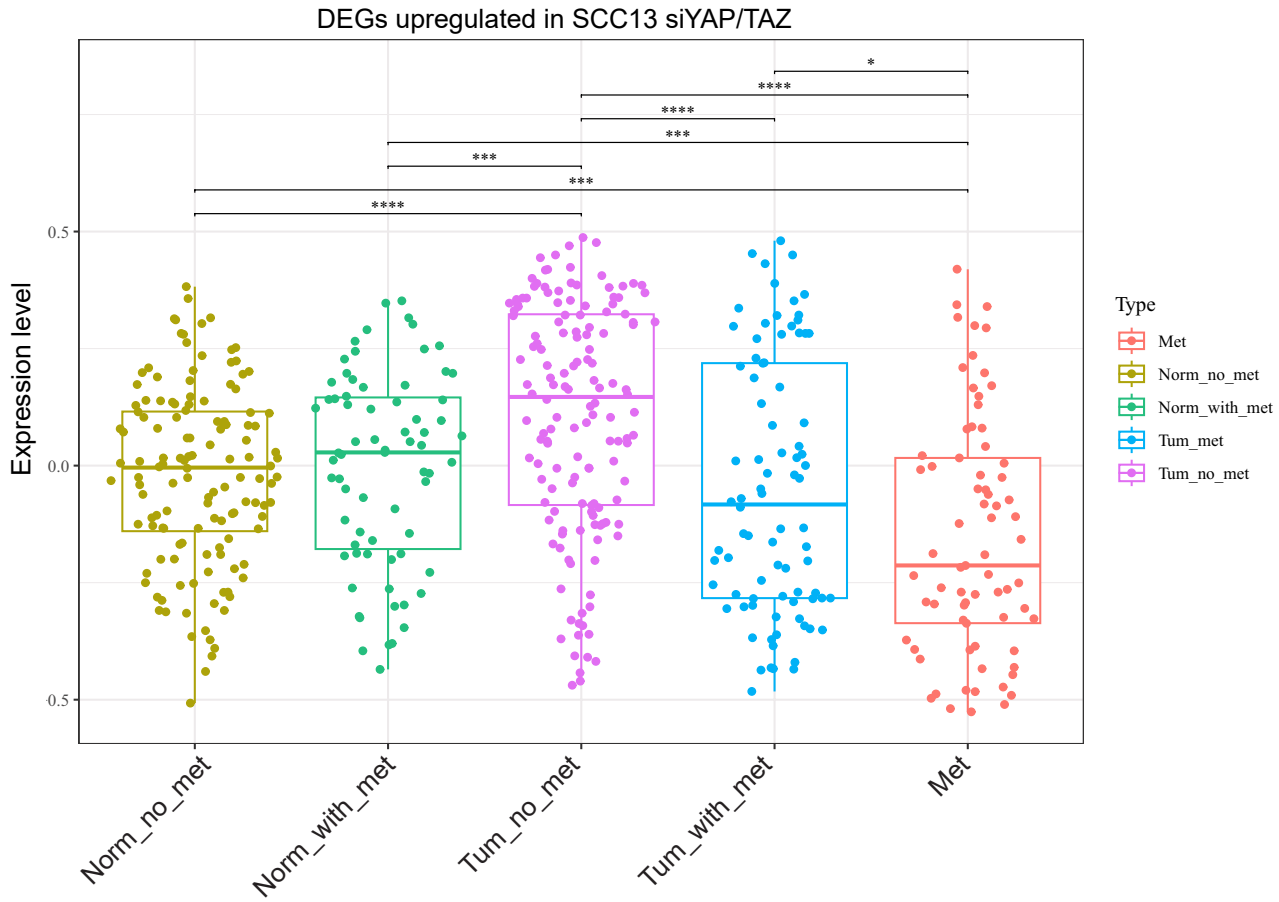

Figure S7_Bojko et al.

A

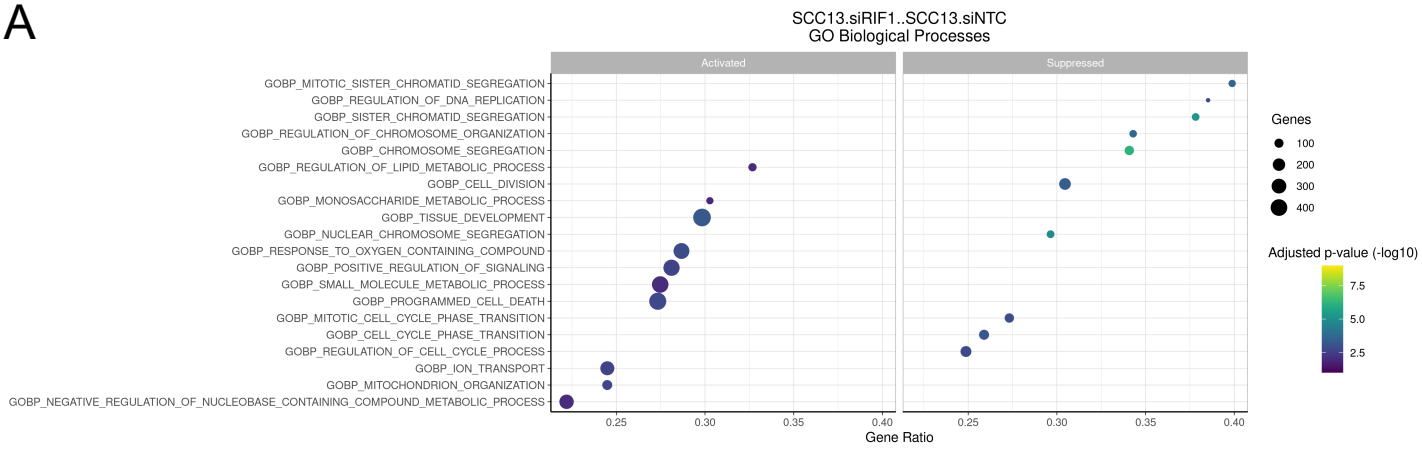

B

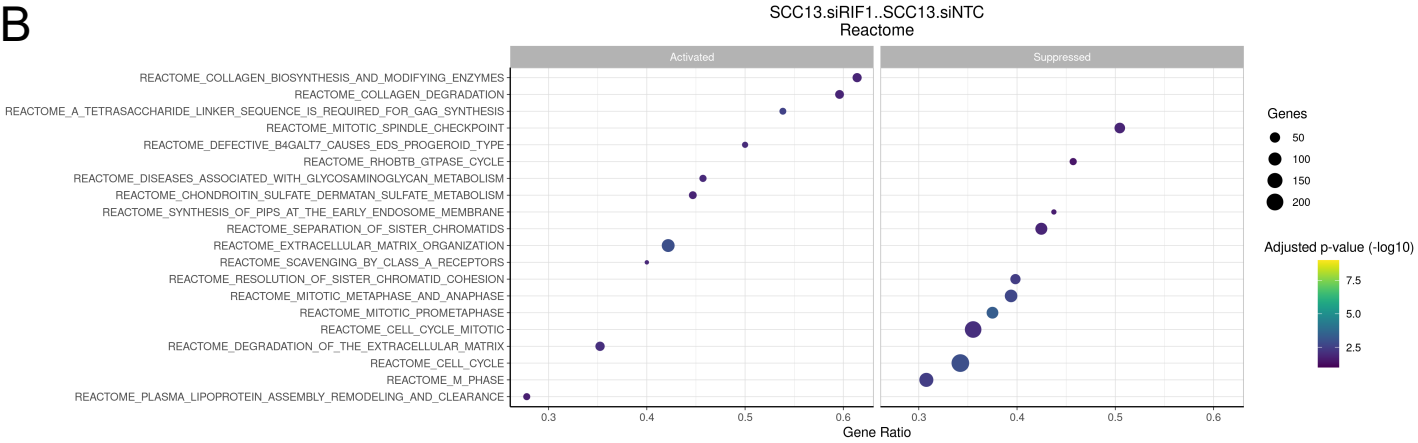

C

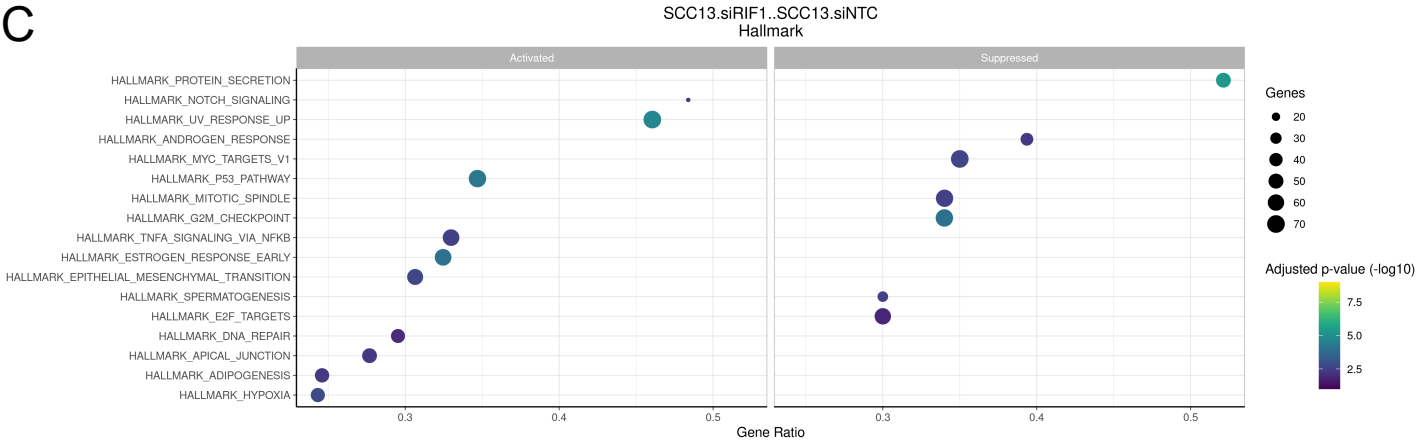

Figure S8_Bojko et al.

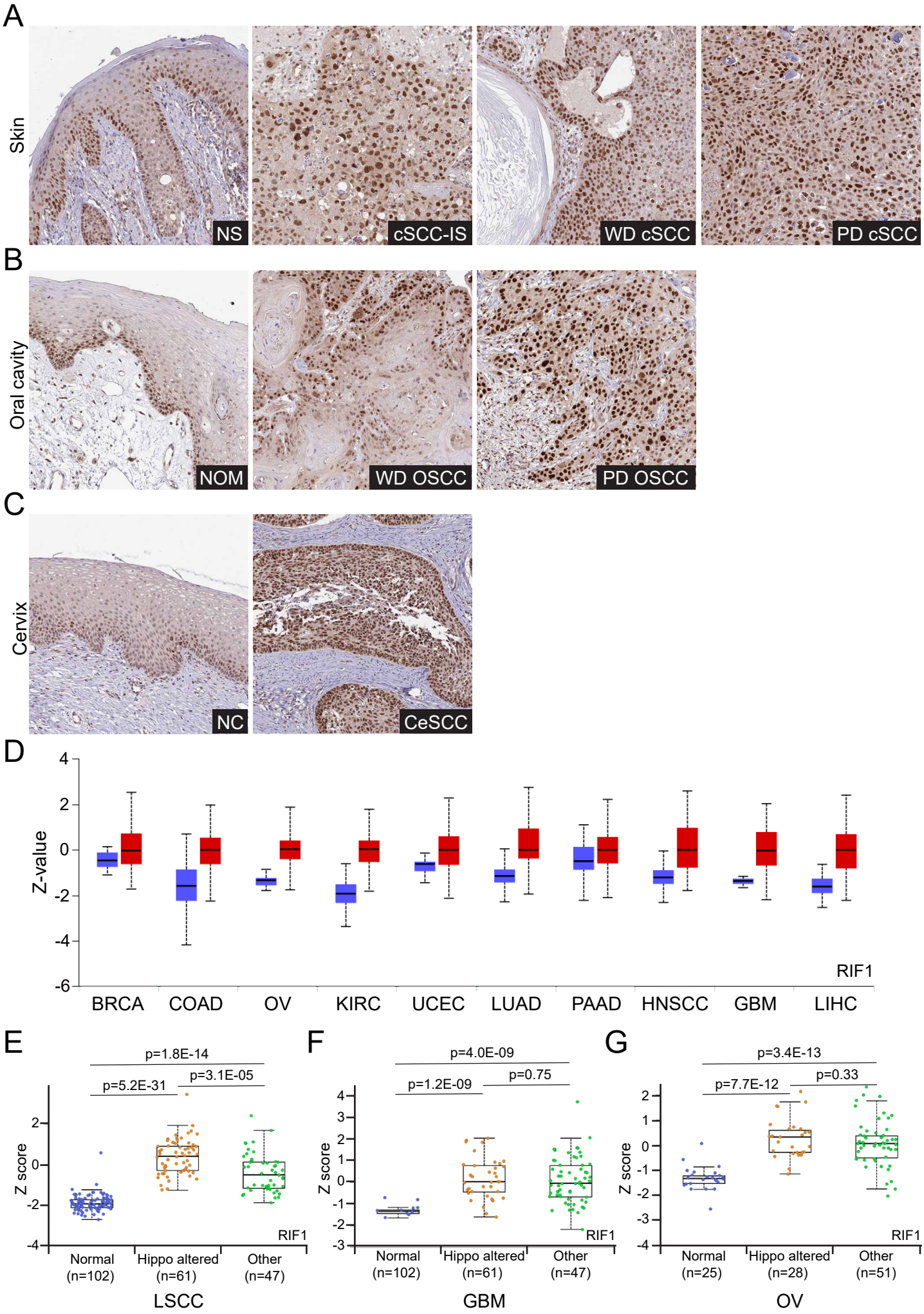

Figure S9_Bojko et al.